Single spin asymmetries in semi-inclusive electroproduction of pions and kaons on a transversely polarized hydrogen target at HERMES

Den naturwissenschaftlichen Fakultäten

der Friedrich-Alexander-Universität Erlangen-Nürnberg

zur

Erlangung des Doktorgrades

vorgelegt von

Ralf-Christian Seidl aus Nürnberg

Als Dissertation genehmigt von den Naturwissenschaftlichen Fakultäten der Universität Erlangen-Nürnberg

Tag der mündlichen Prüfung: 2. August 2004

Vorsitzender der Promotionskommision:	Prof. Dr. L. Dahlenburg
Erstberichterstatter:	Prof. Dr. K. Rith
Zweitberichterstatter:	Prof. Dr. D. Ryckbosch
Drittberichterstatter:	Prof. DR. M. Burkardt

Contents

0

Zusammenfassung

Diese Doktorarbeit behandelt die Messung azimutaler Einzel-Spin-Asymmetrien von Pionen und Kaonen in semi-inklusiver tief-unelastischer Lepton-Proton Streuung am HERMES Experiment am DESY. Es werden die Resultate der Datennahme mit einem transversal polarisierten Proton Target vorgestellt.

Neben der unpolarisierten und der longitudinal polarisierten Quarkverteilung im Nukleon existiert in führender Ordnung noch eine dritte Quarkverteilung, die sogenannte *Transversity*. Sie misst die Differenz der Wahrscheinlichkeit, Quarks anzutreffen, deren Spin parallel zum transversalen Spin des Nukleon bzw. dazu antiparallel ausgerichtet ist. Diese Grösse ist bisher noch nicht bestimmt worden, da sie aufgrund der Helizitätsumkehr in der zugehörigen elastischen Compton Steuamplitude in inklusiver tief-unelastischer Lepton-Nukleon Streuung aufgrund der Helizitätserhaltung von nahezu masselosen Quarks nicht zugänglich ist. Entsprechend bedarf die Messung dieser chiral ungeraden transversalen Quarkverteilung einer zweiten chiral ungeraden Grösse, damit die Chiralität des Gesamtprozesses wieder gerade ist. In Drell-Yan Prozessen (Proton + (Anti)Proton → Lepton + Antilepton) kann dies eine zweite transversale Antiquarkverteilung sein, während in tief-unelastischer Lepton-Nukleon Streuung eine Fragmentationsfunktion den chiral ungeraden Partner stellen kann. Diese Möglichkeit der Messung setzt voraus, dass man zusätzlich zum gestreuten Lepton noch mindestens ein Hadron des bei der Streuung entstandenen hadronischen Endzustands detektiert. Man spricht dann von der semi-inklusiven tief-unelastischen Lepton-Nukleon Streuung. Eine Besonderheit der führenden chiral ungeraden Fragmentationsfunktion, der sogenannten Collins Funktion, ist, dass sie vom intrinsischen Transversalimpuls des Quarks, welcher bei der Fragmentation entsteht, abhängt. Diese Abhängigkeit erzeugt eine azimu-

tale Verteilung der erzeugten Hadronen um die Richtung des virtuellen Photons, welches mit dem Nukleon wechselwirkt. Diese Verteilungen lassen sich dann als azimutale Asymmetrien zweier entgegengesetzter Target Spinzustände in einem Detektor wie HERMES nachweisen. Es tritt noch eine weitere Grösse auf, die azimutale Asymmetrien erzeugt, welche in diesem Fall vom intrinsischen Tansversalimpulse des Quarks im Nukleon abhängt. Die sogenannte Sivers Funktion misst die Differenz zwischen den Wahrscheinlichkeiten, ein unpolarisiertes Quark in zwei entgegengesetzten transversal polarisierten Targetspinzuständen anzutreffen. Da diese Größe die Existenz von Bahndrehimpuls der Quarks im Nukleon voraussetzt, erschließt sie eine Möglichkeit, diesen Beitrag zum Gesamtspin des Nukleons zu messen. Wenn auch bisher noch kein direkter Zusammenhang zwischen Bahndrehimpuls und der Größe der Sivers Funktion bewiesen werden konnte, wurde er indirekt in diversen Modellen bereits gesehen.

In bisherigen Messungen an einem longitudinal polarisierten Target erzeugen beide Funktionen, die Collins Funktion und die Sivers Funktion, dieselbe azimutale Abhängigkeit, weswegen man nur eine Kombination beider Größen messen kann. In einem transversal polarisierten Target sind beide Größen entkoppelt und können simultan gemessen werden. Um diese Möglichkeit genauer zu untersuchen, wurden Monte-Carlo Studien durchgeführt. Hierbei stellt sich heraus, dass die Extraktion beider Amplituden am zuverlässigsten in einer zweidimensionalen Fit-Prozedur gewährleistet ist. Auch Einflüsse des transversalen Targetmagneten, und die damit verbundene Verschlechterung der Auflösung in den kinematischen Variablen wurden untersucht. Mittels einer Korrektur der geladenen Teilchenspuren erreicht man allerdings wieder die ursprünglichen Auflösungen, so dass der Effekt des Targetmagneten die Asymmetrierekonstruktion nicht weiter beeinträchtigt.

Weiterhin werden die Analyse der gemessenen Daten, sowie systematische Studien an den Daten erörtert, woran sich die Präsentation der extrahierten Ergebnisse anschliesst. Da die Ergebnisse im Collins Kanal nicht mit den theoretischen Erwartungen übereinstimmen, werden im Rahmen eines einfachen Modells Wahrscheinlichkeitsverteilungen von Verhältnissen der unbekannten Grössen auf der Basis der gemessenen Werte berechnet. Diese geben einen Hinweis darauf, dass das Verhältnis der unfavorisierten zur favorisierten Collinsverteilung nahe eins und negativ ist. Mit diesem Resultat, das bisher in keiner theoretischen Vorhersage enthalten ist, werden die Vorhersagen mit den gemessenen Werten verglichen. Im Falle der Sivers Funktion lassen sich die vereinfachten Modellannahmen nutzen, die Sivers Funktionen der positiv und negativ geladenen leichten Quarks zu ermitteln.

Als Ausblick werden zukünftige Messungen bei HERMES und anderen Experimenten vorgestellt.

1

Introduction

Wisdom begins in wonders.
Sokrates

Before the appearance of the so called spin crisis [A$^+$88] at the end of the 80s it was generally assumed that the spins of the 3 valence quarks, all spin 1/2 fermions, would directly add up to the nucleon spin of 1/2. It came as a surprise when the measurements by the EMC experiment at CERN [A$^+$88] gave a hint that only a small fraction of the nucleon spin can be attributed to the spins of the quarks. This has since been confirmed by many more experiments. So, what else contributes? It is known since quite some time that the quarks are not the only particles occupying the nucleon. As they are not only electrically-charged but also color-charged objects they can interact by the electroweak force and also the strong color interaction. The mediators of the corresponding local gauge theory, Quantum Chromo Dynamics (QCD), are the gluons which have been first observed at DESY in the 70s. Since then one knows that the 3 valence quarks of the nucleon continually interact with many gluons which sometimes break apart into quark-antiquark pairs or into other gluons. So instead of the nucleon being only built by three valence quarks it is filled by a complete *sea* of quarks and gluons occupying the average volume of a nucleon. Consequently these sea quarks and the gluons may also contribute a share of the total spin to this compound object. The latest DIS measurements not only allow to deduce the sea-quark and gluon contribution to the nucleon spin from global fits to the data but to determine them directly. Additionally, orbital angular momentum of the quarks and the gluons can contribute to the total spin.

Adding up all contributions one obtains:

$$\frac{s_z^N}{\hbar} = \frac{1}{2} = 1/2\Delta\Sigma_q + \Delta g + L_q^z + L_g^z \quad , \tag{1.1}$$

where $\Delta\Sigma$ is the contribution by the quark spins, Δg the one by the gluon spins, and L_q^z and L_g^z represent the contributions of orbital angular momentum of the quarks and gluons.

Up to now the latter could not be measured although a connection to generalized parton distributions could be established [Ji97a]. Recently also another possibility is being discussed which might help to access the orbital angular momentum. A new class of quark distribution functions depending also on the intrinsic transverse momentum of the quarks was introduced, with its most prominent member being the so-called Sivers function. Such distributions can only exist if the quark angular momentum is non-zero. Here no direct relation to the angular momentum is available, but models at least see such a connection.
Another unknown quark distribution function is the so-called *transversity* distribution which due to its chiral-odd nature cannot be measured in inclusive deep-inelastic lepton-nucleon scattering (DIS). Newer experiments such as HERMES allow the identification of some hadrons in the final state, known as semi-inclusive DIS, which are able to access the transversity distribution. Since transversity is chiral-odd the second non-perturbative object in this process, the fragmentation function, has to exhibit the same properties. This is the so-called Collins function which again depends on intrinsic transverse momentum.
This transverse momentum dependence is the key to measure these two quark distribution functions: Transversity and the Sivers function. As will be explained in the following chapters the transverse momentum dependence creates observable left-right asymmetries which can be measured as single target-spin asymmetries in the semi-inclusive DIS experiments. The first results on a transversely polarized target at HERMES will be presented in this thesis.
This thesis is organized as follows: In the second chapter the theoretical basics of spin dependent semi-inclusive DIS are described. The third chapter especially treats the theoretical properties of transversity and the intrinsic transverse momentum dependent distribution and fragmentation functions and their connection to measurable single spin asymmetries. Chapter 4 addresses the HERMES experiment at the accelerator complex HERA at DESY. Also aspects of the data-taking are addressed there. Chapter 5 continues with the details of the analysis as well as the relevant systematic studies on both a MC generated and the real data sample. Chapter 6 contains the extracted virtual-photon asymmetries and gives interpretations based on simple model calculations. A detailed comparison with existing model predictions is shown and discussed there as well. Chapter 7 gives an outlook on the quark distribution extraction and the possibilities to measure the functions involved in greater detail at HERMES and other experiments.

1.0.1 Notations and conventions

Throughout this thesis most notations are similar to the so-called Mulders notation [MT96], that is quark momenta are described by **p** when referring to intrinsic momentum in the quark distribution part of the cross section and momenta described by **k** are applied for the fragmentation part. Except for the leading-twist transverse-momentum-independent quark distribution functions the Mulders notation is applied for the distribution and fragmentation functions. These three distribution functions specified differently are defined as $q(x)$, $\Delta q(x)$ and $\delta q(x)$ as the Mulders notation for them is also applied for the charge square weighted sums over the quarks and correspond to the structure functions $f_1(x)$ and $g_1(x)$. In the following $\hbar$ and c are set to 1, the definitions of the metric tensor $g_{\mu\nu}$ and the light-cone coordinates are defined in appendix A.

2

Structure of the nucleon - DIS

2.1 General formalism of QCD

Quantum Chromo Dynamics (QCD) is the gauge theory of the strong interaction between objects containing the charge color. The participants in this interaction are quarks which belong to the basic representation of the gauge group $SU(3)_{color}$ containing the 3 charges red, blue and green for example. The mediators of QCD - its gauge bosons, namely the gluons who conserve the local gauge invariance - can be classified by the $N_c^2 - 1$ generators T^a of such $SU(N_c)$ transformations,

$$U(A^a_\mu(x))_\mu = e^{iA^a_\mu(x)T^a} \quad , \tag{2.1}$$

where $A^a_\mu(x)$ are the gauge fields creating them. These eight 3×3 matrices T^a are generally chosen to be the Gell-Mann matrices [GM64] λ^a which can be found in appendix A. Accordingly there are 8 different gluons which due to this matrix or adjoint representation of $SU(3)_c$ always contain a combination of color and anti-color ($3 \times \bar{3}$). Note that no singlet combination exists next to the octet of gluons in contrast to $SU(3)_{flavor}$, the gauge symmetry between the 3 light quarks, where the η' as a symmetric combination of u, d and s quark and antiquarks exists. Its existence would be permitted by the mechanism of confinement which allows only to observe color singlet or color invariant states, but such a singlet gluon would create a strong long-range force between other color singlet states like hadrons [Gri] which has not been observed.

In order to create not only a globally but locally gauge invariant theory one has to introduce covariant derivatives

$$D_\mu(x) = \partial_\mu - igA^a_\mu(x)T^a \quad , \tag{2.2}$$

which take into account the infinitesimal change in the gauge field $A^a_\mu(x)$ when comparing for example 2 quark fields at infinitesimal separation dx_μ. In an analogous way to QED the field strength tensor $F_{\mu\nu}$ can be calculated by the commutator of two covariant derivatives

$$-igT^a F_{\mu\nu} = [D_\mu, D_\nu] \quad . \tag{2.3}$$

The only difference to QED arises in the fact that the gauge fields $A^a_\mu(x)$ and $A^b_\mu(x)$ do not commute and hence this gauge theory is non-abelian. The complete Lagrangian for QCD can be written as

$$\mathcal{L} = \bar{\psi}(i\not{D})\psi - \frac{1}{4}F^a_{\mu\nu}F^{\mu\nu a} - m\bar{\psi}\psi \quad , \tag{2.4}$$

where ψ are Dirac fermion fields representing the quarks of mass m. The non-abelian nature of such a gauge theory allows not only quark-quark-gluon vertices but also 3-gluon or 4-gluon vertices which enables the gluons to couple to themselves as displayed in Fig 2.1. When calculating the quark-gluon coupling $\alpha_S = \frac{g^2}{4\pi}$ one has to include all possible loop diagrams to the gluon propagator which can be summed up in leading order of the coupling into an effective coupling which depends on the momentum transfer $|q^2|$ of the gluon [PS]:

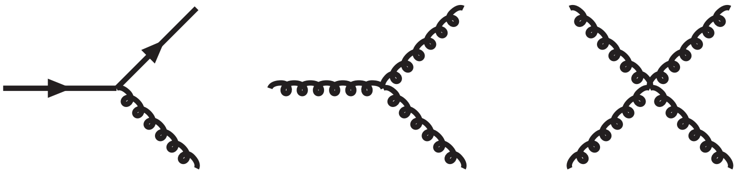

Figure 2.1: Quark-gluon and gluon-gluon vertices

$$\alpha_s(|q^2|) = \frac{12\pi}{(11n - 2f)\ln(|q^2|/\Lambda^2_{QCD})} \quad (|q^2| \gg \Lambda^2_{QCD}), \tag{2.5}$$

where $\Lambda_{QCD} \approx 250\ MeV$ is a parameter containing a lower momentum cut-off and the coupling at that scale, n is the number of colors (ie. 3 in QCD) and f is the number of quark flavors which is found to be 6 [A$^+$95].

It can be seen that the coupling α_s becomes weak at momentum transfers well above Λ_{QCD} and can thus be used as a perturbative expansion parameter. It follows that at high energies quarks can be treated as free particles. This is also known as asymptotic freedom [tHV72]. On the other hand one immediately sees from equation 2.5 that at low energies the coupling becomes large and a perturbative description will fail. This is the confining regime where the color interaction does not allow non-singlet states to exist. In this regime one has to use either effective theories like some bag models or quark soliton models, or to take phenomenological models such as the quark-diquark model and perturbative QCD analysis to calculate measurable predictions or use the lattice-QCD with discretized space-time.

2.2 DIS cross section

The nucleon, as all baryons and mesons, is a system of confined quarks and gluons. Therefore only non-perturbative methods can describe its properties. Since these methods are nowadays mostly effective models they cannot give a full description of the QCD structure of the nucleon. The chiral quark soliton model, for example, lacks any gluonic degrees of freedom [S$^+$01] and thus can only make predictions for the quark content of the nucleon which does not involve explicit gluonic variables [Pob02].
As a consequence one has to rely on experimental results to get as much information as possible. Next to the creation of quark-antiquark pairs and subsequently hadrons in e^+e^- annihilation and $p\bar{p}$ annihilation processes lepton nucleon scattering gives a very reliable and clean access to the nucleon structure.

2.2.1 Elastic lepton nucleon scattering

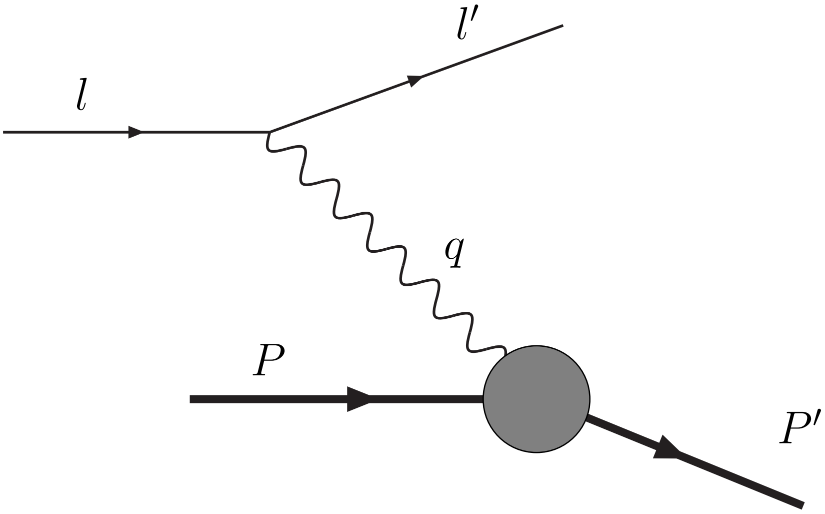

Figure 2.2: Feynman diagram of elastic lepton nucleon scattering

In the simplest case such a process can be the elastic scattering of an (anti)electron off a proton which stays intact: $e + p \rightarrow e + p$. The corresponding Feynman diagram is depicted in Fig. 2.2 where the *blob* is a reminder of the substructure of the nucleon, l and P are the four-momenta of the incoming electron and the proton respectively and l' and P' are those of the scattered particles. The momentum transfer via the virtual photon from the lepton vertex to the proton vertex is just the difference of the incoming and outgoing four-momenta $q = l - l' = P' - P$. The spin averaged amplitude of such a process can easily be calculated by applying the according Feynman rules for QED and trace technology [PS].

$$\langle|\mathcal{M}|^2\rangle = \frac{\alpha^2}{q^4} L_{\mu\nu} K^{\mu\nu} \quad , \tag{2.6}$$

where

$$L^{\mu\nu} = 2\left(l^\mu l'^\nu + l^\nu l'^\mu + g^{\mu\nu}(m^2 - l^\sigma l'_\sigma\right) \tag{2.7}$$

is the well known leptonic tensor, $\alpha = \frac{e^2}{4\pi}$ is the electromagnetic coupling and m is the mass of the lepton which can be neglected at typical lepton energies. Its hadronic counterpart $K^{\mu\nu}$ cannot be directly calculated, but since it has to be a Lorentz tensor and since the proton charge has to be conserved [Gri] it is possible to parameterize it by

$$K^{\mu\nu} = K_1\left(-g^{\mu\nu} + \frac{q^\mu q^\nu}{q^2}\right) + \frac{K_2}{M^2}\left(P^\mu + \frac{1}{2}q^\mu\right)\left(P^\nu + \frac{1}{2}q^\nu\right) \quad , \tag{2.8}$$

where K_1 and K_2 are the proton form factors, M is its mass and P is the incoming proton momentum. These form factors only depend on q^2 and contain very little information about the substructure in the nucleon itself as the proton stays intact and its constituents can only contribute coherently. They can be redefined as the electric (G_E) and magnetic (G_M) form factors of the nucleon [BD]. The form factors only represent one limiting edge of the broader framework of the generalized parton distributions [GPV01]. After knowing the structure of the scattering amplitude the corresponding differential cross section, known as the Rosenbluth formula [Ros50], can easily be calculated to be

$$\frac{d\sigma}{d\Omega} = \frac{4\alpha^2 E^2 \cos^2(\theta/2)}{q^4[1 + (2E/M)\sin^2(\theta/2)]}\left(\frac{G_E^2 + \tau G_M^2}{1+\tau} + 2\tau G_M^2 \tan^2(\theta/2)\right) \quad , \tag{2.9}$$

where θ is the scattering angle, $d\Omega$ is the solid angle and $\tau = -q^2/4M^2$.

2.2.2 Deep-inelastic scattering (DIS)

In order to access information on the quark content of the nucleon one has to use lepton energies sufficient to break up the proton.

As can be seen in Fig. 2.3 the proton breaks apart and its remnants fragment into many different hadrons. The cross section of such a process can still be calculated similarly to equation 2.9 as the lepton vertex did not change and thus the Lorentz structure of the hadronic tensor can still be classified as before. The differential cross section

$$\frac{d^2\sigma}{d\Omega dE'} = \frac{\alpha^2}{2Mq^4}\frac{E'}{E} L_{\mu\nu} W^{\mu\nu} \tag{2.10}$$

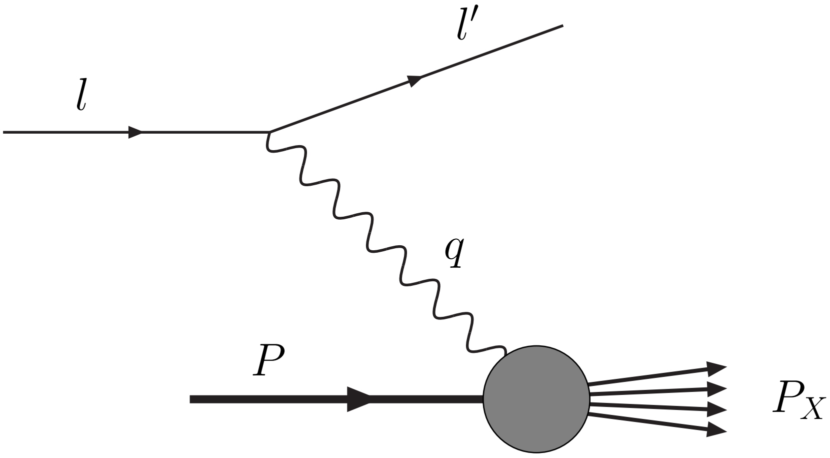

Figure 2.3: Feynman diagram of deep inelastic lepton nucleon scattering

is now double differential as the energy of the scattered lepton is not anymore defined by the scattering angle θ or the momentum transfer q alone.
In later chapters I will also address spin dependent quantities. Here one cannot average out the spin of the incoming lepton and has to add a completely antisymmetric part to equation 2.7

$$L_{\mu\nu}(l,s;l') = 2\left[L^{(S)}_{\mu\nu}(l;l') - iL^{(A)}_{\mu\nu}(l,s;l')\right] \tag{2.11}$$

which consists of [Lea01]

$$L^{(A)}_{\mu\nu} = m\epsilon_{\mu\nu\alpha\beta}s^\alpha q^\beta \quad , \tag{2.12}$$

where s is the spin 4−vector of the lepton. This allows a hadronic tensor containing an antisymmetric component also to be included:

$$W_{\mu\nu}(q;P,S) = W^{(S)}_{\mu\nu}(q;P) + iW^{(A)}_{\mu\nu}(q;P,S) \quad . \tag{2.13}$$

This tensor now consists of

$$\begin{aligned} W^{(S)}_{\mu\nu}(q;P) &= 2M\Bigg[W_1(Pq,q^2)\left(-g^{\mu\nu} + \frac{q^\mu q^\nu}{q^2}\right) && (2.14)\\ &+ \frac{2W_2(Pq,q^2)}{M^2}\left(P^\mu + \frac{Pq}{q^2}q^\mu\right)\left(p^\nu + \frac{Pq}{q^2}q^\nu\right)\Bigg] && (2.15)\end{aligned}$$

and

$$\begin{aligned} W^{(A)}_{\mu\nu}(q;P,S) &= 2M\epsilon_{\mu\nu\alpha\beta}q^\alpha\Bigg[MS^\beta G_1(Pq,q^2) && (2.16)\\ &+ \left((Pq)S^\beta - (Sq)P^\beta\right)\frac{G_2(Pq,q^2)}{M}\Bigg] \quad , && (2.17)\end{aligned}$$

where S is the spin four-vector of the nucleon. Only the combinations of the two symmetric tensors and the two antisymmetric tensors do not cancel. The symmetric part of $W_{\mu\nu}$ contains only spin independent structure functions (W_1, W_2) whereas the antisymmetric part includes only spin-dependent structure functions (G_1, G_2). Conventionally these structure functions are rewritten not as functions of the variables Pq and q^2 but as functions of the positive quantity $Q^2 = -q^2$ and the Bjorken scaling variable

$$x \equiv x_{Bj} \equiv \frac{Q^2}{2Pq} \overset{lab}{=} \frac{Q^2}{2M\nu} \quad , \tag{2.18}$$

where $\nu \overset{lab}{=} E - E'$ is the energy transferred by the virtual photon in the laboratory frame. The structure functions thus become

$$MW_1(Pq, Q^2) \equiv F_1(x, Q^2) \qquad \nu W_2(Pq, Q^2) \equiv F_2(x, Q^2) \tag{2.19}$$

$$\frac{(Pq)^2}{\nu} G_1(Pq, Q^2) \equiv g_1(x, Q^2) \qquad \nu G_2(Pq, Q^2) \equiv g_2(x, Q^2) \quad . \tag{2.20}$$

At this stage x can be identified as a measure of the inelasticity of the scattering process, as in the limit of $x \to 1$ the structure functions become the aforementioned form factors and one obtains the elastic cross section of equation 2.9 (for the spin independent part).

2.3 Structure of the nucleon

Equation 2.19 allows the internal structure of the nucleon to be represented by structure functions but the connection to the quark content is not yet performed. As perturbative QCD can be applied at reasonably high energy scales, i.e. high momentum transfer $Q^2 > M^2$, where the proton breaks apart, one can describe the deep inelastic scattering process as the incoherent sum of elastic scattering on quasi-free quarks inside the nucleon which later fragment into a hadronic final state X (Fig. 2.3). The (anti-)quark is treated as a free (anti-)quark (on the mass shell) and thus the scattering of this (anti-)quark can be described by the Feynman diagram for the quark-photon-quark vertex acting as a local operator between the initial state of the nucleon and the hadronic final state.

Using the optical theorem one can relate the squared scattering amplitude to the imaginary part of the forward Compton amplitude on a quark in the background of the remnants of the nucleon as can be seen in the so-called handbag diagram in Fig. 2.4. The hadronic tensor can then be written as a sum over all final hadronic states X with their momenta $\mathbf{P}_X$ and energies E_X, integrating over the possible initial and final (anti-)quark momenta p and k:

$$\begin{aligned} W^{\mu\nu} \; = \; & \frac{1}{(2\pi)} \sum_q e_q^2 \sum_X \int \frac{d^3\mathbf{P}_X}{(2\pi)^3\, 2E_X} \int \frac{d^4k}{(2\pi)^4} \int \frac{d^4p}{(2\pi)^4}\, \delta(p^2) \\ & \times \left[\bar{u}(k)\gamma^\mu \phi(p; X, P, S)\right]^* \left[\bar{u}(k)\gamma^\nu \phi(p; X, P, S)\right] \\ & + \left[\bar{\phi}(p; X, P, S)\gamma^\mu u(k)\right]^* \left[\bar{\phi}(p; X, P, S)\gamma^\nu u(k)\right] \\ & \times (2\pi)^4\, \delta^4(P - p - P_X)\, (2\pi)^4\, \delta^4(p + q - k) \quad , \end{aligned} \tag{2.21}$$

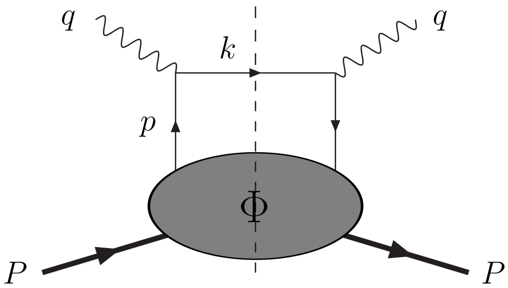

Figure 2.4: The so-called handbag diagram.

where momentum conservation is ensured by the 2 Dirac delta functions together with the corresponding integrals. $u(\bar{u})$ is the spinor of the scattered quasi-free (anti-)quark, γ^μ are the Dirac matrices, e_q is the fraction of the electron charge the quark of flavor q carries and $\phi(p; X, P, S)$ contains the emission of the soft quark from the proton being described by the matrix element

$$\phi_i(p, P, S) = \langle X|\psi_i(0)|PS\rangle \tag{2.22}$$

with ψ_i being one component of the quark spinor emerging from the complete proton. The hadronic tensor can now be split into the hard QED part describing only the photon-quark scattering and the quark-quark correlation matrix defined as

$$\begin{aligned}\Phi_{ij}(p, P, S) \;=\; & \sum_X \int \frac{d^3\mathbf{P}_X}{(2\pi)^3\, 2E_X}\,(2\pi)^4\,\delta^4(P-p-P_X) \\ & \times \langle PS|\psi_j(0)|X\rangle\langle X|\psi_i(0)|PS\rangle \quad ,\end{aligned} \tag{2.23}$$

which contains the non-perturbative QCD part. This matrix contains the information of the nucleon substructure. By the application of the completeness of hadronic final states and the translational invariance it is possible to rewrite the correlation matrix as a bilocal, bilinear operator acting on the initial nucleon state, integrated over all possible separations ξ of the second quark spinor:

$$\Phi_{ij}(p, P, S) = \int d^4\xi\, e^{ip\cdot\xi}\,\langle PS|\bar{\psi}_j(0)\psi_i(\xi)|PS\rangle \quad . \tag{2.24}$$

Any observables can now be obtained from projectors acting on this correlation matrix, taking the trace in Dirac space and integration over the internal momentum p. These projectors are constructed from combinations of Dirac matrices and thus project different Dirac structures out of the correlator and hence also out of the nucleon. The most important matrix combinations are

$$\Gamma = \left\{\gamma^\mu,\ \gamma^\mu\gamma^5,\ i\sigma^{\mu\nu}\gamma^5\right\} \quad , \tag{2.25}$$

with $\sigma^{\mu\nu} = \gamma^\mu \gamma^\nu$, which extract the (Lorentz-)vector ($\mathcal{V}_\mu$), axial vector ($\mathcal{A}_\mu$) and tensor ($\mathcal{T}_{\mu\nu}$) components [BDR02]:

$$\Phi(p, P, S) = \frac{1}{2} \left\{ \mathcal{V}_\mu \gamma^\mu + \mathcal{A}_\mu \gamma^5 \gamma^\mu + \frac{1}{2} i\, \mathcal{T}_{\mu\nu}\, \sigma^{\mu\nu} \gamma^5 \right\} \quad . \tag{2.26}$$

All of these components can only depend on combinations of the momenta p_μ, P_μ and the nucleon spin S_μ.

Choosing an infinite momentum frame (see also appendix A), and neglecting transverse momentum of the quarks in the nucleon one obtains $p^\mu \simeq xP^\mu$ and the Bjorken scaling variable x can be interpreted as the fraction of the nucleon's light-cone momentum carried by the quark. The vector component gives, after integration

$$q(x) \;=\; \frac{1}{2} \int \frac{d^4 p}{(2\pi)^4}\, Tr(\gamma^+ \Phi)\, \delta(p^+ - xP^+) \quad . \tag{2.27}$$

where $q(x)$ is the number density to find a quark of flavor q at the momentum fraction x. After summation over all possible (anti-)quarks this can be identified with the symmetric part of the hadronic tensor and gives up to order $\mathcal{O}(\frac{m^2}{Q^2})$[Bjo69]:

$$F_2(x) = 2xF_1(x) = \sum_{q,\bar{q}} e_q^2 x q(x) \quad . \tag{2.28}$$

The relation between F_1 and F_2 is known as the Callan-Gross relation [CG69] for scattering on spin-half particles. In a similar way the leading twist part, which describes the leading order in the light-cone nucleon momentum component P^+ of the axial vector component can be identified with the polarized structure function g_1:

$$g_1(x) = \frac{1}{2} \sum_{q,\bar{q}} e_q^2 \Delta q(x) \quad . \tag{2.29}$$

The quark helicity distributions $\Delta q(x)$ are only related to the light-cone, or longitudinal components of the nucleon spin S^μ and therefore instead of the complete axial vector combinations of Dirac matrices only the $\gamma^+ \gamma^5$ part is needed:

$$\Delta q(x) \;=\; \frac{1}{2} \int \frac{d^4 p}{(2\pi)^4}\, Tr(\gamma^+ \gamma_5 \Phi)\, \delta(p^+ - xP^+) \quad . \tag{2.30}$$

The transverse nucleon spin is naturally suppressed in these light-cone variables and so appears only in higher twist, which corresponds to an operator applied in an operator product expansion (OPE) that is $1/Q$ suppressed. The transverse nucleon spin can be related, together with the tensor part which is suppressed by the bare quark mass, to the transverse polarized structure function g_2. This suppression with respect to g_1 has also been verified experimentally.

The tensor component of the quark-quark correlator is related to a third quark distribution function called *transversity* distribution:

$$\delta q(x) \;=\; \frac{1}{2} \int \frac{d^4 p}{(2\pi)^4}\, Tr(\gamma^+ \gamma^1 \gamma_5 \Phi)\, \delta(p^+ - xP^+) \quad , \tag{2.31}$$

which, even though it is suppressed in inclusive DIS by the low bare quark mass, can be accessed in semi-inclusive DIS. This, as well as its properties, will be addressed in the next chapter as it is one of the key functions to the analysis which will be presented in chapters 5 and 7.

2.4 Semi-inclusive DIS

In contrast to inclusive DIS where only the scattered lepton but not the hadronic final state is observed, in semi-inclusive DIS (SIDIS) at least part of the fragments of the nucleon will be detected. By identifying at least one hadron or jet of hadrons, one is able to gain further information on the quark type involved in the hard process. Fig. 2.5 shows the leading order diagram where, in addition to the scattered lepton, also a hadron or jet of hadrons with momentum P_h and maybe even its spin S_h is detected.

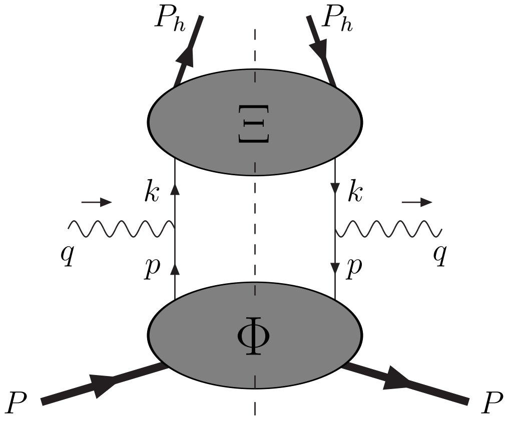

Figure 2.5: Leading order SIDIS diagram.

The second quark-quark correlation matrix Ξ, also known as fragmentation matrix is defined in a very similar way to the quark-quark correlation matrix Φ containing the quark distribution functions. Here the fragmentation matrix describes the probabilities of the struck quark fragmenting into a hadronic state $|P_h, S_h; X\rangle$:

$$\begin{aligned}\Xi_{ij}(k; P_h, S_h) &= \sum_X \int \frac{d^3\mathbf{P}_X}{(2\pi)^3\, 2E_X} \int d^4\xi\, e^{ik\cdot\xi} \\ &\quad \times \langle 0|\psi_i(\xi)|P_h S_h, X\rangle\langle P_h S_h, X|\bar{\psi}_j(0)|0\rangle \quad , \end{aligned} \tag{2.32}$$

where the conservation of 4-momentum between $k = p + q$ and the momenta P_h and P_X can be used to create a new parameter z which, after neglecting transverse hadron momentum (i.e. $P_{h\perp} \ll Q^2$ [Bac02]), relates P_h to k:

$$k^- = \frac{P_h^-}{z} \quad . \tag{2.33}$$

In the hadron-nucleon collinear system the hadron moves in the opposite direction to the nucleon and therefore the P_h^- component is the dominant contribution. In the laboratory system this relation can be translated to the involved energies which gives the well known interpretation of z being the fraction of the energy transferred by the virtual photon which is contained in the detected hadron:

$$z \overset{lab}{=} \frac{E_h}{q_0} = \frac{E_h}{\nu} \quad . \tag{2.34}$$

Similar to the classification of the distribution functions in the quark-quark correlator (section 2.3) it is now possible to classify the different fragmentation functions by traces over the according Lorenz projectors acting on the fragmentation matrix. The vector component can therefore be found at leading order by the trace over $\gamma^-\Xi$ and gives the unpolarized fragmentation function

$$\begin{aligned} D_1^h(z) &= \frac{z}{4}\int \frac{d^4k}{(2\pi)^4}\, Tr(\gamma^-\Xi)\,\delta(k^- - P_h^-/z) \\ &= \frac{z}{4}\sum_X \int \frac{d\xi^+}{2\pi}\, e^{iP_h^-\xi^+/z} \\ &\qquad \times \langle 0|\psi(\xi^+, 0, \mathbf{0}_\perp)|P_h S_h, X\rangle\langle P_h S_h, X|\bar{\psi}(0)\gamma^-|0\rangle \quad . \end{aligned} \tag{2.35}$$

The other fragmentation functions are calculated accordingly by the other Lorentz matrix combinations.

Since in this chapter intrinsic transverse momentum of the quarks is still neglected, the according cross section will also be integrated over the transverse hadron momentum $P_{h\perp}$ and thus can only depend on the inclusive variables x and Q^2 and the semi-inclusive variable z.

3

Transversity and Sivers distribution functions and the Collins fragmentation function

Since the main goal of this work is the analysis of single spin asymmetries which relate to either transversity in conjunction with the Collins fragmentation function or to the Sivers function it is appropriate to go into further detail in the theoretical definitions of these functions. The basics of semi-inclusive DIS have been described in the previous chapter. In comparison to the more fundamental description of the last chapter this chapter will teleologically arrive at the expressions needed for the analysis following in later chapters. Now the special properties of transversity will be addressed and the quark model will be expanded to include also intrinsic transverse momentum dependent functions. First the essential properties of the transversity distribution are presented. After introducing intrinsic transverse momentum dependent distribution and fragmentation functions the most prominent members, the Collins function and the Sivers function are specified further. The fact that both are also naive T-odd leads to single spin asymmetries observable in SIDIS. Aspects of universality and positivity limits on these functions are discussed at the end of the chapter.

3.1 Transversity

3.1.1 Tensor charge of the nucleon

The definition of the Transversity distribution $\delta q(x)$ has been given in equation 2.31. In leading twist the whole quark-quark correlator reads

$$\Phi(x) = \frac{1}{2}\left(q(x)\not{P} + \lambda \Delta q(x)\gamma_5 \not{P} + \delta q(x) \not{P} \gamma_5 \not{S}_\perp\right) \tag{3.1}$$

after integration over the intrinsic quark momentum. λ is the helicity of the nucleon. When also integrating over x the correlator contains the charges related to the corresponding Lorentz structures which are defined as follows:

$$\Phi = \frac{1}{2}\left(g_V \not{P} + \lambda g_A \gamma_5 \not{P} + g_T \not{P} \gamma_5 \not{S}_\perp\right) \quad , \tag{3.2}$$

where g_V is the vector charge, g_A is the axial charge and g_T is the tensor charge of the nucleon. Using the definition of the quark distribution functions (eqs. 2.27, 2.30 and 2.31) the charges can be identified as integrals over x summed over quark and corresponding antiquark:

$$\begin{aligned}
q = g_V = \quad & \textstyle\int_{-1}^{+1} dx\, q(x) & = \int_0^1 dx\,[q(x) - \bar{q}(x)]\ , \qquad & (3.3)\\
\Delta q = g_A = \quad & \textstyle\int_{-1}^{+1} dx\, \Delta q(x) & = \int_0^1 dx\,[\Delta q(x) + \Delta\bar{q}(x)]\ , \qquad & (3.4)\\
\delta q = g_T = \quad & \textstyle\int_{-1}^{+1} dx\, \delta q(x) & = \int_0^1 dx\,[\delta q(x) - \delta\bar{q}(x)] \quad , \qquad & (3.5)
\end{aligned}$$

where use of the charge conjugation of the correlators and respectively the distributions has been made [BR]. Since g_V and g_T contain the difference of quark and antiquark distributions these charges are determined by the valence quark content of the nucleon; the vector charge for the proton thus gives 2 for u quarks and 1 for d quarks (and vice versa for the neutron) being just the numbers of valence quarks present in the nucleon. While the axial and the vector charge have been determined quite well experimentally the tensor charge was only calculated theoretically by different models such as the MIT bag model (MIT) [JJ92, Str93], the chiral color-dielectric model (CDM) [BCD97], the chiral quark soliton model (CQSM) [KPG96b, WK99], perturbative QCD analyses (CQM,LC) [SW98, SS97], the spectator diquark model (Spect.) and Lattice calculations (Latt.) [FKOU95, ADHK97].

These models give quite different results although the general magnitudes are at least similar (i.e. δu somewhat below 1 and positive while δd is around -0.2) as can be seen in table 3.1 where the first row gives the expectations of a non-relativistic quark model (NRQM). It is therefore of great interest to extract the tensor charge experimentally as well. Additionally, the sum of the axial charges over the quarks, $\Delta\Sigma = \Delta u + \Delta d + \cdots$, which is the contribution of the quark spins to the spin of the nucleon as mentioned in the introduction, is displayed in this table.

Table 3.1: Summary of axial and tensor charges in various models as presented in [BDR02]. Some of the tensor charges were evolved in LO QCD from the intrinsic scale of the models (Q_0^2) to $Q^2 = 10\,\mathrm{GeV}^2$ to give a comparable scale for all models.

Model [Ref.]	Δu	Δd	$\Delta\Sigma$	δu	δd	$\lvert\delta u/\delta d\rvert$	Q_0[GeV]	$\delta u(Q^2)$	$\delta d(Q^2)$
NRQM	1.33	-0.33	1	1.33	-0.33	4.00	0.28	0.97	-0.24
MIT [JJ92]	0.87	-0.22	0.65	1.09	-0.27	4.04	0.87	0.99	-0.25
CDM [BCD97]	1.08	-0.29	0.79	1.22	-0.31	3.94	0.40	0.99	-0.25
CQSM1 [KPG96a]	0.90	-0.48	0.37	1.12	-0.42	2.67	0.60	0.97	-0.37
CQSM2 [WK99]	0.88	-0.53	0.35	0.89	-0.33	2.70	0.60	0.77	-0.29
CQM [SW98]	0.65	-0.22	0.43	0.80	-0.15	5.33	0.80	0.72	-0.13
LC [SS97]	1.00	-0.25	0.75	1.17	-0.29	4.03	0.28	0.85	-0.21
Spect. [JMR97]	1.10	-0.18	0.92	1.22	-0.25	4.88	0.25	0.83	-0.17
Latt. [FKOU95, ADHK97]	0.64	-0.35	0.29	0.84	-0.23	3.65	1.40	0.80	-0.22

3.1.2 Helicity and transverse spin basis

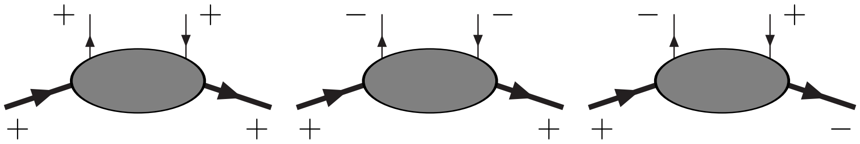

Figure 3.1: The three helicity amplitudes $\mathcal{A}_{++,++}, \mathcal{A}_{+-,+-}$ and $\mathcal{A}_{+-,-+}$ of the quark in the nucleon

When looking at the definition of transversity in equation 2.31 it becomes clear that the combination of the two regular gamma matrices with the γ^5 matrix gives a tensor component of the quark-quark correlator. It can be shown [Jaf97] that the distribution functions can be expressed in the quark helicity basis by three helicity amplitudes which are left over after applying helicity conservation, parity invariance and time-reversal invariance. The quark distribution functions $q(x)$ and $\Delta q(x)$ can be related to the two quark helicity conserving amplitudes to be

$$q(x) = \quad q_+(x) + q_-(x) \quad \sim \mathrm{Im}(\mathcal{A}_{++,++} + \mathcal{A}_{+-,+-})\,, \tag{3.6}$$

$$\Delta q(x) = \quad q_+(x) - q_-(x) \quad \sim \mathrm{Im}(\mathcal{A}_{++,++} - \mathcal{A}_{+-,+-})\,, \tag{3.7}$$

where $+(-)$ represents the positive (negative) helicity of either the quark or the nucleon as illustrated in 3.1. The transversity distribution can be identified with the third amplitude which is non-diagonal in the helicity basis

$$\delta q(x) \quad \sim \mathrm{Im}\mathcal{A}_{+-,-+} \quad , \tag{3.8}$$

where the helicity flips. For the large (and thus leading) light-cone components of the quark spinor helicity and chirality are the same [Jaf97] and such a chiral-odd process in inclusive DIS is prohibited by helicity conservation when assuming negligible current quark masses. This can be understood since helicity is a conserved quantity for nearly massless particles and therefore a helicity flip is suppressed by m/Q^2, as displayed in Fig. 3.2.

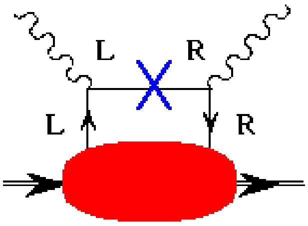

Figure 3.2: Forward Compton scattering diagram of the forbidden helicity flip amplitude.

Furthermore in the helicity basis transversity does not even have a probabilistic interpretation. This *problem* can be overcome by changing into the quark transverse spin basis $|\uparrow\rangle(|\downarrow\rangle)$ defined by the linear combinations of the quark helicity states $\frac{1}{\sqrt{2}}(|+\rangle \pm i|-\rangle)$. In

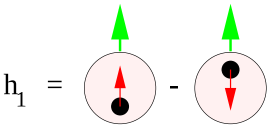

Figure 3.3: Illustration of the transversity quark distribution with respect to the transverse spin ↑ of quark and nucleon

this basis the probabilistic interpretation of the amplitudes is regained, defining transversity as the difference of the probability to find quarks with spin parallel to the spin of the transversely polarized nucleon and that of finding quarks with spin antiparallel, as illustrated in Fig. 3.3:

$$\delta q(x) = \quad q_{\uparrow}(x) - q_{\downarrow}(x) \quad \sim \mathrm{Im}(\mathcal{A}_{\uparrow\uparrow,\uparrow\uparrow} - \mathcal{A}_{\uparrow\downarrow,\uparrow\downarrow}) \, . \tag{3.9}$$

Note that in the transverse spin basis the quark helicity distribution corresponds to a non-diagonal amplitude.

The other problem, that transversity is not measurable in inclusive DIS, can be overcome by including another chiral-odd object to ensure helicity conservation. As an example it can be measured in transversely-polarized Drell-Yan (DY) [DY70] processes where the combination of a quark and an antiquark transversity distribution can be observed [JJ92]. Another combination applicable also in semi-inclusive DIS is the combination with a chiral-odd fragmentation function. Since the only relevant leading twist function depends on the intrinsic transverse momentum created in the fragmentation process, that concept will be explained in the next section before explaining the fragmentation function in greater detail.

In addition to its chiral-odd property, the transversity distribution function is also special under QCD evolution aspects which is the evolution of the distribution functions from one scale Q_1^2 to a different scale Q_2^2 taking into account higher order diagrams in the strong coupling α_S. These higher order corrections are necessary as emissions of gluons and quark-antiquark pairs created by the gluons have to be included in the process. Absorption of all possible effects into the quark-photon vertex creates a scale dependency which is commonly calculated by the DGLAP equations [Dok77, GL72, AP77]. Since a transversity distribution for gluons does not exist in a nucleon due to an impossible helicity flip of 2 for a spin-half target, the gluons cannot couple to quark transversity. This of course influences the Q^2 evolution of transversity. So, even if at some scale Q_1^2 the transversity distribution and the helicity distribution would coincide, this does not need to be the case at a different scale Q_2^2. Of course, since the deuteron is a spin 1 object, here gluon transversity can exist.
The question why such a chiral-odd function exists at all in the nucleon is assumed to be related to the chiral symmetry breaking in QCD, since one also needs a mass insertion in the nucleon to flip the helicities between incoming and outgoing quark. This can, as demonstrated before, be only achieved by a mass insertion to the corresponding quarks inside the nucleon. Such an interaction can take place with a scalar object changing the helicities. This is exactly the kind of process used to create the chiral symmetry breaking as for example predicted by instantons as classical, topological solutions to the QCD vacuum.

3.2 Transverse momentum dependent distribution and fragmentation functions

In the SIDIS cross section as defined in section 2.4 the transverse momentum of the outgoing hadron(s) has been integrated out to arrive at a differential cross section of the variables x, z and Q^2 or $y = \frac{P_\mu q^\mu}{P_\nu l^\nu} \overset{lab}{=} \frac{\nu}{E}$, which is the fractional energy transfer of the photon. In a more general description of semi-inclusive processes one also has to include the transverse momentum of the hadrons $\mathbf{P}_{h\perp}$ which in combination with the included angle of the lepton scattering plane with respect to the target polarization gives three degrees of freedom more, resulting in a 6-fold differential cross section:

$$\frac{d\sigma^6}{dx dy dz d\phi_S d\phi dP_{h\perp}} =: d\sigma^6 \quad , \tag{3.10}$$

which will commonly be abbreviated as $d\sigma^6$ bearing in mind its dependencies. Generally one defines the 2 transverse momentum variables by their absolute value $P_{h\perp}$ and by the azimuthal angle ϕ of the outgoing hadron with respect to the lepton scattering plane along the common axis of the virtual photon direction (see Fig. 3.4). The azimuthal angle of the transverse target polarization component with respect to the lepton scattering plane ϕ_S is calculated similarly. Note that this angular definition contains an extra sign relative to the definition in theory papers; therefore all cross sections containing odd functions of the azimuthal angles will have the inverse sign in comparison to the theory descriptions [MT96, Bac02]. The transverse momentum has to be generated within the semi-inclusive processes.

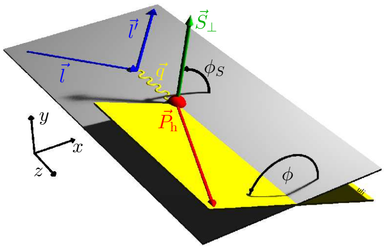

Figure 3.4: Definition of the azimuthal angles ϕ and ϕ_S

This can either happen in the quark distribution part where the struck quark contained some intrinsic transverse momentum $\mathbf{p}_T$ or during the fragmentation process where the fragmenting hadron gained intrinsic transverse momentum $\mathbf{K}_T = -z\mathbf{k}_T$ [Bac02]. Therefore the concept of distribution and fragmentation functions has to be expanded to depend not only on x or z when leaving out Q^2 dependencies, but also on their intrinsic transverse momenta. Any semi-inclusive cross section which before depended only on the distribution function and a fragmentation function contains two convolution integrals which take care of the transverse momentum. The unpolarized cross section part depending on $q(x, \mathbf{p}_T)$ and $D_1(z, \mathbf{k}_T)$, following [MT96] thus reads:

$$\frac{d\sigma^6}{dxdydzd\phi_S d^2\mathbf{P}_{h\perp}} = \frac{2\alpha^2}{s} A(x,y) \sum_q e_q^2 \mathcal{I}\left[q(x,\mathbf{p}_T) D_1(z,\mathbf{k}_T)\right] \quad , \tag{3.11}$$

where the convolution integral over the intrinsic momenta has been abbreviated as

$$\mathcal{I}[\cdots] = \int d^2\mathbf{p}_T d^2\mathbf{k}_T \delta^{(2)}\left(\mathbf{p}_T - \frac{\mathbf{P}_{h\perp}}{z} - \mathbf{k}_T\right)[\cdots] \tag{3.12}$$

and $s = (P_\mu + q_\mu)(P^\mu + q^\mu) = Q^2/xy$ is the center of mass energy squared. The kinematic pre-factor $A(x,y)$ as well as further pre-factors which will appear in the following sections are defined as

$$A(x,y) = \frac{1}{xy^2}\left((1-y)\frac{1+R(x,y)}{1+\gamma^2(x,y)} + \frac{y^2}{2}\right) \tag{3.13}$$

$$B(x,y) = \frac{1}{xy^2}(1-y) \tag{3.14}$$

$$C(x,y) = \frac{1}{xy^2}2(1-y)\sqrt{1-y} \quad , \tag{3.15}$$

as given in [MT96] but taking into account the fact that the Callan-Gross relation, equation 2.28, has to be corrected at momentum transfers of HERMES. In fact, the unpolarized cross section σ_{UU} measured with an unpolarized beam is the sum of the cross sections for longitudinally and transversely polarized virtual photon scattering [DCS] $\sigma_{UU} = \sigma_L + \sigma_T$ which is proportional to F_2 while F_1 only relates to σ_T. The factor R is defined as [Rob]:

$$R := \frac{\sigma_L}{\sigma_T} = \frac{(1+\gamma^2)F_2 - 2xF_1}{2xF_1} \quad , \tag{3.16}$$

with $\gamma = Q/\nu$ and relates the measured unpolarized cross section to $F_1 = \sum_q e_q^2 q(x)$, which is the quantity one is interested in:

$$\frac{F_2}{2x} = F_1 \cdot \frac{1+R}{1+\gamma^2} \quad . \tag{3.17}$$

The R ratio has be measured at experiments which are sensitive to this distinction and can be looked up in a parameterized way [WRB+90, A+99].

The distribution and fragmentation functions mentioned already in chapter 2 are expected to have a Gaussian distribution with a width of around 0.44-0.5 GeV for the intrinsic transverse momenta before integrating over them. The transverse momentum dependent functions presented in the following are likely to be Gaussian shaped as well, but cannot have the same widths as the previously mentioned functions as this could spoil positivity limits. This will become clear soon.

3.2.1 Collins function

The possibility to measure the chiral-odd transversity distribution in DIS relies on a chiral-odd fragmentation function to regain helicity conservation. At leading twist for one particle inclusive DIS of unpolarized outgoing hadrons one chiral-odd function is the so-called Collins function first proposed by Collins [Col93]. Just as for the unpolarized fragmentation function $D_1(z)$, it is possible to extract the chiral-odd fragmentation functions by applying the according Lorentz trace on the quark fragmentation matrix and integration over the non-transverse components of the intrinsic quark momentum:

$$\begin{aligned}
\frac{1}{4z}\int \frac{dk^+dk^-}{(2\pi)^4}\, Tr(\sigma^{i-}\gamma_5\,\Xi)\,\delta(k^- - P_h^-/z) \quad &= \\
S_{hT}^i\,\Delta_T' D(z,\mathbf{k}_T^2) + \frac{\lambda_h}{M_h}\,k_T^i H_{1L}^\perp(z,\mathbf{k}_T^2)& \\
-\frac{1}{M_h^2}\left(k_T^i k_T^j + \frac{1}{2}\,\mathbf{k}_T^2\, g_\perp^{ij}\right) S_{hTj}\, H_{1T}^\perp(z,\mathbf{k}_T^2)& \\
+\frac{1}{M_h}\,\varepsilon_T^{ij} k_{Tj}\, H_1^\perp(z,\mathbf{k}_T^2)& \quad ,
\end{aligned} \tag{3.18}$$

where M_h is the mass of the produced hadron h. The different fragmentation functions are defined as in [MT96] and represent the different possibilities to find unpolarized hadrons originating from quarks with their polarizations longitudinally (L) or transversely (T) with respect to the virtual photon direction. Since the interest of this thesis lies in the measurement of transversity ($\delta q(x)$) which couples in leading twist only to the Collins function $H_1^{\perp}(z, \mathbf{k}_T^2)$ the other fragmentation functions are not further discussed. To include also this function in equation 3.18 time reversal symmetry was not applied. The part of the cross section containing the transversity distribution when scattering an unpolarized (U) lepton beam on a transversely polarized (T) target thus reads:

$$d^6\sigma_{UT} \quad = -\textstyle\sum_q \frac{2\alpha^2 e_q^2}{s} |\mathbf{S}_T| B(x,y) \sin(\phi + \phi_S) \mathcal{I}\left[\frac{\mathbf{k}_T \cdot \hat{\mathbf{P}}_{h\perp}}{M_h} \delta q(q, \mathbf{p}_T^2) H_1^{\perp q}(z, \mathbf{k}_T^2)\right] \quad . \quad (3.19)$$

The fact that the absolute value of the target spin transverse to the virtual photon **S** appears takes into account that in an experiment the target will be polarized with respect to the lepton beam which does not coincide with the direction of the virtual photon. The $\sin(\phi + \phi_S)$ modulation arises since the Collins mechanism is sensitive to the orientation to the lepton scattering plane because the produced hadron gains transverse momentum in the fragmentation process.

3.2.2 Sivers function

Another important transverse momentum dependent function is the Sivers function, first proposed by Sivers [Siv90] to describe single spin asymmetries observed in pion production in *pp* scattering. It appears in the quark-quark correlator when not integrating over intrinsic transverse momentum of the outgoing quark. Also time-reversal symmetry has not been applied to the correlator. Since it gives the probability to find an unpolarized quark in a transversely polarized nucleon it is part of the γ^+ trace of the quark correlation matrix.

$$\begin{aligned} \frac{1}{2}\int \frac{dp^+\,dp^-}{(2\pi)^4}\, Tr(\gamma^+\,\Phi)\,\delta(p^+ - xP^+) = \\ \cdots - \frac{\varepsilon_T^{ij} p_{Ti} S_{Tj}}{M}\, f_{1T}^{\perp}(x, \mathbf{p}_T^2)\,, \end{aligned} \qquad (3.20)$$

where $f_{1T}^{\perp}(x, \mathbf{p}_T^2)$ is the Sivers function as defined in [BM98]. The cross section for an unpolarized lepton beam and a transversely polarized target, containing the Sivers function is then

$$d^6\sigma_{UT} = -\sum_q \frac{2\alpha^2 e_q^2}{s} |S_T| A(x,y) \sin(\phi - \phi_S) \mathcal{I}\left[\frac{\mathbf{p}_T \cdot \hat{\mathbf{P}}_{h\perp}}{M} f_{1T}^{\perp q}(x, \mathbf{p}_T^2) D_1^q(z, \mathbf{k}_T^2)\right] \quad . \quad (3.21)$$

The $\sin(\phi - \phi_S)$ modulation which is independent of the scattering plane is caused by the intrinsic transverse momentum of the quarks in the nucleon which is then transferred to the outgoing hadron. The existence of functions depending on the transverse momentum of the quarks inside the nucleon implies that these quarks also have a non-vanishing orbital angular momentum which is one of the still missing pieces in the spin puzzle mentioned in the introduction. Unfortunately no direct relation between the Sivers and other similar functions (e.g. $h_1^\perp$) to the angular momentum contribution of the quarks to the nucleon spin could be established, yet. A sum rule to calculate the angular momentum contribution of quarks and gluons from generalized parton distributions [Ji97b] exists, but this is not the subject of the analysis presented. A few model calculations [MPXZ89, Bur02] nevertheless suggest a relation between such a sine modulation and the angular momentum of quarks and possibly also the gluons [Bur04]. Some of these models will later be discussed when interpreting the obtained results in chapter 6.

3.2.3 Further transverse momentum dependent functions

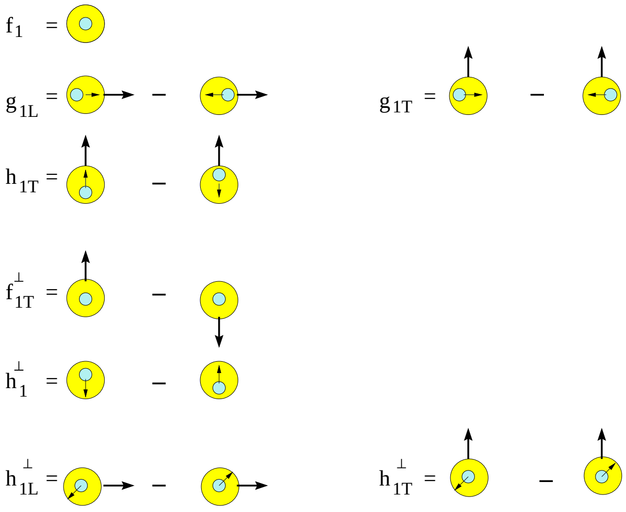

Figure 3.5: Leading twist transverse momentum dependent quark distribution functions visualized by the spin orientation of the nucleon and the quark relative to a virtual photon entering horizontally from the left

Additionally also other transverse momentum dependent and some higher twist functions appear in the semi-inclusive DIS processes analyzed. All of the leading twist distribution functions are depicted in Fig. 3.5, where nucleon and quark spin for each of the functions are displayed relative to a virtual photon entering from the left. Some functions of importance for the analysis to be presented are:

- $h_1^\perp$ which describes transversely polarized quarks in an unpolarized nucleon. As a consequence it is part of the unpolarized cross section and hence will appear in any asymmetry in the denominator:

$$\begin{aligned} d^6\sigma_{UU} &= \sum_q \frac{2\alpha^2 e_q^2}{s} |S_T| B(x,y) \cos(2\phi) \\ &\times \ \mathcal{I}\left[\frac{2(\mathbf{p}_T\cdot\hat{\mathbf{P}}_{h\perp})(\mathbf{k}_T\cdot\hat{\mathbf{P}}_{h\perp}) - \mathbf{p}_T\cdot\mathbf{k}_T}{MM_h} h_1^{\perp q} H_1^{\perp q}\right] . \end{aligned} \tag{3.22}$$

- $h_{1L}^{\perp}$ as well as interaction dependent higher twist functions $\tilde{h}_1$ and $\tilde{H}_1$, which appear in the longitudinally polarized cross section
$$\begin{aligned} d^6\sigma_{UL} &= -\sum_q \frac{2\alpha^2 e_q^2}{s}\,|S_L| \Bigg\{ B(x,y)\sin(2\phi) \\ &\times\ \mathcal{I}\left[\frac{2(\mathbf{p}_T\cdot\hat{\mathbf{P}}_{h\perp})(\mathbf{k}_T\cdot\hat{\mathbf{P}}_{h\perp}) - \mathbf{p}_T\cdot\mathbf{k}_T}{MM_h}\,h_{1L}^{\perp q}H_1^{\perp q}\right] \qquad (3.23) \\ &-\ C(x,y)\sin(\phi)\frac{1}{Q}\Big(\mathcal{I}\left[....h_{1L}^{\perp q}H_1^{\perp q}\right] \\ &+\ \mathcal{I}\left[....\tilde{h}_L^{\perp q}H_1^{\perp q}\right] + \mathcal{I}\left[....h_{1L}^{\perp q}\tilde{H}_1^{q}\right]\Big)\Bigg\} \qquad (3.24) \end{aligned}$$
Even though some of these functions are higher twist, they can become sizeable when leading twist functions are for example suppressed by a comparatively small transverse spin component as in eq. 3.19, if scattering on longitudinally polarized nucleons.

- $h_{1T}^{\perp}$ also shows up in the transversely polarized cross section in leading twist, but due to the higher polynomials in the intrinsic transverse momenta it is expected to be suppressed. Also the interaction dependent higher twist functions $\tilde{h}_T^q, \tilde{h}_T^{\perp q}, \tilde{h}_{1L}^{\perp q}$ and $\tilde{H}^q$ appear
$$\begin{aligned} d^6\sigma_{UT} &= -\sum_q \frac{2\alpha^2 e_q^2}{s}\,|S_T| B(x,y)\sin(3\phi-\phi_S) \qquad (3.25) \\ &\times\ \mathcal{I}\left[\frac{4(\mathbf{p}_T\cdot\hat{\mathbf{P}}_{h\perp})^2(\mathbf{k}_T\cdot\hat{\mathbf{P}}_{h\perp}) - 2(\mathbf{p}_T\cdot\hat{\mathbf{P}}_{h\perp})(\mathbf{p}_T\cdot\mathbf{k}_T)}{2M^2M_h}\,h_{1T}^{\perp q}H_1^{\perp q}\right] . \end{aligned}$$

3.3 Single spin asymmetries and the relation to T-odd functions

3.3.1 Single spin asymmetries

As we have seen in the last sections both the Collins function as well as the Sivers function cause a sine modulation depending on the sum (amplitude proportional to $\delta q(x,\mathbf{p}_T)\cdot H_1^{\perp}(z,\mathbf{k}_T)$) or the difference (amplitude proportional to $f_{1T}^{\perp}(x,\mathbf{p}_T)\cdot D_1(z,\mathbf{k}_T)$) of the azimuthal angles from the produced hadron and the target spin with respect to the lepton scattering plane. This results in observable single spin azimuthal asymmetries (SSAs) in SIDIS, which are calculated from the difference in count rates of pseudo-scalar hadrons in two opposite spin states divided by the sum. For the case of an unpolarized lepton beam and a transversely polarized target this reads:
$$A_{UT} = \frac{1}{\langle P\rangle}\frac{N^{\uparrow}(x,z,\phi,\phi_S) - N^{\downarrow}(x,z,\phi,\phi_S)}{N^{\uparrow}(x,z,\phi,\phi_S) + N^{\downarrow}(x,z,\phi,\phi_S)}\,, \qquad (3.26)$$

where $\langle P\rangle$ is the average target polarization .

The numerator of this asymmetry consists of

$$\begin{aligned} -\textstyle\sum_q e_q^2\,|\mathbf{S}_T| \Bigg\{ & B(x,y)\sin(\phi+\phi_S)\,\mathcal{I}\left[\tfrac{\mathbf{k}_T\cdot\hat{\mathbf{P}}_{h\perp}}{M_h}\, h_1^q H_1^{\perp q}\right] \\ & + A(x,y)\sin(\phi-\phi_S)\,\mathcal{I}\left[\tfrac{\mathbf{p}_T\cdot\hat{\mathbf{P}}_{h\perp}}{M}\, f_{1T}^{\perp q} D_1^q\right] + B(x,y)\sin(3\phi-\phi_S) \\ & \times\mathcal{I}\left[\tfrac{4(\mathbf{p}_T\cdot\hat{\mathbf{P}}_{h\perp})^2(\mathbf{k}_T\cdot\hat{\mathbf{P}}_{h\perp})-2(\mathbf{p}_T\cdot\hat{\mathbf{P}}_{h\perp})(\mathbf{p}_T\cdot\mathbf{k}_T)-\mathbf{p}_T^2(\mathbf{k}_T\cdot\hat{\mathbf{P}}_{h\perp})}{2M^2M_h}\, h_{1T}^{\perp q} H_1^{\perp q}\right] \Bigg\}, \end{aligned} \tag{3.27}$$

while the denominator is

$$\begin{aligned} \textstyle\sum_q e_q^2 \Bigg\{ & A(x,y)\,\mathcal{I}\left[f_1^q(x,\mathbf{p}_T^2) D_1^q(z_h,z_h^2\mathbf{k}_T^2)\right] - B(x,y)\cos 2\phi \\ & \times\mathcal{I}\left[\tfrac{2(\mathbf{p}_T\cdot\hat{\mathbf{P}}_{h\perp})(\mathbf{k}_T\cdot\hat{\mathbf{P}}_{h\perp})-\mathbf{p}_T\cdot\mathbf{k}_T}{MM_h}\, h_1^{\perp q}(x,\mathbf{p}_T^2) H_1^{\perp q}(z_h,z_h^2\mathbf{k}_T^2)\right] \Bigg\}. \end{aligned} \tag{3.28}$$

3.3.2 Naive T-odd functions

These SSAs are left-right asymmetries which originate from the flipping of the transverse nucleon polarization. Should not CPT invariance in general and especially time reversal invariance forbid the existence of such an asymmetry? They should of course, but it can be possible to create an interference for example by a final state interaction which leads to an asymmetry. Such final state interactions have already been observed in pion-proton scattering some 30 years ago and therefore the possibility to have a non-vanishing Collins function became accepted. The Sivers function on the other hand created some controversy on whether it should exist at all. Both the Sivers and the Collins function do only appear in the traces of the corresponding correlators when allowing naive time reversal, that is time reversal without interchange of initial and final state, to be broken. Time reversal changes the nucleon state $|P,S\rangle$ into $|-P,-S\rangle$ while naive time reversal just interchanges the initial state to $|P,-S\rangle$. Therefore these functions are not completely T-odd and can in general be nonzero. The Collins proof that T-odd functions have to be zero [Col93] is thus still valid but does not apply to naive T-odd functions. Such a function can also be understood as a final state interaction created in this case by the interference of a soft gluon which is necessary to regain color gauge invariance [BHM$^+$02, BJY03] which was at that time claimed to break factorization. [Col02, JY02] showed that it is at least possible to absorb the soft gluon part into the definition of the distribution function (Sivers) or fragmentation function (Collins).

The quark-quark correlator defined in equation 2.24 relates a quark and an antiquark at two different space-time points. As described in section 2.1 quark fields are colored objects and hence two quarks separated by a distance ξ must have a gauge link, e.g. a gluon field connecting them to become colorless. The correlator has to be modified accordingly to:

$$\Phi_{ij}(k,P,S) = \int d^4\xi\, e^{ik\cdot\xi}\,\langle PS|\bar{\psi}_j(0)\mathcal{U}(0,\xi)\psi_i(\xi)|PS\rangle \quad , \tag{3.29}$$

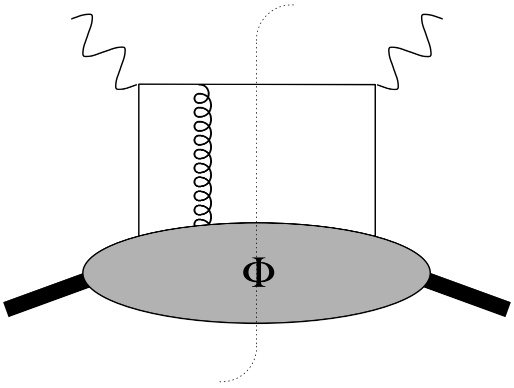

Figure 3.6: One gluon gauge link.

where

$$\mathcal{U}(0,\xi) = \mathcal{P}\exp(ig\int_{\xi}^{0} ds^{\mu}A_{\mu}) \tag{3.30}$$

is the path ordered ($\mathcal{P}$) exponential over the gauge field. As an assumption the interference of the handbag diagram with the 1-gluon diagram as illustrated by the additional gluon line in Fig. 3.6 can be taken to create a non-vanishing Sivers function although one has to bear in mind that in fact any number of gluons contributes.

3.3.3 Moments and factorization

In all the transverse momentum dependent cross sections the transverse momentum dependent functions appear within the convolution integrals over the transverse momenta involved. Since this convolution integrals cannot always be disentangled without assumptions it will be convenient to define moments of the transverse momentum dependent functions including extra powers of the momentum involved in this function. Hence the nth Sivers moment upon $\mathbf{p}_T$ integration is defined as

$$f_{1T}^{\perp(n)}(x) \equiv \int d\mathbf{p}_T^2 \left(\frac{\mathbf{p}_T^2}{2M^2}\right)^n f_{1T}^{\perp}(x,\mathbf{p}_T) \quad , \tag{3.31}$$

where n can be any integer. The mass M is the mass scale corresponding to the distribution function and is thus conventionally set to the nucleon mass. Additionally also the (1/2) moment is defined which is built with the weight $\sqrt{\left(\frac{\mathbf{p}_T^2}{4M^2}\right)}$ which differs by a factor of $\sqrt{2}$ from the definition of the other moments as in equation 3.31.

Similarly the nth Collins moment upon $\mathbf{k}_T$ integration is defined as

$$H_1^{\perp(n)}(z) \equiv \int d\mathbf{k}_T^2 \left(\frac{\mathbf{k}_T^2}{2M_h^2}\right)^n H_1^{\perp}(z,\mathbf{k}_T) \quad . \tag{3.32}$$

Here M_h corresponds to the mass of the produced hadron (i.e. the pion or kaon mass) since the process happens during the fragmentation. The (1/2) moment is again different by $\sqrt{2}$.

Until recently no proof of factorization was available although many theoreticians believed that factorization would hold for these transverse momentum dependent functions. It has only been shown for the Qiu-Sterman effect [QS99] appearing in twist-3 pion hadroproduction. The convolution of the transverse momenta could actually spoil factorization. As an example a simple Gaussian ansatz for the intrinsic transverse momentum dependence of both distribution and fragmentation function would give in the unweighted asymmetries defined in equation 3.26 an additional term $\frac{1}{\sqrt{\langle p_T^2\rangle+\langle k_T^2\rangle}}$ where $\langle p_T^2\rangle$ and $\langle k_T^2\rangle$ are the Gaussian widths. The explicit integration can be found in appendix D. Such an extra factor would of course be no direct problem to factorization, but these widths could in principle depend on x and z respectively, such that it would be impossible to absorb this factor into either the distribution or fragmentation case. Assuming a Gaussian dependence, the unweighted asymmetries would in this case become:

$$\begin{aligned} A_{UT} \approx &= 2|S_T|\sin(\phi+\phi_S)\frac{B(x,y)\sum_q e_q^2\delta q(x)H_1^{\perp,(1/2),q}(z)/\sqrt{\langle p_T^2\rangle+\langle k_T^2\rangle}}{A(x,y)\sum_q q(x)D_1^q(z)} \\ &\quad -2|S_T|\sin(\phi-\phi_S)\frac{A(x,y)\sum_q e_q^2 f_{1T}^{\perp,(1/2),q}(x)D_1^q(z)/\sqrt{\langle p_T^2\rangle+\langle k_T^2\rangle}}{A(x,y)\sum_q q(x)D_1^q(z)} \qquad .(3.33) \end{aligned}$$

It has been argued that weighting the events with an additional $\frac{P_{h\perp}}{zM_h}$ creates asymmetries which can be calculated without assumptions on the intrinsic transverse momentum dependence [KM97]. Furthermore these asymmetries have any information on that dependencies absorbed in the 1-moments of the functions. Consequently the weighted asymmetries are probably better candidates to hold factorization [Bac04]. The $\frac{P_{h\perp}}{zM_\pi}$ weighted asymmetry gives

$$\begin{aligned} A_{UT} &= \frac{\sum_i^{N^+}\frac{P_{h\perp,i}}{M_\pi z_i}-\sum_i^{N^-}\frac{P_{h\perp,i}}{M_\pi z_i}}{N^+ + N^-} \\ &\overset{\sin(\phi+\phi_S)}{=} 2|S_T|\frac{B(x,y)\sum_q e_q^2\delta q(x)H_1^{\perp,(1),q}(z)}{A(x,y)\sum_q q(x)D_1^q(z)} \end{aligned} \qquad (3.34)$$

and accordingly for the $\frac{P_{h\perp}}{zM_N}$ case

$$A_{UT} \overset{\sin(\phi-\phi_S)}{=} -2|S_T|\frac{A(x,y)\sum_q e_q^2 f_{1T}^{\perp,(1),q}(x)D_1^q(z)}{A(x,y)\sum_q q(x)D_1^q(z)} \quad . \qquad (3.35)$$

Just recently [JMY04] claim to have proofed that factorization holds also for semi-inclusive DIS at low transverse momenta.

3.4 Positivity constraints and universality

3.4.1 Positivity

The polarized cross section cannot be larger than the unpolarized cross section. This quite simple statement can easily be understood when describing transversity in the transverse spin basis. Here, the unpolarized quark distribution function can be expressed as $q(x) = q^{\uparrow}(x) + q^{\downarrow}(x)$. Since $q^{\uparrow,\downarrow}$ can both be identified as probabilities and thus are positive, the absolute value of the transversity distribution can only be smaller or equal to the unpolarized distribution:

$$|\delta q(x)| = |q^{\uparrow}(x) - q^{\downarrow}(x)| \leq q(x) \quad . \tag{3.36}$$

From the description of transversity in the helicity basis on the amplitude level it is possible to derive an even sharper bound called Soffer bound [Sof95]

$$|\delta q(x)| \leq \frac{1}{2}(q(x) + \Delta q(x)) \quad . \tag{3.37}$$

For positive Δq and q as in the u quark case this bound is of course not stronger as equation 3.36, but for d quarks, where Δd is negative while d stays positive δd is further constrained.

Additionally the analysis of the Dirac structure of the diagrams involved allows further limits especially on the transverse momentum dependent functions [BBHM00, Bac02]:

$$\begin{aligned} |f_{1T}^{\perp(1)}(x, \mathbf{p}_T)| &\leq f_1^{(1/2)}(x, \mathbf{p}_T) & (3.38)\\ |H_1^{\perp(1)}(x, \mathbf{k}_T)| &\leq D_1^{(1/2)}(z, \mathbf{k}_T) \quad . & (3.39) \end{aligned}$$

The aforementioned Gaussian ansatz for the intrinsic transverse momentum dependencies could actually fail to fulfill these relations as applying the definition of the moments to, for example the Sivers function, gives:

$$|f_{1T}^{\perp(1)}(x, \mathbf{p}_T)| = |f_{1T}^{\perp(1/2)}(x, \mathbf{p}_T) \cdot \sqrt{\frac{\mathbf{p}_T^2}{M^2}}| \quad . \tag{3.40}$$

Factorizing out the same Gaussian for $f_{1T}^{\perp(1/2)}(x, \mathbf{p}_T)$ and $f_1^{(1/2)}(x, \mathbf{p}_T)$ and dividing by it leaves a remaining $\sqrt{\frac{\mathbf{p}_T^2}{M^2}}$ dependence which becomes large at large transverse momenta. However intrinsic transverse momenta can only contain a fraction of the total available rest energy in the nucleon $|\mathbf{p}_T^2| < M$ leaving $\sqrt{\frac{\mathbf{p}_T^2}{M^2}} < 1$ and thus fulfilling the positivity condition. Nevertheless the Gaussian ansatz can accordingly only be applicable to transverse momenta up to the order of the rest mass.

Another class of constraints on the different distribution and fragmentation functions can be obtained by the QCD analysis of integrated quantities which are related to conservation laws. These constraints are also called sum rules. The so-called Terayev-Schaefer sum rule [ST00] treats the integral over the 1^{st} moment of the Collins function integrated over the whole z-range and summed over all hadron types:

$$\sum_h \int dz\, z^2 H_1^{\perp(1)}(z) = 0 \quad ; \tag{3.41}$$

which just contains the conservation of the produced transverse momentum in the fragmentation process. This sum rule will become interesting in the context of the interpretation of the obtained experimental results.

3.4.2 Universality

The Feynman diagrams leading to the naive T-odd behavior (i.e. Fig. 3.6) of the transverse momentum dependent functions do also appear in different other processes, not only in SIDIS. The mechanism leading to the Sivers function is also visible in DY processes, except that in this case the gauge link is closed on the opposite light-like direction. This leaves a different possibility to cut the corresponding diagram resulting in an extra sign of the Sivers function [Col02], as they are connected by time reversal:

$$f_{1T,DIS}^{\perp} = -f_{1T,DY}^{\perp} \quad . \tag{3.42}$$

While this is certainly an interesting test of the underlying model in two different processes other T-odd functions may have extra contributions which make them process dependent. Studies performed by [BMP03] show that the Collins function belongs to this category where some contributions to its creation, the final state interactions, are not process dependent and thus may show the same sign in SIDIS and electron positron annihilation while gluonic pole contributions change sign as they are similar to the ones in the Sivers case. But even there such process independent contributions might occur. Nevertheless the theoretical situation on this subject is not yet settled. It will certainly be very interesting to measure and compare these functions in different processes like $pp^{\uparrow} \rightarrow hX$, DY, e^+e^- and SIDIS. The first measurements in the latter process will be addressed in the following chapters.

4

The HERMES experiment

The data presented in this thesis was obtained in the years 2002 and 2003 by the HERMES experiment with a transversely polarized Hydrogen target. The experiment is situated in the East area of the HERA (**H**adron **E**lektron **R**ing **A**nlage) ring at DESY in Hamburg, Germany. Since only the lepton beam is used in HERMES the beginning of this chapter will only describe the HERA lepton beam without discussing the proton beam. After that the internal gas target and the HERMES spectrometer itself will be presented. Here several detector quantities important for the analysis will be explained, afterwards the online monitoring system controlling the quality of the data is described. At the end of this chapter the performance of HERA II and HERMES run II and the amount of raw data are shown.

4.1 The HERA lepton beam

The HERA storage rings of 6.3 km circumference consist of two beam-pipes, one for protons, which is usually run at 920 GeV, and the other for electrons or positrons mostly run at 27.6 GeV. They intersect at the interaction regions in the experimental areas North (ZEUS) and South (H1). The main aim of these two experiments is the low x and high Q^2 behavior of the quarks in the nucleon. The beams collide with an invariant mass of $\sqrt{s} = 319$ GeV. Until 2003 HERA-B used the proton beam in the western experimental area to produce heavy mesons in order to investigate CP violations in B-meson decays.
HERMES utilizes only the lepton beam. Beam currents of up to 50 mA at the beginning of a fill have been achieved. Due to residual gas interactions the beam current decays nearly

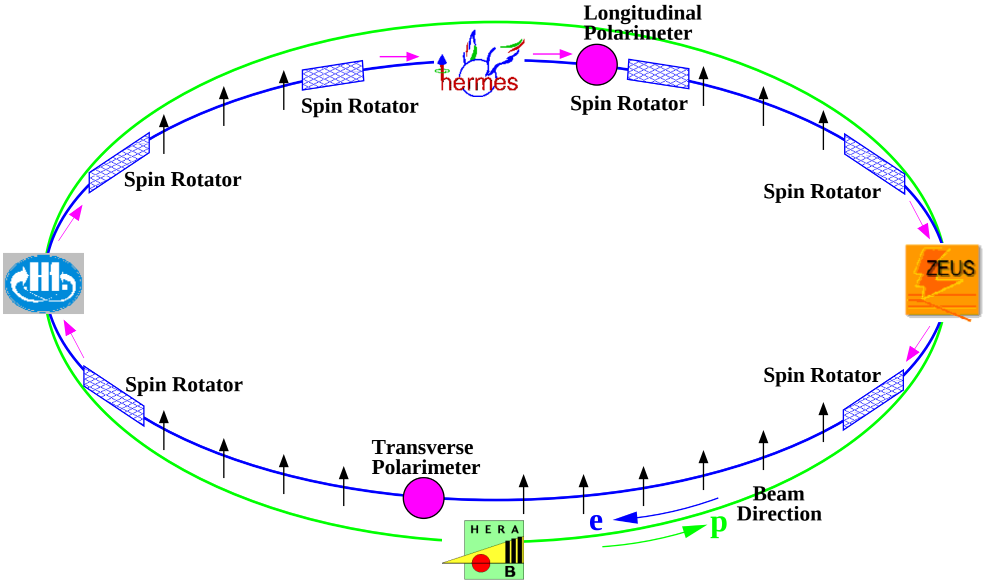

Figure 4.1: A schematic view of the HERA beams including the experiments and the spin orientation of the lepton beam after 2001.

exponentially. The average lifetime which can be derived from decay constant lies between 12 to 14 hours but usually the beam will be either dumped at around 10 to 12 mA or dumped after drastically reducing the current by inserting high density unpolarized gas in the HERMES target cell to gain statistics of unpolarized DIS important for deeply virtual Compton scattering (DVCS) and nuclear effects.

The electron beam is separated in 220 bunches of which up to 200 are filled. Generally the lepton beam polarizes itself transversely by the Sokolov-Ternov mechanism [ST64]. Spin rotators in front of and after HERMES turn the polarization to longitudinal which originally was used to measure double spin asymmetries where both the beam and the target were longitudinally polarized. This was applied in the years 1995 to 2000 in order to extract the spin structure function [Wei, A$^+$98b] and the quark helicities [Bec, A$^+$04]. For the asymmetries presented in this work no beam polarization is required which means that generally one has to ensure an unpolarized data sample by adding equal amounts of data obtained with the two longitudinal lepton polarizations. Although this was important for the longitudinal single spin asymmetries, A_{UL}, measured in the years 1996-2000 [A$^+$00, A$^+$01b, A$^+$03b] and will become important for later data again the net beam polarization during the data taking presented here was small or zero.

4.2 The HERMES target

The HERMES target consists of an open-ended elliptical target cell [B$^+$03b] which is internal to the vacuum of the HERA electron beam. This cell is continually flooded with either polarized or unpolarized gas. The advantage of a gaseous target in comparison to solid state targets is that no dilution from other atoms occurs. On the other hand a gas target suffers from a very thin target thickness resulting in reduced statistics. The target cell increases the thickness by a factor of 100 compared to a free gas jet, resulting in a thickness of 0.7 to 1.0×10^{14} nucleons/cm^2 which corresponds to a negligible impact on the total lepton beam lifetime. As can be seen in Fig. 4.2 the hydrogen atoms, which were obtained by dissociation of hydrogen gas in a plasma are nuclear polarized by the atomic beam source (ABS) [N$^+$03] which works as a Stern-Gerlach separation of the electron spin states. The two spin states $|1>:=|m_s, m_I>=|+\frac{1}{2}, +\frac{1}{2}>$ and $|2>:=|+\frac{1}{2}, -\frac{1}{2}>$ which have the same electron spin $|m_s>$ but different nuclear spin $|m_I>$ are focused by the sextupole magnets, while the two other states $|3>:=|-\frac{1}{2}, -\frac{1}{2}>$ and $|4>:=|-\frac{1}{2}, +\frac{1}{2}>$ are defocused and thus get removed by the pumps. By activating one of the two high frequency transitions, 1 → 3 or 2 → 4 it is possible to populate the 2 states with the same nuclear spin orientation. Since switching on one transition and off the other does not take much time it is possible to change the nuclear polarization every 60s while the actual switching process takes less than a second, including the removal of the target gas from the cell. This rapid switching of the target polarization reduces the possibility of systematic time-dependent errors. Once the gas reaches the target cell a magnetic holding field defines the quantization axis for the nuclear polarized states. Before 2001 this field was longitudinally oriented with respect to the lepton beam, which allowed to measure longitudinally polarized target spin asymmetries. During the shutdown in the year 2001 the magnet was replaced by a transverse target magnet (see Fig. 4.3). It is since then possible to measure transversely polarized target spin asymmetries. Such a transversal magnet field deflects all charged particles by the Lorentz force, therefore correction coils were used to stabilize the orbit of the lepton beam. Charged particles produced in DIS, which

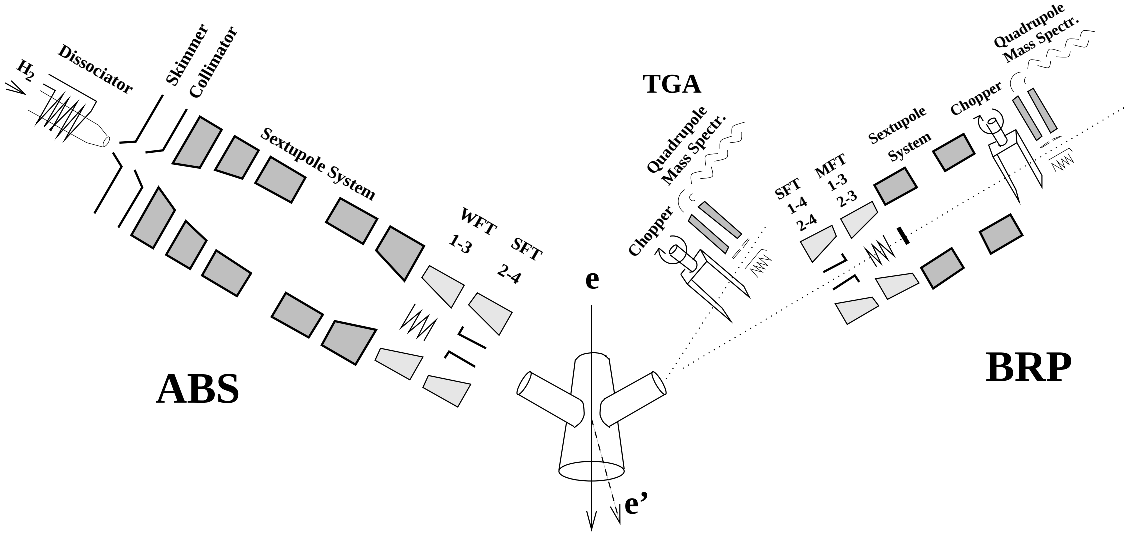

Figure 4.2: A schematic view of the polarized gas target.

Figure 4.3: A side-view of the transverse target magnet.

do not move collinearly with the beam also suffer a deflection which has to be corrected in order to calculate their kinematics. This target magnet correction (TMC) will be addressed later in this chapter.

A small fraction of the gas in the target cell is sampled by two diagnostic devices. The Breit Rabi Polarimeter (BRP) [B$^+$02] works in the opposite order as the ABS. It separates different polarization states to find the mean polarization in the target cell. In addition the composition of the gas is continously analyzed in the target gas analyzer (TGA) [B$^+$03a], which gives the degree of dissociation

$$\alpha = \frac{N_H}{N_H + 2N_{H_2}} \quad . \tag{4.1}$$

Part of the hydrogen atoms recombine [B$^+$03b] in the cell, some hydrogen molecules enter the target cell through the ABS and some originate from residual gas inside the cell and the beam vacuum. Since not all of these components are polarized, α is split into α_r, which describes the ratio of recombined molecules and α_0 which accounts for molecules injected from the ABS and the residual gas molecules.

From the value of α and the polarization value obtained from the BRP it is possible to calculate the mean polarization in the target cell.

$$P_z = \alpha_0 \left((1-\alpha_r)\beta + \alpha_r\right) P_{BRP} \,, \tag{4.2}$$

where β is the polarization of the recombined molecules. During the data taking period of 2002/2003 the average polarizations were

$$\begin{aligned} 2002\,\text{data}: \quad < P_z >= & \quad 0.783 \pm 0.041 && (4.3)\\ 2003\,\text{data}: \quad < P_z >= & \quad 0.795 \pm 0.033 \quad . && (4.4)\end{aligned}$$

4.3 The HERMES spectrometer

The HERMES experiment consists of a forward magnetic spectrometer of 2 symmetric halves on top and below the horizontal plane defined by the lepton and the proton beam pipes.

Fig. 4.4 shows a schematical side-view of the HERMES spectrometer. The lepton beam is shielded from the spectrometer magnet field by iron plates within the magnet region. In addition a correction coil has been installed within the shielding plate to compensate the remaining field components.

The spectrometer magnet itself is operated at an integrated magnetic flux of $\int dzB = 1.3\,Tm$ where the magnetic field of the dipole magnet is oriented perpendicular to the beam axis in the y-direction. The aperture of the magnet defines the acceptance for particle tracks which is $\theta_y = 140\,mrad$ in the vertical plane and $\theta_x = 170\,mrad$ in the horizontal plane. In the following the detector parts used for the analysis presented here are specified further while for the description of those components not applied for this analysis the reader is referred to [A$^+$98a]. The coordinate system used has the z-axis along the downstream direction of the lepton beam, the y axis points up while the x axis points radially outside of the ring.

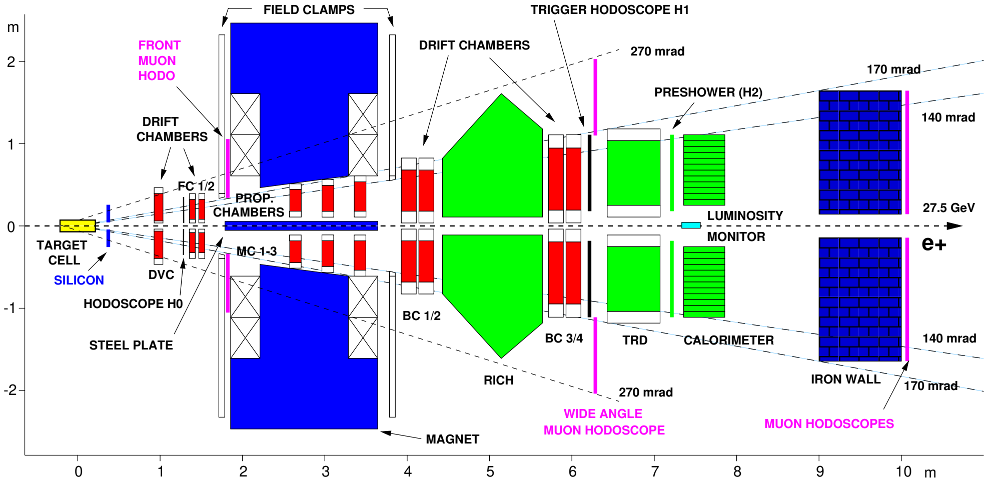

Figure 4.4: A side-view of the HERMES spectrometer as seen from inside the HERA ring.

4.3.1 Tracking

Several layers of drift chambers before and after the spectrometer magnet allow the reconstruction of tracks outside the volume where the magnetic field acts on charged particles. The setup of all drift chambers is similar where the orientations of the wires are either vertical (defined as X planes) or rotated by $\pm 30^0$ (defined as U and V planes) or shifted by half a cell width perpendicular to the corresponding plane (X',U',V' planes). Each module consists of a combination of all 3 orientations together with their shifted planes.

The front region contains the drift vertex chambers (DVC) with 6 planes in the orientation XX'UU'VV' and a spatial resolution per plane of 220 μm and the two front chambers (FC) of 6 planes each in the UU'XX'VV' configuration and a spatial resolution of 225 μm. The back region of the HERMES spectrometer contains 4 back chambers (BC) [Bera] with also

6 planes each in the same configuration as the FCs. 2 back chambers are directly after the spectrometer magnet and have an average resolution of $275\,\mu m$ and 2 chambers are situated after the dual radiator ring image Čerenkov counter with a resolution $300\,\mu m$. Out of the information from the front drift chamber signals and separately for the back drift chambers signals two partial tracks are constructed by a tree search algorithm comparing signal topologies with a look-up table [Wan]. The combination of the two partial tracks into a full track allows to define the momentum and charge of a particle track based upon the bending of the particle in the spectrometer magnet. Its momentum resolution is $\delta p/p \leq 2\%$ and its angular resolution is $\delta\theta/\theta \leq 1\%$ since 1998.

4.3.2 Particle identification

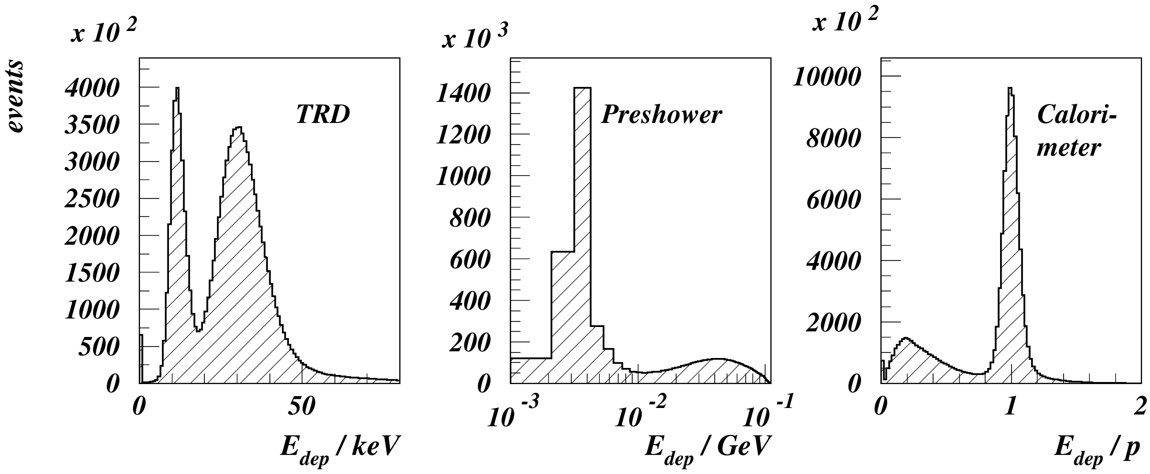

Figure 4.5: Momentum integrated energy spectra for the PID detectors TRD (left), preshower (middle) and calorimeter (right) as presented in [Wei] and based on HERMES 2000 data.

Since it is crucial to reconstruct the scattered lepton the HERMES experiment was designed to have a very clean lepton hadron separation. Four detector components allow to distinguish between these and are the basis to the particle identification (PID) which is mainly based on a different energy deposition in the applied materials. After the BCs tracks pass the transition radiation detector (TRD) which consists of an optically dense material followed by proportional tubes. The tracks produce photons at the boundary which are proportional to their Lorentz boost $\gamma = E/m$. Since the electrons are generally highly relativistic while hadrons are just relativistic particles the measured energies in the proportional chamber show two distinct peaks as can be seen in the left plot of panel 4.5.

After the TRD tracks go through the preshower detector which contains lead plates with a thickness of 11 mm and a plastic scintillator behind the plates. Particles deposit energy in the lead by radiating Bremsstrahlung and Compton photons which are then measured with the scintillator. The middle plot of Fig. 4.5 shows the energy deposition in the preshower.

The sharp peak at 2 to 3 MeV is due to hadrons while leptons deposit more energy in the lead.

Most of the energy of the particles is absorbed in the calorimeter which consists of 420 blocks of lead glass which are 50 cm long and with a cross section of $9\,cm \times 9\,cm$. While electrons lose practically all their energy in the Calorimeter hadrons only deposit part of it. To measure the energy of the particles the energy of 9 blocks is added up, where the central block is defined by the highest amount of energy deposited. The position is calculated by the mean of the energy weighted sum of the block center positions. Originally the weight $\sqrt{E_i}$ was applied but since 2002 the weight $\max\{0, 4.8 + \ln(E_i/E_{tot})\}$ is used as the spatial resolution improves with this weight [Ell]. In addition to the other detector components the Calorimeter also allows to reconstruct neutral particles such as photons originating from π^0 decays or DVCS related processes. The right plot in Fig. 4.5 displays the ratio of deposited energy in the Calorimeter and the measured momentum for charged tracks. The lepton peak around unity can clearly be distinguished from the hadron peak at ratios of 0.2 and falling off quickly.

The fourth PID detector plays only a minor role in the lepton hadron separation but enables the distinction between different hadron types. The ring image Čerenkov counter (RICH) contains silica aerogel in the front (refractive index of $n_1 = 1.03$) followed by C_4F_{10} (refractive index of $n_2 = 1.0014$) in the rest of the RICH volume. In both volumes relativistic charged particles above the threshold depending on the refractive index create Čerenkov cones which are reflected by a mirror and measured by a fine array of photomultipliers [A$^+$02b]. Since the opening angle θ of these cones is defined by $\cos\theta = \frac{1}{\beta n}$ [PSRZ] it allows to determine the velocity of the particles. Already knowing the momentum of them by the tracking detectors enables the determination of their rest mass. In this way the RICH can identify pions with more than 95% detection efficency, kaons with about 74% detection efficiency and protons with an efficiency of 53% [A$^+$02b].

All of these 4 detector responses give some information to the distinction between leptons and hadrons. Combined likelihood ratios for the 2 assumptions were created for these detector components which are defined as

$$\mathrm{PID} = \lg_{10} \frac{\mathcal{P}(e)}{\mathcal{P}(h)} \tag{4.5}$$

and are called PID values. The sum of the PID values from preshower, Calorimeter and the RICH used as an threshold Čerenkov are defined as $\mathcal{PID}_3$; the PID value of the TRD is defined as $\mathcal{PID}_5$. The combination of these 2 PID values allows a lepton and hadron detection efficency of 98%.

4.3.3 Target magnet correction

Since 2002 HERMES is running with a transversely polarized target as presented above. To keep a quantization axis for the target nucleons a magnetic holding field is necessary which is transverse to the lepton beam direction. Such a transverse field deflects charged tracks.

Therefore the angles of charged tracks measured in the spectrometer do not coincide with the angles of those charged tracks at the vertex. Expecially for the analysis presented here, which measures azimuthal asymmetries, a good knowledge of the original angles is crucial. A track correction program (**T**arget **M**agnet **C**orrection) which calls either of two routines to calculate the original angles has been developed. Those methods follow two different concepts in regaining that information, but the input data are the front track positions (x_i, y_i) and slopes (θ_i, ϕ_i) as obtained from the DVCs and FCs which are out of the magnetic field already.

HAZEX method - TMC method 1: HAZEX uses the magnetic field values as measured on the z axis and extrapolated values on the x axis to define a field map. This map is then used to generate a base set of trajectories in the following ranges:

- momentum p: $0.5 \ldots 27.5$ GeV with a step of 0.05 GeV
- z-vertex position: $-20 \ldots 20$ cm with a step of 2cm
- vertical angle θ_y: $40 \ldots 160$ mrad with a step of 20mrad
- horizontal angle θ_x: $-250 \ldots 230$ mrad with a step of 20mrad.

The distances of the observed tracks in the DVCs and FCs are compared to the base of trajectories and the base trajectories which minimize this distance are taken. Using a linear approximation between the base trajectories with the smallest differences at the DVCs and FCs the values at the vertex are accordingly approximated linearly.

Raytrace method - TMC method 2 A reference particle at some starting point is taken and transferred via some optical elements to the final point. Two coordinate systems are defined at this starting and at the end point with both being zero for the reference particle. A second particle with slightly different initial coordinates is expected to have only small differences in the final coordinates. Therefore one can Taylor expand the final position of the second particle in terms of the coordinate differences at the initial position. The expansion coefficients are called the transfer coefficients and can be calculated. One therefore tracks several particles by applying the MIT-RAYTRACE [KE] program. In the data one has to invert this transfer matrix in order to obtain the vertex coordinates from the tracked coordinates a the reference plane. This is performed iteratively by first taking some starting point, propagating that starting point to the reference plane, calculating the error vector of in the coordinates, which gives in linear approximation an error in the initial coordinates and thus improves the original guess. The procedure is repeated until convergence is reached and the vertex coordinates are known.

Both methods were tested on MC data and have been shown to work reliably. Additional tests on the track resolutions and the asymmetry reconstruction have been performed within the analysis presented here and are discussed in chapter 5. For a detailed description of TMC and the 2 methods applied see [AMS$^+$04].

4.4 Data quality

4.4.1 Data acquisition

When a detector signal is detected by several combinations of the different hodoscopes (H0, H1, H2) and the calorimeter a trigger signal is produced. If this signal is likely to be a relevant physics event the stored digitized information of all detector components will be read out with the HERMES **D**ata **AQ**uisition system (DAQ). The data is at that point still in a raw format containing only the digitized ADC and TDC values of all the channels of the detectors grouped in **D**istributed [W$^+$] **AD**AMO [Gro93] tables (DAD). The data is stored once on disks at the DESY main site and also backuped on tape in the experimental hall itself. The data structure contains several substructures. An amount of raw data of 450 MB is grouped together as a run. Since the detector information per event is always occupying the same amount of storage, roughly the same amount of events can be found per run. The amount of time it takes to collect the data for a run of course depends on the beam current as well as on the target density. These runs are further divided into bursts of around 10 seconds. This is basically a relict of the previous experiments EMC and NMC at CERN where the muons where delivered in bursts every 10 seconds. At HERMES the slowly varying detector, target and beam quantities are read out with such a frequency. The beam current and polarization as well as the target polarization and degree of dissociation are such values. This information is stored separately in the so called SLOW DAD tables.

4.4.2 Data production chain

The raw data per run still contains the ADC and TDC values in the detector components. This has to be translated into physical values by taking into account calibrations stored in DAD tables on a server. As an example a hit in a drift chamber plane contains drift times of several wires. These have to be calculated via the **S**pace **D**rift **T**ime **R**elationships into distances relative to the several wires which together give a hit pattern in each of the planes. This process of translation into hit positions in the several detectors is performed by the **H**ERMES **D**e**C**oder (HDC). It not only calculates hit positions in every detector part separately but uses a general geometry file and alignment information to give each hit in each detector part (or plane) in coordinates of the HERMES coordinate system. After this first step in the HERMES data production chain the hit information is used by a tree search algorithm [Wan] to reconstruct tracks in the detector, this software is called HRC. The ADAMO tables produced by HRC contain several tracks, including the track momentum and charge, calculated by the bending in the magnet between the front and the back partial track.

The aforementioned SLOW data is then synchronized with the HRC tables by the μDST-writer and stored in the so-called μDST tables. These tables contain the full physics information necessary to perform data analysis at the advantage of reducing the amount of storage space and increasing analysis code performance. The complete data of the 2002 running contains roughly 5000 runs with approx. 450 MB each while the compressed μDST data needs only 7 GB of disk space.
For Monte Carlo Data a very similar production chain is applied. Instead of the DAQ and HDC a generator of DIS events, GMC based on LEPTO[IER97] and JETSET[Sjo95] is used. The simulation of the detector responses and its material is performed by HMC, containing a GEANT3 [BBM$^+$] implementation of all detector components. The Monte Carlo data gets reconstructed and compressed with HRC and the μDST-writer just like real data, although some tables for the generated values are added. It is schematically displayed in Fig. 4.6.

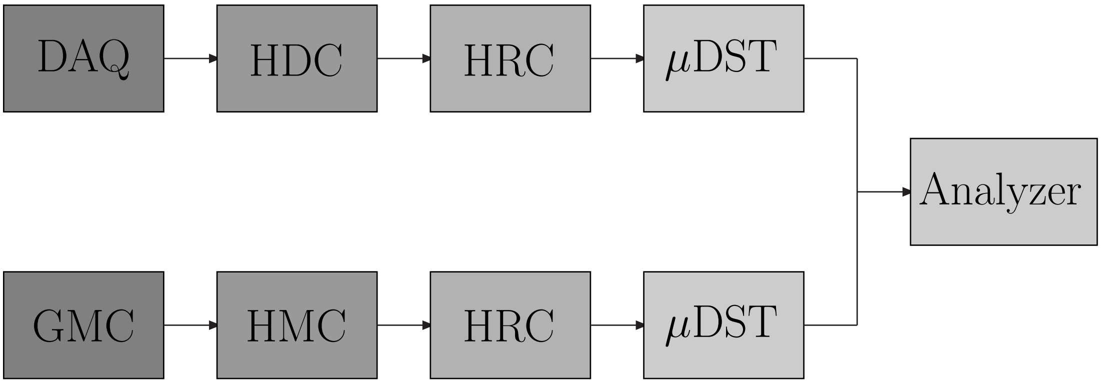

Figure 4.6: The HERMES data production chain for detector data in the top row and for Monte Carlo data in the bottom row of the chain.

A further explanation of the software applied at HERMES in much more detail can be found in [Fun].

4.4.3 Quality monitoring

HERMES checks the quality of the data already in the process of data-taking. One essential component of this online-quality monitoring is the so called wiremaps program originally created to check the responses of each wire in the drift chambers but nowadays adapted to almost all detector components in order to see dead wires, photomultipliers, silicon strips and other detector responses. One can immediately see during data-taking, if one detector component has some serious problems. As an example a dead wire would be visible in one dead or low channel in a histogram over all wires in a detector plane while a broken TDC

card would result in a whole dead region in the same histogram.
Additionally, also physics quantities are monitored during data taking showing for example the average lepton and hadron multiplicities for each run, the vertex positions and some preliminary PID values compared to the direct PID detector responses. If some problems occur, the corresponding runs can be marked as bad in the logrun file which contains the information about the target gas, polarized or unpolarized running, the analyzability and space for comments such as detector trips.
During the data production the information from the logrun file as well as the tables containing the detector responses and the slow information are distilled into a 32-bit pattern created per burst and detector half containing all the conditions under which this burst has been taken. For an analysis most of the bits should not be set, although depending on the purpose of the analysis some bad bits can be set. The following relevant bits are set, if

bit 2: the trigger 21 dead time has unphysical values,

bit 6: this is the first burst of a run,

bit 7: this is a record, which is part of the last burst in a fill with reconstructed events, or a record, which is bad due to e.g. synchronization problems, burst or event number jumps or table overflows,

bit 8: there is no particle identification (PID) available due to initialization problems or an unknown calorimeter threshold,

bit 11: the target is unpolarized,

bit 12: the log-book information is not available,

bit 13: the target is in the three state mode,

bit 14: the target is in the special two state mode for polarized Bhabha scattering,

bit 15: the target is unpolarized according to the valve settings of the target,

bit 16: the target is in a bad state,

bit 17: there are dead blocks in the calorimeter,

bit 18: there are dead blocks in the hodoscope H2 and in the luminosity monitor,

bit 19: the TRD is in a bad state,

bit 20: planes have tripped in the FC's or BC's,

bit 21: for the period, in which the RICH was operated with N_2,

bit 22: the RICH has trips,

bit 25: the RICH is in a bad state,

bit 31: there is more than one dead block in the calorimeter (except outer blocks),

whereas the remaining relevant bits are not set, only if

bit 0: the target is in a spin state up or down with respect to the HERMES coordinate system,

bit 3: the burst length is between 0 and 11 seconds,

bit 4: the beam current is between 2 and 50 mA,

bit 5: the luminosity monitor count rate is between 1 and 80 Hz,

bit 9: the data is analyzable according to the log-book,

bit 10: the target is in the two state mode,

bit 30: the sanity check on the artificial dead time correction was successful. This artificial dead time correction is not used anymore since the year 1998. This bit should not discard any burst.

For the productions before 2002 the bits **23**, **24**, and **27** are used to check the measured quantities for the target polarization calculation. Since a fixed target polarization for the whole production is given by the target group, these checks are not necessary anymore and the three bits are always empty now. The lower limits for the beam current and the luminosity rate are reduced, due to smaller HERA currents in the year 2002 and a smaller acceptance of the luminosity monitor with a transverse target magnet field. A detailed study of the calorimeter dead blocks [Has02] has shown, that for charged tracks in semi-inclusive analysis one dead block does not influence the resulting asymmetries. Therefore bit **31** is used for charged particles and bit **17** is used for π^0. The bits **1** and **28** are used for the beam polarization and are not considered in this analysis.

4.5 HERA performance and data taking

As can be seen in Fig. 4.7 which displays the integrated amount of DIS events versus the day of data taking, it took quite a while to take a reasonable amount of data in the running period of 2002, ranging from fall 2002 to late spring 2003. This is mostly due to the fact that the collider experiments H1 and ZEUS suffered from unexpectedly high synchrotron and other background rates in detector components closest to the beam pipe and the interaction region. This forced the machine group to run with lower beam currents, for the positron beam they stayed below 30 mA resulting in low event rates at HERMES. Additionally also several problems occurred running the accelerator resulting in several periods with hardly any *Luminosity run* conditions. In fall 2003 and spring 2004 the data taking worked quite reliably, as now the HERA II accelerator seems to be understood and also measures were taken to reduce the background rates in the collider experiments. Therefore the beam currents could be raised and also the availability of the beam for the experiments increased. Currently HERMES has taken the following amount of transversely polarized raw DIS events before data qualitiy.

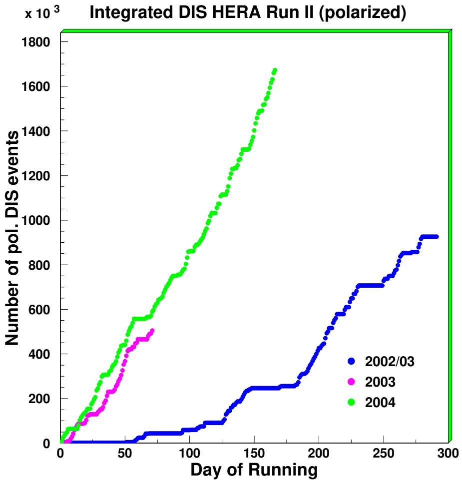

Figure 4.7: Integrated transversely polarized DIS events vs. the number of days of data taking.

production year	# DIS events
2002	920K
2003	500K
2004	1.7M

On clearly sees that once the new data is calibrated and run through the production chain the statistical errors will decrease significantly.

5

Single spin asymmetries

5.1 Definition of angles

Two different azimuthal angles play a role in the cross section containing either the Sivers function (equation 3.21) or transversity (equation 3.19). Those angles are defined between the lepton scattering plane and either the transverse momentum of the outgoing hadron or the transverse polarization vector of the target as illustrated in figure 5.1. The azimuthal

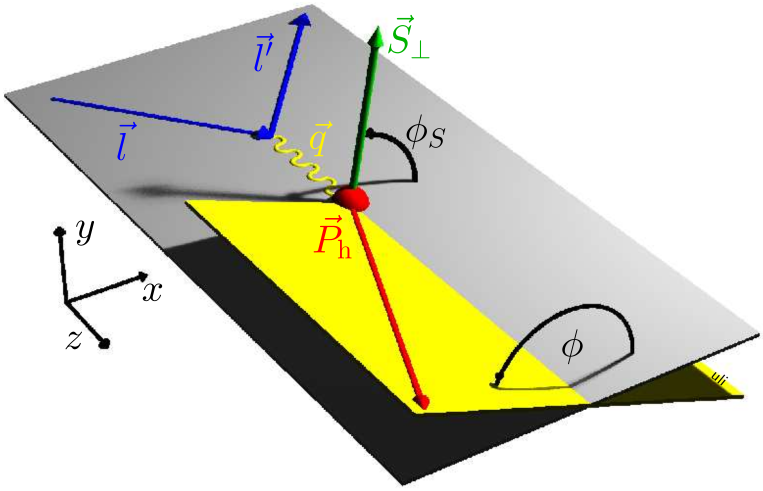

Figure 5.1: Kinematics of the process $lH \to l'hX$ in the lab frame.

angle of the target spin can be calculated as

$$\phi_S = \frac{\mathbf{q} \times \mathbf{l} \cdot \mathbf{S}}{|\mathbf{q} \times \mathbf{l} \cdot \mathbf{S}|} \cdot \arccos\left(\frac{\mathbf{q} \times \mathbf{l} \cdot \mathbf{q} \times \mathbf{S}}{|\mathbf{q} \times \mathbf{l}| \cdot |\mathbf{q} \times \mathbf{S}|}\right) \quad , \tag{5.1}$$

where $\mathbf{q}$ is the 3-vector of the virtual photon, $\mathbf{l}$ is the 3-vector of the incoming lepton and $\mathbf{S}$ is the polarization vector of the target nucleon, all of them evaluated in the laboratory frame.

According to the conventions used by the HERMES target group [LRT03], the positive target state P_z^+ is defined as $(0, -1, 0)$ using the HERMES coordinate system, defined in chapter 4; here the target nucleons are polarized parallel to the transverse magnetic holding field of the target. As can already be seen from this definition of the angle ϕ_S this angle would be shifted by π if the polarization vector were in the opposite direction . The resulting asymmetries would then only change their sign but would not interchange Sivers and Collins effects. When $\mathbf{S} \rightarrow -\mathbf{S}$ then $\arccos\left(\frac{\mathbf{q}\times\mathbf{l}\cdot\mathbf{q}\times\mathbf{S}}{|\mathbf{q}\times\mathbf{l}|\cdot|\mathbf{q}\times\mathbf{S}|}\right) \rightarrow \pi - \arccos\left(\frac{\mathbf{q}\times\mathbf{l}\cdot\mathbf{q}\times\mathbf{S}}{|\mathbf{q}\times\mathbf{l}|\cdot|\mathbf{q}\times\mathbf{S}|}\right)$ and $\frac{\mathbf{q}\times\mathbf{l}\cdot\mathbf{S}}{|\mathbf{q}\times\mathbf{l}\cdot\mathbf{S}|} \rightarrow -\frac{\mathbf{q}\times\mathbf{l}\cdot\mathbf{S}}{|\mathbf{q}\times\mathbf{l}\cdot\mathbf{S}|}$, thus $\phi_S \rightarrow -(\pi - \phi_S) = \phi_S - \pi$. Therefore all asymmetries involving an uneven multiple of ϕ_S will change their sign.

Analogous the azimuthal angle of the outgoing hadron is defined as

$$\phi = \frac{\mathbf{q} \times \mathbf{l} \cdot \mathbf{P_h}}{|\mathbf{q} \times \mathbf{l} \cdot \mathbf{P_h}|} \cdot \arccos\left(\frac{\mathbf{q} \times \mathbf{l} \cdot \mathbf{q} \times \mathbf{P_h}}{|\mathbf{q} \times \mathbf{l}| \cdot |\mathbf{q} \times \mathbf{P_h}|}\right) \quad , \tag{5.2}$$

where $\mathbf{P_h}$ is the 3-vector of the outgoing hadron in the lab frame.

These definitions are the same as the ones used in the HERMES single spin asymmetries on a longitudinally polarized proton [A$^+$00, A$^+$01b] or deuterium target [A$^+$03b]. They therefore differ from the conventions used by Mulders et al. [MT96] by a sign.

For longitudinally polarized nucleons there occurs only a small transverse component $|S_T|$ of the target polarization with respect to the virtual photon γ direction. This component is proportional to $\sin\theta_\gamma$, with θ_γ being the angle between the incoming lepton and the virtual photon, which in the HERMES measurements in the years 96-00 typically was around 15%. Hence the leading twist terms related to the transversity distribution or the Sivers function were always suppressed. They could thus be of the same order of magnitude as the twist-3 terms occurring in the cross section expression for the longitudinal component of the target $|S_L|$ (see equation 3.23). For HERMES kinematics $|S_L| \propto \cos\theta_\gamma \approx 0.98$. As the target polarization was (anti)parallel to the incoming lepton beam the target polarization vector was always oriented in the lepton scattering plane, thus the azimuthal angle of the target spin ϕ_S was confined to the values 0 or π. The Collins and Sivers effects could both contribute to the remaining $\sin\phi$ moment of the asymmetry, and were not distinguishable since

$$\sin(\phi + \phi_S) = \sin(\phi + \pi) = \sin(\phi - \pi) = \sin(\phi - \phi_S) \quad . \tag{5.3}$$

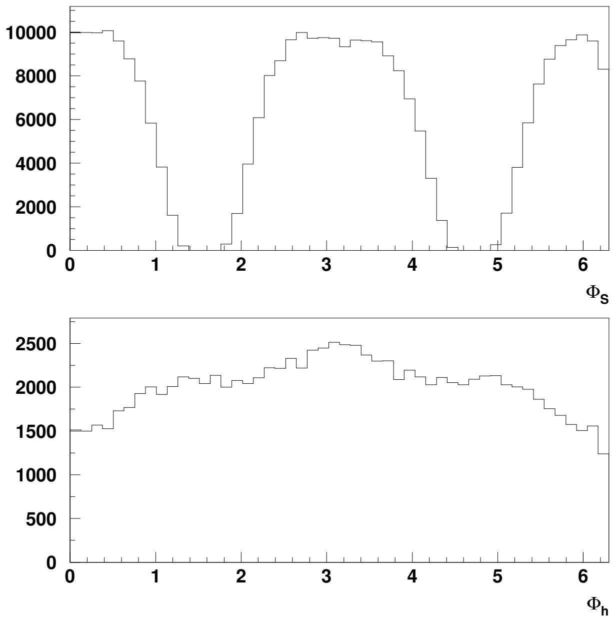

Figure 5.2: Top: distribution of the azimuthal angle ϕ_S in arbitrary units as calculated for DIS leptons in the data sample from 2002. Bottom: distribution of the azimuthal angle ϕ in arbitrary units as calculated for all hadrons from the 2002 data sample.

With a transversely polarized target the azimuthal angle of the target polarization ϕ_S can take any value in the interval $[0, 2\pi]$ although it is affected by the acceptance of the HERMES spectrometer. It cannot detect leptons for ϕ_S near $\pm\frac{\pi}{2}$ because this angular range corresponds to the gap between top and bottom part of the detector (the target polarization vector always points in the y-direction) as illustrated in Fig. 5.2. The twist-3 terms associated with the component of the target spin vector longitudinal to the virtual photon momentum are now not only suppressed by $1/Q$ but also kinematically suppressed by a factor proportional to $\sin\theta_\gamma \propto 15\%$.

Thus it is now easier to interpret the measured asymmetries (in a theoretical framework). It is possible to distinguish between Sivers and Collins moments as now two independent variables, ϕ and ϕ_S, are available. Two different, orthogonal combinations give access to either the Sivers asymmetry or the Collins asymmetry. To see that for example a non-vanishing Sivers moment $\propto \sin(\phi - \phi_S)$ does not give a contribution to the Collins moment assuming no acceptance effects, perfect resolution in the azimuthal angles and enough statistics, the integral over $(\phi + \phi_S)$ containing the weighting function $\sin(\phi + \phi_S)$, the Sivers moment and the integral over the remaining angle ϕ_S should vanish:

$$\begin{aligned}
& \int d\phi_S \int d(\phi+\phi_S) \cdot \sin(\phi+\phi_S) \cdot \sin(\phi-\phi_S) \\
= & \int d\phi_S \int d\phi' \cdot \sin\phi' \cdot \sin(\phi' - 2\phi_S) \\
= & \int d\phi_S \int d\phi' \cdot \sin\phi' \cdot [\sin\phi' \cdot \cos 2\phi_S - \cos\phi' \cdot \sin 2\phi_S] \\
= & \int d\phi_S \int d\phi' \cdot \sin\phi' \cdot \sin\phi' \cdot \cos 2\phi_S \\
= & \pi \cdot \int d\phi_S \cos 2\phi_S \\
= & 0 \quad .
\end{aligned} \tag{5.4}$$

One question which comes up frequently is about the definition of the asymmetries. As the HERMES spectrometer is not a 4π detector it is generally preferable to look at asymmetries to minimize the effects of the acceptance but also to eliminate unpolarized cross section contributions. For simplicity one can assume a cross section which contains an unpolarized term $\sigma_{UU}(x,y,Q^2)$ and a polarized term proportional to $\sigma_{UT}(x,y,Q^2)\sin(\phi+\phi_S)$ (the argument goes similar when also allowing a $\sin(\phi-\phi_S)$ term). The azimuthal angle ϕ_S is always defined as the angle between the lepton scattering plane and the target spin vector in one spin state. The state in which the spin of the nucleon is parallel to the **B**-field is denoted as the '+ state', whereas the other state is denoted as the '− state'. Then the azimuthal angle between the lepton scattering plane and the target spin vector of the '− state' is shifted by π from the calculated (i.e. measured) angle, i.e. $\phi'_S = \phi_S + \pi$. Calculating the cross section asymmetry, which is just the count rate asymmetry without weighting with any harmonics, for a certain ϕ_S yields:

$$\begin{aligned}
A_{UT}(\phi,\phi_S) &= \frac{\sigma^+ - \sigma^-}{\sigma^+ + \sigma^-} \\
&= \frac{\sigma_{UU} + \sigma_{UT}\cdot\sin(\phi+\phi_S) - (\sigma_{UU} + \sigma_{UT}\cdot\sin(\phi+\phi'_S))}{\sigma_{UU} + \sigma_{UT}\cdot\sin(\phi+\phi_S) + (\sigma_{UU} + \sigma_{UT}\cdot\sin(\phi+\phi'_S))} \\
&= \frac{\sigma_{UU} + \sigma_{UT}\cdot\sin(\phi+\phi_S) - (\sigma_{UU} + \sigma_{UT}\cdot\sin(\phi+\phi_S+\pi))}{\sigma_{UU} + \sigma_{UT}\cdot\sin(\phi+\phi_S) + (\sigma_{UU} + \sigma_{UT}\cdot\sin(\phi+\phi_S+\pi))} \\
&= \frac{\sigma_{UU} + \sigma_{UT}\cdot\sin(\phi+\phi_S) - (\sigma_{UU} - \sigma_{UT}\cdot\sin(\phi+\phi_S))}{\sigma_{UU} + \sigma_{UT}\cdot\sin(\phi+\phi_S) + (\sigma_{UU} - \sigma_{UT}\cdot\sin(\phi+\phi_S))} \\
&= \frac{\sigma_{UT}\cdot\sin(\phi+\phi_S) + \sigma_{UT}\cdot\sin(\phi+\phi_S)}{\sigma_{UU} + \sigma_{UU}} \\
&= \frac{\sigma_{UT}\cdot\sin(\phi+\phi_S)}{\sigma_{UU}} \quad .
\end{aligned} \tag{5.5}$$

In this way one filters out the transverse cross section components of interest. The cross-section asymmetry can be fitted with the according trigonometric functions (i.e. $\sin(\phi+\phi_S)$ in the previous example).

It can be shown with similar arguments that this projection of the transverse cross section works also for the moments method of the asymmetry calculation:

$$\begin{aligned} A_{UT}^{\sin(\phi\pm\phi_S)} &= 2\cdot\frac{\sum_i^{N^+}\sin(\phi_i\pm\phi_{S,i})-\sum_i^{N^-}\sin(\phi_i\pm\phi_{S,i})}{N^+ + N^-} \\ &= 2\cdot\frac{1/2\sigma_{UT}+1/2\sigma_{UT}}{2\sigma_{UU}} \quad . \end{aligned} \tag{5.6}$$

Also note that the sign of the asymmetries does not change when defining the other target state as the '+ state' as long as one calculates ϕ_S then with respect to this spin orientation.

In this method the cross section will be first integrated (or in the experiment summed up) with the corresponding harmonics of the angles of each event as a weight. Thus the extra sign for the negative state also occurs for the polarization dependent part of the cross section. The factor 2 takes care of the fact that the integrals of $\int_0^{2\pi}\sin^2=\pi$ give 1/2 and hence once the transverse cross section in the numerator stands against twice the unpolarized cross section in the denominator, as the integration there yields 2π. Any additional factors of two originating from the definition of the (1) and (1/2) moments are only taken into account in chapter 6. They are explicitly discussed in appendix D. With this weighted method, higher moments in the cross section in conjunction with nonzero moments in the acceptance can result in an additional moment in the harmonic one is looking for, e.g.

$$\cos_{acc}\phi\cdot\sin_\sigma 2\phi=\frac{1}{2}\sin\phi+\frac{1}{2}\sin 3\phi \quad , \tag{5.7}$$

where the $\sin_\sigma 2\phi$ moment appears in the cross section and the $\cos_{acc}\phi$ moment is created by the acceptance. Thus when using this method one has to ensure a very good knowledge of the acceptance and possible contributions of higher harmonics in the cross section to correct for them. In an ideal 4π detector both methods are equivalent, while this has to be studied for a real detector such as the HERMES spectrometer.

5.2 Monte Carlo studies

In this section the effects of the detector acceptance and smearing of kinematical variables by multiple scattering and energy loss on the measured $\sin\phi$ and $\sin 2\phi$ moments is studied by using a Monte Carlo (MC) simulation. At the time of these studies no MC generator based on the distribution functions $h_1(x)$ and $f_{1T}^\perp(x,p_t)$ and the fragmentation function $H_1^\perp(z,k_t)$ at tree level (i.e. based on the leading Feynman diagrams) exists to create azimuthal asymmetries in SIDIS reactions. Therefore the unpolarized generator LEPTO [IER97], based on the fits to unpolarized distribution functions was used in conjunction with the LUND fragmentation model applied in the package JETSET [Sjo95] tuned to HERMES multiplicities [A$^+$01a, Hil]. The HERMES spectrometer is modeled in a GEANT3 [BBM$^+$] simulation.
An unpolarized MC data set for deuterium with the 2000 geometry and approximately 10 M DIS events as well approximately 10 M DIS events of unpolarized hydrogen data including the 2002 geometry and a parameterization of the transverse magnetic field were generated.

Since these events were generated in an unpolarized MC production one has to assign a spin state arbitrarily and re-weight the events to introduce a target-spin dependent azimuthal dependence.
Moments of different size and kinematic dependencies were introduced to the generated samples to extract detector effects on these azimuthal asymmetries possibly caused by the detector acceptance itself and the influence of the transverse target magnet and depending on different kinematic variables or linear combinations of the two azimuthal angles.

5.2.1 Method to generate moments

Assume a real particle yield which contains an unpolarized term ($\propto \sigma_{UU}(x, Q^2)$) and polarized terms ($\propto \sigma_{UT,i} f^i(\phi, \phi_s, x, Q^2)$), convoluted with an acceptance function ϵ which can also depend on the azimuthal angles and kinematics:

$$N(x, Q^2) = \left(\sigma_{UU} + \sigma_{UT,i} f^i(\phi, \phi_S)\right) \times \epsilon(\phi, \phi_S) \quad . \tag{5.8}$$

Thus by arbitrarily attributing unpolarized Monte Carlo runs to different polarization states (±) and re-weighting their events by a function similar to

$$1 \pm w_i(x_{gen}, z_{gen}) \cdot f^i(\phi_{gen}, \phi_{S,gen}) \tag{5.9}$$

the extracted cross section asymmetry

$$A_{UT}(\phi_{rec}, \phi_{S,rec}) = \frac{N^-(\phi_{rec}, \phi_{S,rec}) - N^+(\phi_{rec}, \phi_{S,rec})}{[N^-(\phi_{rec}, \phi_{S,rec}) + N^+(\phi_{rec}, \phi_{S,rec})]} \tag{5.10}$$

would ideally only contain the *polarization dependent* part $w_i(x_{gen}, z_{gen}) \cdot f^i(\phi_{h,gen}, \phi_{S,gen})$ of the weighting function and thus would only contain the ratio of the polarized part of the cross section over the unpolarized cross section as in read data. The Monte Carlo studies then have to show, that the assumption of a polarization and kinematics independent acceptance function is valid and that these generated moments can be reproduced.

Generated functions In order to test the best ϕ_S and ϕ binning and the best reconstruction method the MC-data samples were re-weighted by weighting moments in the generated angles. As an assumption two kinematical dependencies were taken for the generated moments. First $\sin(\phi + \phi_S)$ and/or $\sin(\phi - \phi_S)$ moments were independently generated as linear functions of the generated x:

$$1 \pm A \cdot x \cdot \sin(\phi + \phi_S) \pm B \cdot x \cdot \sin(\phi - \phi_S) \quad , \tag{5.11}$$

where A and B were taken to have values of $0.0, 0.2, 0.4$ and 0.8. This functional form resembles in a very simple way some theoretical predictions [MSY02a, MSY02b, EGS02b] favorising an increasing asymmetry with increasing x for at least the Collins type asymmetry

within the range of the HERMES acceptance.
The second function to generate moments applied for the 2-dimensional fit method is also slightly phenomenologically motivated, as its functional dependence is that of a very simple parameterization for distribution functions [BBS95]:

$$1 \pm C \cdot x(1-x)^D \cdot \sin(\phi + \phi_S) \pm E \cdot x(1-x)^F \cdot \sin(\phi - \phi_S) \quad , \tag{5.12}$$

which does not only guarantee a vanishing asymmetry for $x = 0$ but also for $x = 1$. Values C and E were taken as $0.0, 0.2$ and also 0.8. For the exponents D and F integer values between 0 and 3 were taken.

5.2.2 Asymmetry reconstruction methods

As two orthogonal linear combinations of the angles ϕ and ϕ_S are physically relevant, there are several different possibilities on how to extract the corresponding asymmetries. These combinations fall in either of the already mentioned ways and can be characterized as follows:

- **Weighted moments:** In this method the events are weighted with e.g. the sine of the relevant combinations of azimuthal angles (as in equation 5.6). It is most preferred by theorists as it directly implies the integration over the azimuthal angles. Although this is theoretically the cleanest integration of the angles and the $P_{h\perp}$ distribution of the hadrons and has been applied in previous analysis on single spin asymmetries it contains some flaws. From the experimentalists point of view it is unfortunately the method most affected by acceptance effects such as for example the large $\cos\phi$ moments stemming from the spectrometer acceptance which then can give false asymmetries in conjunction with higher moments in the cross section as described in equation 5.7. Recently it has been shown that the angular and tranverse momentum integrations work equally well using the following methods [BO03].

- **1-dimensional analysis:** Just like in the previous analysis on the single spin asymmetries of semi-inclusive pions and kaons from a longitudinally polarized deuterium target [A^+03b] the cross section asymmetry (cf. equation 5.10) is evaluated and fit in just a binning in the angular combinations of interest (i.e. $\phi := \phi \pm \phi_S$). By using this technique moments introduced by the acceptance cancel out. One might however be vulnerable to distortions due to the other angular moment(s) in the cross section as the ϕ resolution will not be perfect and statistics will limit the number of ϕ bins. Also polarization independent moments (as in equation 3.22) can give a contribution in the denominator and might in theory affect the fit results.

- **2-dimensional analysis:** Instead of displaying and fitting the two theoretically orthogonal combinations of angles (i.e.$\phi := \phi \pm \phi_S$) separately it is also possible to introduce an asymmetry in a $\phi \times \phi_s$ binning. Then this asymmetry can be fitted in a 2-dimensional way by several moments simultaneously. That means that one does not need to fit only the $\sin(\phi \pm \phi_S)$ moments but can fit the $\sin(3\phi \pm \phi_S)$ and higher twist terms at the same time. This method is displayed in Fig. 5.3 for a x-bin and a combination of Sivers and Collins moments generated. In principle this method should be more accurate with a limited angular resolution but as the number of events will be distributed into N^2 bins instead of only N bins in the 1-dimensional method it might need a larger amount of statistics to extract the asymmetries with the same precision. Also here polarization independent moments occurring in the denominator can affect the fit results just like in the 1-dimensional analysis. Acceptance effects will be small as they are supposed to cancel out as well.

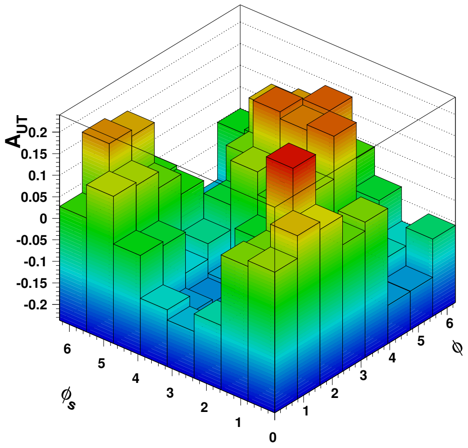

Figure 5.3: An example of a 2-dimensional asymmetry as calculated for the 2-dimensional binning method with 8 ϕ bins each. The asymmetry is calculated for 1 x-bin where a large Sivers and a relatively small Collins asymmetry were generated.

Results of the method comparison Several asymmetries of different magnitude, different type of moments and different dependencies on the kinematic variables were generated. Also the statistics was cut to roughly 1 M DIS as one systematic test. Below the results of the 3 methods will be compared. Generally it can already be seen in the description of the methods, that each method has its advantages and its disadvantages. These differences will be addressed and compared.

- **Weighted moments:** Figures 5.4 and 5.5 show reconstructed (data points) and generated (lines) moments which consist of either a Sivers or Collins type asymmetry linear in x or no asymmetry at all for π^+ and π^-. As higher order moments were not generated only direct acceptance effects such as those generated by a geometric acceptance in conjunction with the transverse magnetic field of the target can contribute. The upward (downward) pointing triangles show the moments for the up (down) state of the target separately. Those moments are defined as

$$A_{UT}^{\sin(\phi\pm\phi_S)\pm} = \frac{\sum_i^{N^\pm} \sin(\phi_i \pm \phi_{S,i})}{N^\pm} \quad . \tag{5.13}$$

Because of the transverse target magnetic field, whose effects will be discussed later, being independent of the target state residual moments of approximately 5% (-3%) are seen for π^+ (π^-) in the Collins channel and about 10% (-6%) in the Sivers channel. Nevertheless these fake moments cancel when taking the combined asymmetry consisting of both target states (squares).

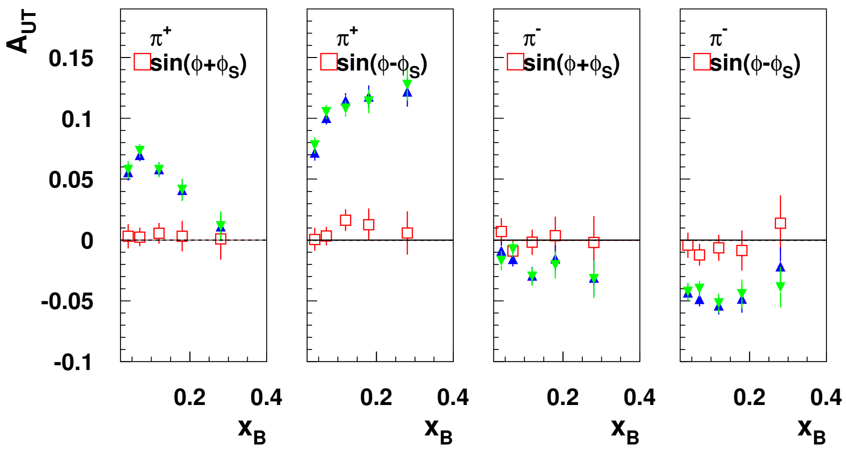

Figure 5.4: Weighted Collins and Sivers moments for π^+(left 2 plots) and π^-(right plots) in the up(down) target state are shown as up(down) triangles, the combined moments are represented by squares. No Sivers type moments and no Collins type moments were generated.

When introducing as well a Sivers as a Collins type moment with different magnitude effects of the higher moment will be large on the lower moment, as can be seen in Fig. 5.6, while the lower moment seems to add insignificantly to the extraction of the higher one. For a moment of equal or at least roughly the same magnitude this effect becomes smaller.

The Figures 5.7 for π^+(left plot) and for π^-(right plot) illustrate that the effect of the transverse target magnetic field vanishes when MC data generated without a transverse magnetic field is reconstructed. When switching on the transverse magnetic target field, residual asymmetries of up to the about 5% for π^+ and -4% for π^- appear, as shown in the left plots of Figs. 5.4. This effect seems to be larger for Sivers type asymmetries than for Collins type asymmetries. As mentioned before this moment reconstruction method might suffer from the combination of higher moments with acceptance effects. As a test a $\sin(2\phi)$ moment was generated which in conjunction with the $\cos\phi$ moment of the acceptance (see Fig. 5.2) results in an additional $\sin\phi$ moment. This is shown in Fig. 5.8 where the generated $\sin\phi$ moment of zero is not reproduced since the $\sin(2\phi) \propto 0.2x$ clearly creates a $\sin\phi$ moment. A similar, but smaller effect can also be observed in the $\sin(\phi \pm \phi_S)$ moments.

- **1-dimensional analysis:** As shown in the Figs. 5.9 this method also gives good agree-

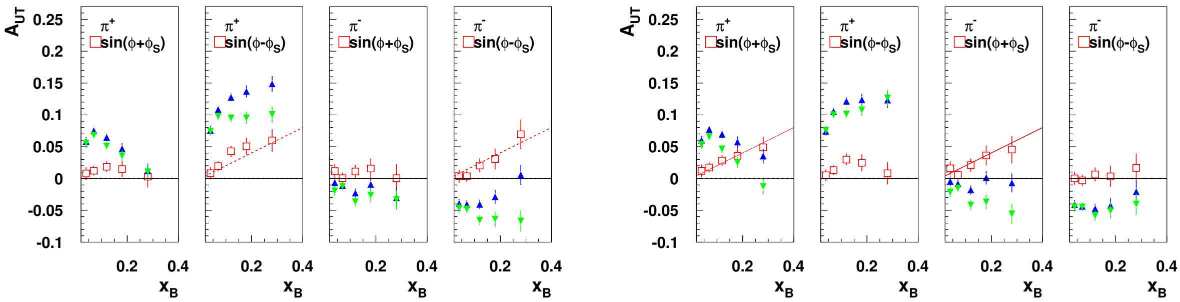

Figure 5.5: Weighted Collins and Sivers moments for π^+ (left plots) and π^-(right plots) in the up(down) target state are shown as up(down) triangles, the combined moments are represented by squares. Sivers type moments of $0.2 \cdot x$ (dashed line) and no Collins type moments (line) were generated in the left panel and vice versa in the right panel .

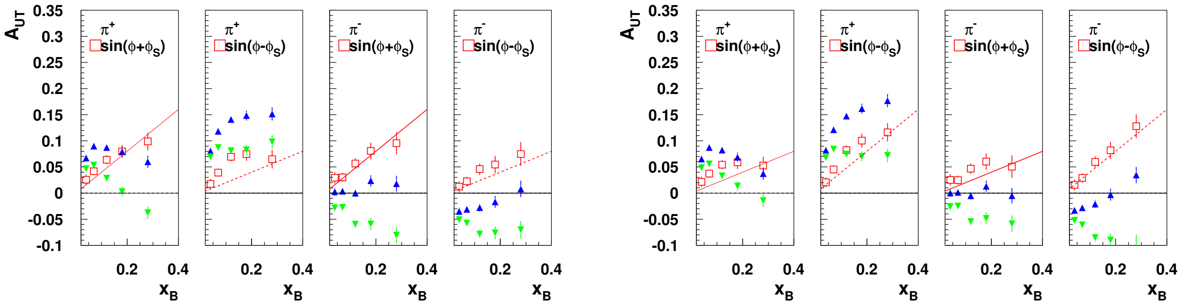

Figure 5.6: Weighted Collins and Sivers moments for π^+ (left plots) and π^-(right plots) in the up(down) target state are shown as up(down) triangles, the combined moments are represented by squares. Sivers type moments of $0.2{\cdot}x$ (dashed line) and Collins type moments of 0.4 (line) were generated in the left plots and vice versa in the right plots.

ment between generated and reconstructed moments, when both types of asymmetries have the same magnitude. In these plots the generated Sivers moment was exactly as large as the corresponding Collins moment; in the left plot of the figure both were $A^{\sin(\phi\pm\phi_S)}_{UT,gen} = 0.2 \cdot x$ for π^+ and in the right plot both were $A^{\sin(\phi\pm\phi_S)}_{UT,gen} = 0.2 \cdot x$ for π^-. The plots show also a comparison between 3 different ϕ binnings of $\{8, 12, 20\}$ bins. It can be seen, that the reconstructed $\sin(\phi \pm \phi_S)$ moments do not severely depend on the number of $\phi \pm \phi_S$ bins.

When 2 different moments were generated the higher moment is reconstructed well whether it is of Collins type or of Sivers type (Fig. 5.10). The lower moment is, however, severely affected by the large asymmetry generated in the other channel. As it seems this effect is largest at medium x-bins within the x-range of the analysis, the highest x-bin and the lowest x-bin are almost not affected.

Figure 5.11 shows that even when no moment is in the generated cross section, moments originating from the transverse magnetic target field in the denominator of these

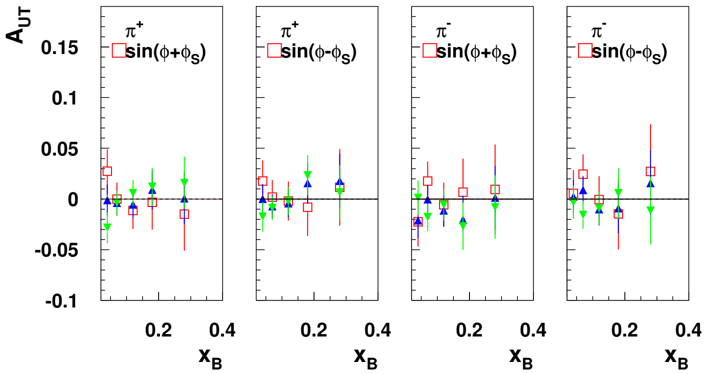

Figure 5.7: Weighted Collins and Sivers moments for π^+ (left plots) and π^- (right plots) in the up (down) target state are shown as up (down) triangles, the combined moments are represented by squares. No Moments were generated. Both plots were generated using the transverse target magnetic correction.

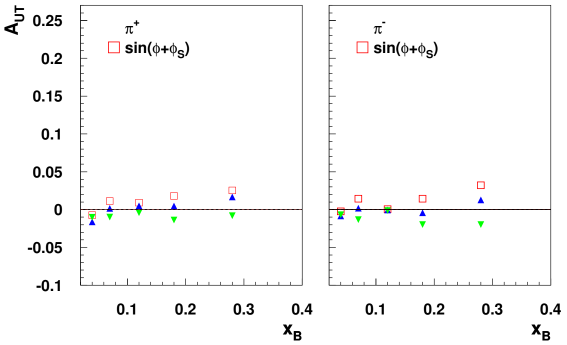

Figure 5.8: Extracted $\sin\phi$ moment when generating only a $\sin(2\phi) \cdot 0.2x$ moment.

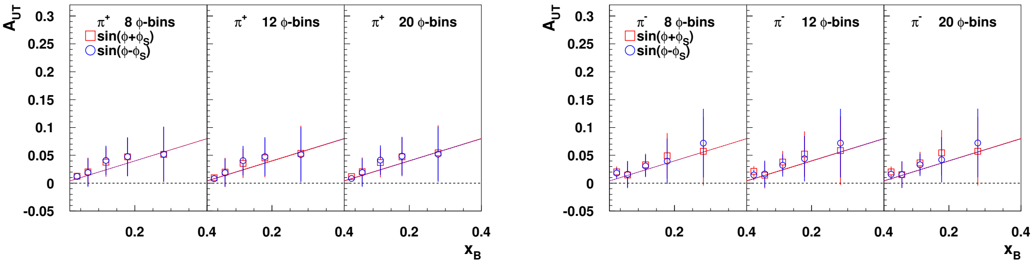

Figure 5.9: One-dimensional fit to reconstruct the generated Collins moment of $0.2 \cdot x$ (line) and Sivers moment of $0.2 \cdot x$ (line). The squares (circles) show the reconstructed values for Collins (Sivers) moments extracted for π^+ in the left panel and for π^- in the right panel.

asymmetries just give deviations less than 1% in the reconstructed values. This shows,

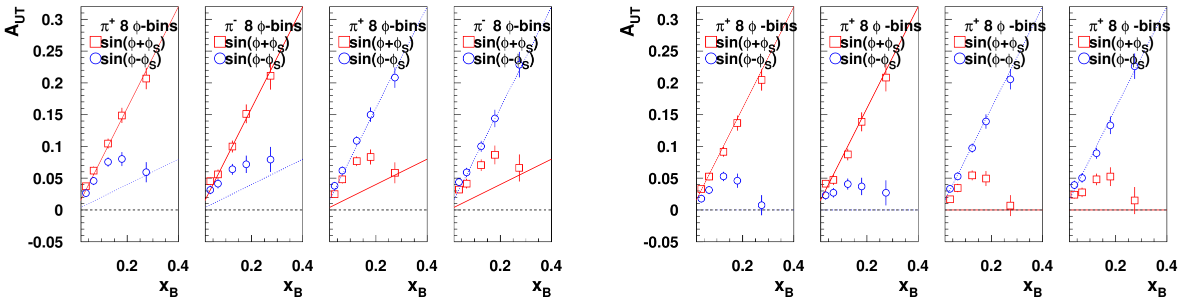

Figure 5.10: Left: One-dimensional fit to reconstruct the generated Collins moment of $0.8 \cdot x$ (line) and Sivers moment of $0.2 \cdot x$ (dotted line) for π^+ and π^- and vice versa, right: One-dimensional fit to reconstruct the generated Collins moment of $0.8 \cdot x$ (line) and Sivers moment of $0.0 \cdot x$ (dotted line) for π^+ and π^- and vice versa. The squares (circles) show the reconstructed values for Collins (Sivers).

that the unpolarized cross section cancels out in the numerator and a Taylor expanded denominator can only couple to higher moments. So the first harmonics containing a residual sine moment is a $\sin^2(\phi \pm \phi_S)$ moment which is linear in the polarized cross section and linear in the magnitude of the residual moment. When generating only one moment (either Sivers or Collins, constant in x) for several different values it is possible to give an estimate on the residual moment B_{res}:

$$\begin{aligned} A_{UT}(\phi = \phi \pm \phi_S) = & \\ &= \frac{\sigma_{UU}(1 + B_{res} \cdot \sin(\phi)) + B \cdot \sin(\phi) - (\sigma_{UU}(1 + B_{res} \cdot \sin(\phi))) - B \cdot \sin(\phi))}{\sigma_{UU}(1 + B_{res} \cdot \sin(\phi)) + B \cdot \sin(\phi) + (\sigma_{UU}(1 + B_{res} \cdot \sin(\phi)) - B \cdot \sin(\phi))} \\ &= \frac{B \cdot \sin(\phi)}{\sigma_{UU}(1 + B_{res} \cdot \sin(\phi))} \\ &\sim \frac{B \cdot \sin(\phi)}{\sigma_{UU}} \cdot \left(1 - B_{res} \cdot \sin(\phi) + \frac{1}{2} B_{res}^2 \cdot \sin^2(\phi) - \cdots \right) \\ &= \frac{1}{\sigma_{UU}} \cdot \left(B \cdot \sin(\phi) - B \cdot B_{res} \sin^2(\phi) + \frac{1}{2} B \cdot B_{res}^2 \sin^3(\phi) - \cdots \right) \quad . \end{aligned} \tag{5.14}$$

As it turns out B_{res} is of the same order of magnitude as the residual moments obtained by the weighted method.

- **2-dimensional analysis:** In this type of analysis not only single moments, but also combined moments, containing a Sivers type as well as a Collins type moment of different magnitude can be reconstructed fairly well. This has been tested for example in Fig. 5.12. Independent of the binning used the difference of the reconstructed from the generated moments is less than 0.5% and seems to be fluctuating only. Also binning effects cannot be observed.

Additionally in the case of this 2-dimensional fitting method also the second weighting

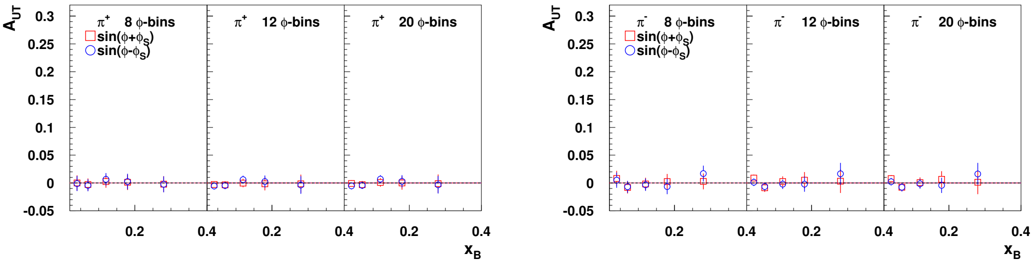

Figure 5.11: One-dimensional fit to reconstruct the generated Collins moment of $0.0 \cdot x$ and Sivers moment of $0.0 \cdot x$. The squares(circles) show the reconstructed values for the Collins(Sivers) type asymmetries for π^+ (left panel) and π^-(right panel).

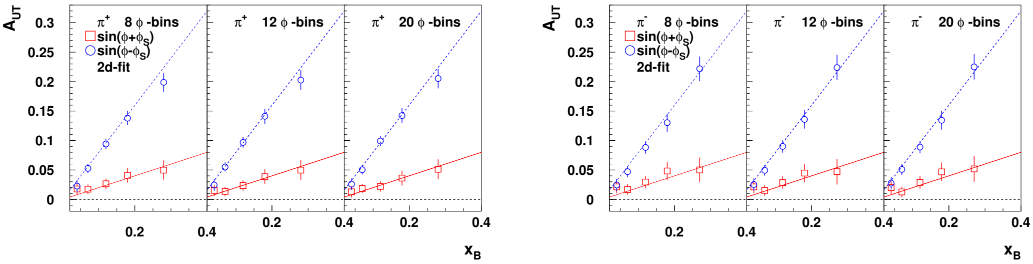

Figure 5.12: 2-dimensional fit to reconstruct the generated Collins moment of $0.2 \cdot x$ (line) and Sivers moment of $0.8 \cdot x$ (dotted line). The left plot shows π^+ the right plot π^-.

function (eq. 5.12) was used to generate asymmetries. Also here the results as shown in Fig. 5.13 verify, that the generated moments are reconstructed very well.

It still has to be shown, that this method also works reliable when the amount of statistics is low, since the actual amount of data taken in the years 2002/2003 with a transversely polarized target is only of the order of 0.75 million DIS events. To check whether the 2-dimensional method also works as good as before on low statistics a subsample of approximately 1M DIS MC events was taken out of the 10M generated. Of course the results fluctuate more than with the complete data set, but nevertheless the generated values still get reproduced quite well (Figs. 5.14).

As a conclusion the 2-dimensional fitting method is most reliable and will thus be applied in the data analysis as it shows the least deviations from the generated asymmetries. Since binning effects could not be observed, an 8×8 binning is used for the analysis.

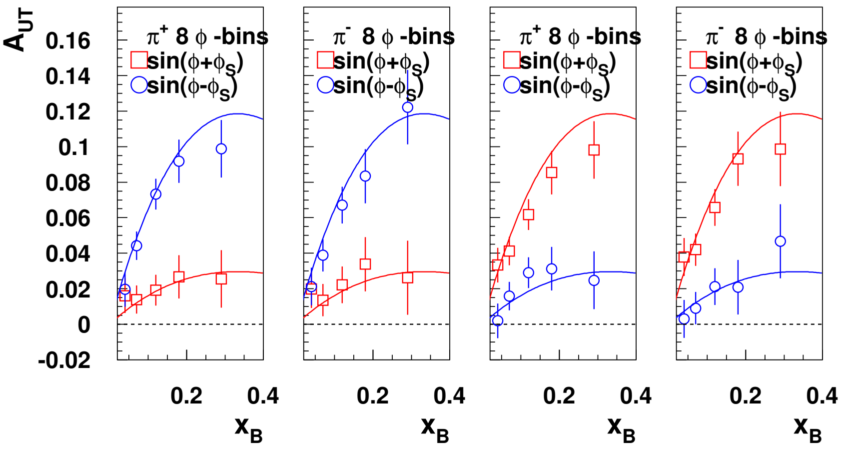

Figure 5.13: 2-dimensional fit to reconstruct the generated Collins moment of $0.2 \cdot x(1-x)^2$ (line) and Sivers moment of $0.8 \cdot x(1-x)^2$ (line) and vice versa. The left plot shows π^+ the right plot π^-.

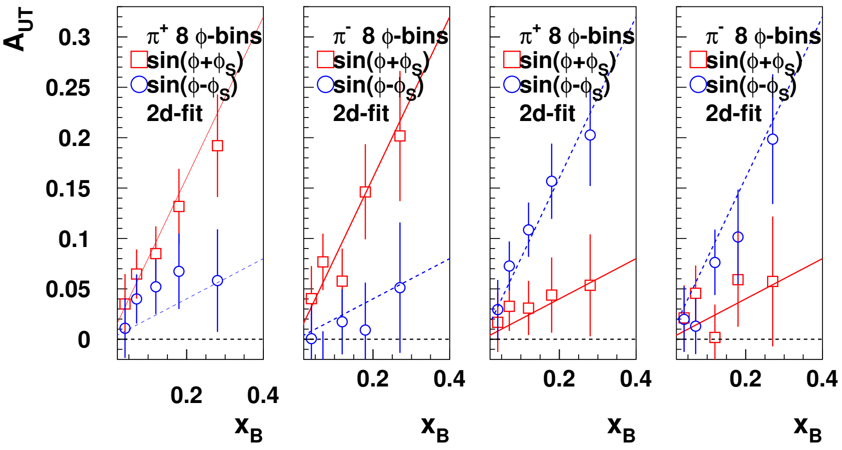

Figure 5.14: 2-dimensional fit to reconstruct the generated Collins moment of $0.8 \cdot x$ (line) and Sivers moment of $0.2 \cdot x$ (dashed line) and vice versa. The left plots show π^+ the right plots π^- asymmetries for a reduced MC data sample of approximately 1M DIS events.

5.2.3 Further asymmetry reconstruction studies

Unpolarized $\cos n\phi$ moments As recent theoretical predictions [GGO03a] favor a significant $\cos 2\phi$ moment in the unpolarized cross section and as the spectrometer acceptance can create $\cos n\phi$ moments as well, the denominator of the reconstructed asymmetries can also contain these two effects. The question arises if this can affect the reconstruction of the $\sin(\phi \pm \phi_s)$ moments, too. The unpolarized MC used does not contain a ϕ dependent cross section but it is known, that the spectrometer acceptance introduces a $\cos\phi$ moment which, although being there in all 3 reconstruction methods mentioned, does not alter the moments reconstructed. To demonstrate that even better a high $\cos\phi$ moment was introduced in the polarization independent weights. Figure 5.15 shows the reconstructed results using a generated $\cos\phi$ moment of 20% in comparison to the results without such a moment. No significant change can be seen. One can therefore conclude that unpolarized moments do not affect the asymmetry reconstruction of the polarized moments.

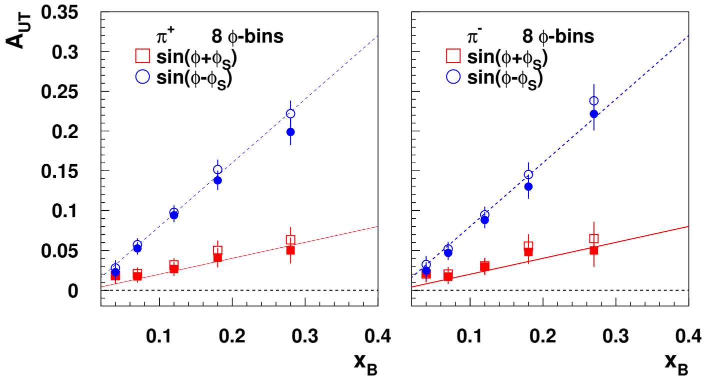

Figure 5.15: Comparison of the reconstructed moments for a generated Collins moments of $0.2 \cdot x$ and generated Sivers moment of $0.8 \cdot x$ with (open symbols) and without (closed symbols) an unpolarized cosine moment of 20%.

Radiative effects Unfortunately the MC generator does not specify if the radiative event one is looking at happened as initial or final state photon radiation. Without this information it is impossible to calculate the real lepton scattering plane, which could be very sensitive to radiative effects. Nevertheless most of the radiative photons produced are low energetic photons which move almost collinearly with the lepton and thus do not alter the lepton's direction. This in turn leaves the lepton scattering plane unchanged. It is known that such radiative events could also produce a $\cos\phi$ moment. Therefore the possibility of effects on the reconstructed asymmetries by radiative effects has been tested to some extent already in the previous paragraph by artificially introducing such a moment. As seen there, even large moments do not influence the moment reconstruction.

Another 2-dimensional fit It was also proposed to test if binning the asymmetries in a 2-dimensional binning in the angles $(\phi + \phi_S)$ and $(\phi - \phi_S)$ gives a different result than binning in ϕ and ϕ_S. It can be seen in Fig. 5.16 that there are no differences at the high statistics available in the MC sample. In the data small differences could be observed but they vanish when the statistical precision gets better.

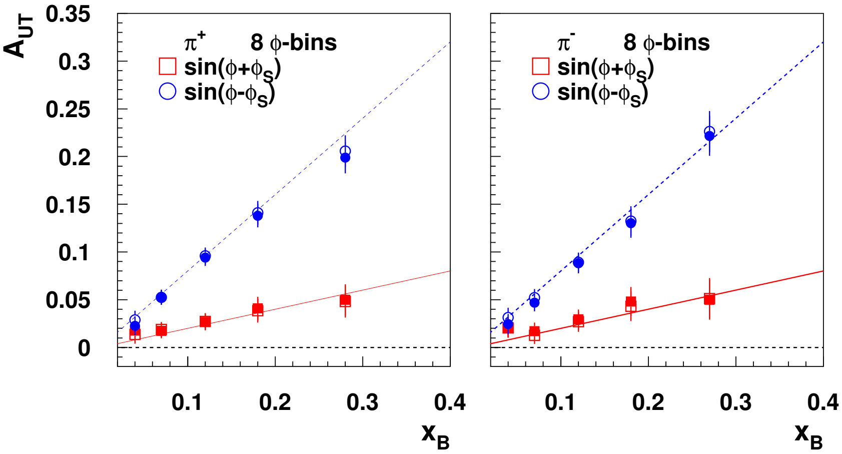

Figure 5.16: Comparison of the reconstructed moments for generated Collins moments of $0.8 \cdot x$ and generated Sivers moment of $0.2 \cdot x$ with the 2^{nd} way to fit 2-dimensionally (open symbols) to the standard method (closed symbols).

5.2.4 Resolution changes by the transverse target magnet field

As the effect of the transverse magnet is momentum dependent, the resolution of the kinematic variables $x, y, \theta_\gamma, \phi_e, \theta_e, E', z, P_{h\perp}, E_h, \phi_h, \theta_h, \theta_{\gamma h}, \phi, \phi_S, (\phi+\phi_S)$ and $(\phi-\phi_S)$ was evaluated in 1 GeV bins of the reconstructed hadron energy, where the subscript e denotes lepton variables and h hadron variables. All azimuthal angular resolutions were plotted modulus 2π to extract the real resolutions. Both, the absolute (eg. $\Delta\phi = \phi_{rec} - \phi_{gen}$) and the relative resolutions (eg. $\frac{\Delta\phi}{\phi_{gen}}$) were first fitted by Gaussian distributions in the interval of $[-0.2, 0.2]$, but due to the non-Gaussian nature of some of the resolutions (e.g. a double peak in the ϕ resolutions with transverse magnetic field) the mean value and the root mean square of the histograms were taken as a better measure for the variations.

As an example the angular resolution distributions for charged pions in the energy range $2 < E_h < 3$ GeV are shown as well for the transverse magnet case in Fig. 5.17 as for the case with no transverse magnet field. A clear increase in the width of the distributions can qualitatively be seen in the comparison of these 2 plots. Since the deflection of the charged particles is highest at low momenta, the hadron energy range between $2 < E_h < 3$ GeV, 2 GeV being the low hadron momentum cut, gives the largest change of resolutions. All absolute resolutions are summarized in table E.1 for π^+ and in table E.2 for π^-. As can be

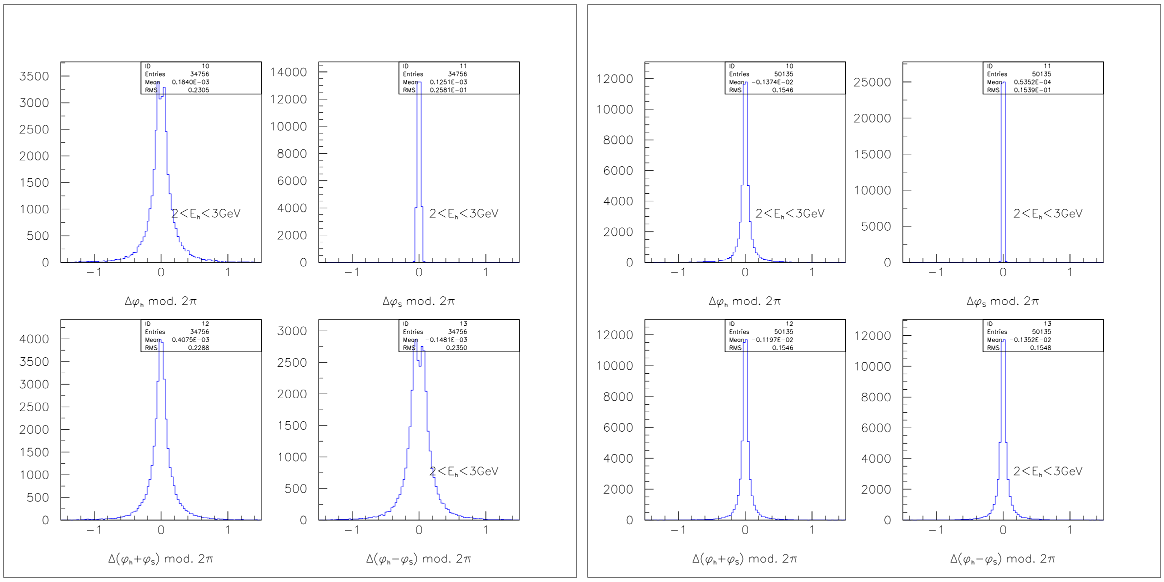

Figure 5.17: Angular resolutions $\Delta\phi$, $\Delta\phi_S$, $\Delta(\phi+\phi_S)$, $\Delta(\phi-\phi_S)$ for charged pions and kaons with transverse magnet on (left panel) and without the transverse magnet(right panel).

seen, the resolution does not severely change by the magnetic field in variables which only depended on the momentum of the track. Those include E_e,E_h,y and z. The variables which depend on the lepton or hadron track momentum as well as their angles show obviously generally worse resolutions with than without the transverse magnet. The resolution difference by the transverse magnet is largest for variables which depend on the momenta and angles of both the lepton and the hadron track. Therefore the azimuthal hadron angle ϕ and the transverse hadron momentum $P_{h\perp}$ are affected most. For negative hadrons the effect on ϕ is smaller than for positive hadrons which can be explained by deflection of the positron and the hadron in the same sense. Both particles get bend in opposite directions and thus having smaller impact on the calculation of the angle between scattering plane and hadron. While the azimuthal angular resolutions of the combined angles $\phi \pm \phi_S$ are mostly governed by the bad resolution of ϕ compared to ϕ_S, it is also visible from the resolution plots (cf. 5.18) that the difference of these 2 angles shows a worse resolution effect to the generated angles than for the sum of the angles.

The overall effect of the bending of the tracks due to the transverse magnet is around a few %. This means that generally the resolutions do only change by a comparatively small amount and that thus the cuts used for the old analyses [A$^+$01b, A$^+$00, A$^+$03b] can still be applied for data taken with a transverse magnetic field. Only the low transverse momentum cut $P_{h\perp} > 0.05$ GeV to define the azimuthal hadron angle should be replaced by the more direct cut in the hadron opening angle with respect to the virtual photon: $\theta_{\gamma,h} > 0.02\ rad$ which is several $mrad$ above its resolution and ensures no miscalculation of ϕ by a factor of π.

Target magnet correction Even though the resolutions do not drastically change it is possible to regain the original resolutions by correcting the tracks for the influence of the transverse target magnet.

When comparing the resolutions for different Monte Carlo data sets containing either the uncorrected values without the transverse magnet implemented, or the uncorrected values with the transverse magnet implemented or the corrected values one can see that most of the effects due to the transverse target magnet get corrected well by the track correction code, also known as TMC which was explained in detail in chapter 4.

Both correction methods agree very well in their calculation of the original angles and z-vertex positions, therefore the comparison plots Figs. 5.18, F.1 and F.2 contain only method 2 as an example. The plots show, that the resolutions without a transverse magnet field are almost recovered.

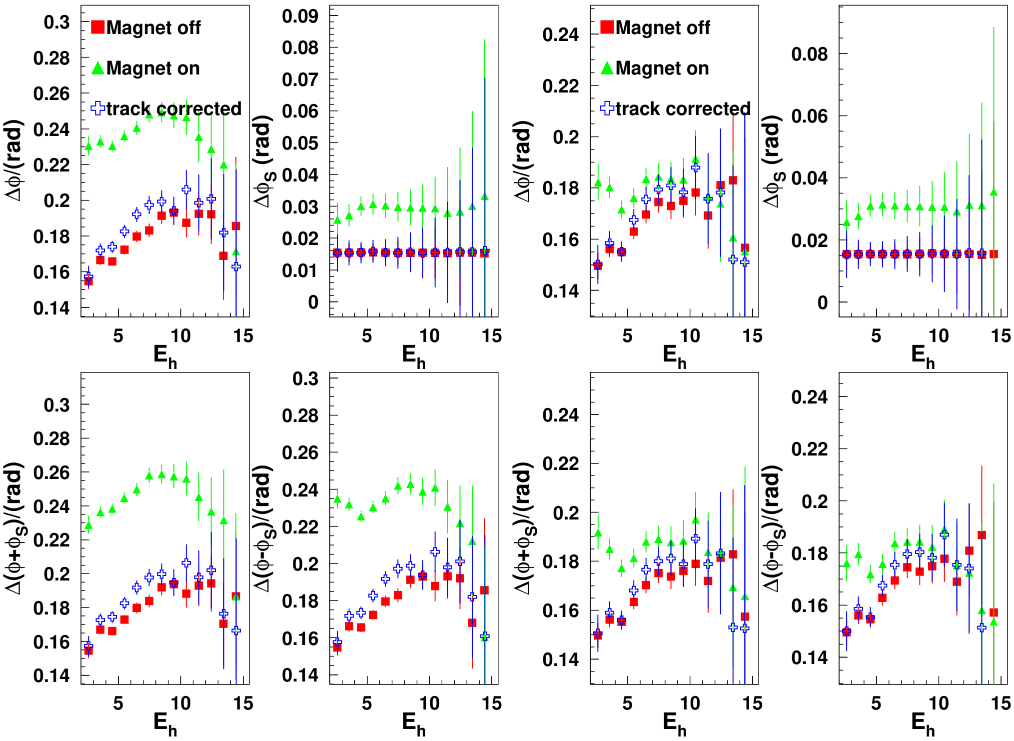

Figure 5.18: Comparison of angular resolutions vs. hadron energy for π^+ in in the left panel and π^- in the right panel.

5.2.5 Misalignment of the detector

In the analysis of the 1996-2000 data the following misalignment parameters of the top and bottom detector halves were found [BK03]:

	top	bottom
x-slope	+0.44 mrad	+0.24 mrad
y-slope	–1.20 mrad	+0.02 mrad
x-offset	–0.09 cm	–0.11 cm
y-offset	–0.01 cm	+0.11 cm

Particularly the top y-slope seems to be quite large. Such a slope should be measurable in a 7 m long detector during the annual surveys. However, at least the calorimeter does not show such a large offset. But these parameters do not have to come from real tilts or shifts of the detector alone, also the *force bridging* in the tracking, that is requiring a front and a back partial track to connect to each other in the magnet volume, could introduce a misalignment depending on the particle type, energy, and other quantities. Studies performed by the tracking experts have shown such a behavior of the misalignment parameters [BK03]. The large values of the parameters listed in the above table are upper limits, nevertheless, and were used in a modified geometry file for a Monte Carlo production where both the HMC and HRC use the misaligned detector geometry. Unfortunately due to a bug this MC production has to be rerun and could therefore not be used in this analysis. Nevertheless a few tests with an aligned MC production have been performed earlier, introducing the slopes mentioned directly in the analysis code. This procedure therefore moves all the track angles and thus also the azimuthal angles involved. The x and y offsets could of course not be probed by this procedure. No systematic shift of the extracted asymmetries due to the misalignment is visible.
In addition also the possibility of a slightly inclined magnetic target field has been tested. Such an inclination would result in a target spin which is not any more pointing in the $(0, -1, 0)$ direction but turned. As an assumption a turn around the z-axis of up to 3 degrees has been implemented in the MC reconstruction. No visible effect on the reconstructed asymmetries could be seen.

Additional MC studies can be found in [ESS] which are not presented here due to lack of space.

5.3 Data analysis

In this section the actual data analysis will be presented. After the description and motivation of the cuts on the data several systematic studies on the data are performed.

5.3.1 Data sample

For the present analysis the transversely polarized hydrogen data is used. This data was taken with an unpolarized beam during the fall of 2002 and the winter (up to February) of 2003. The 02c0 production which includes tracking corrections for the transverse target magnet was used for this analysis. Studies have been done also for uncorrected tracks for comparison.

5.3.2 Event Selection

In every good burst only events caused by Trigger 21, which is the lepton trigger, are taken into account. The leading leptons of these events are identified using the PID values

$$\mathrm{PID}_3 + \mathrm{PID}_5 > 1$$

for all runs starting at run 809. The runs before were not taken into account since no hadron identification was available. The leptons have to fulfill the following requirements:

$$-18 \text{ cm} \leq z_{\text{vertex}} \leq 18 \text{ cm} \tag{5.15}$$

which ensure, that the vertex position of the lepton track lies within the target cell region.

$$|x_{\text{calo}}| < 175 \text{ cm} \quad , \tag{5.16}$$
$$30 \text{ cm} < |y_{\text{calo}}| < 108 \text{ cm} \quad , \tag{5.17}$$

require that the whole electromagnetic shower is contained within the calorimeter. Therefore the inner and outer rows of the calorimeter were discarded. Additional fiducial volume cuts were applied for the entrance window to the spectrometer and the spectrometer magnet. The cuts on the kinematical variables

$$0.1 \leq y < 0.85 \quad , \tag{5.18}$$
$$0.023 < x < 0.4 \tag{5.19}$$

are basically limitations to the kinematical acceptance of the detector. The requirements

$$W^2 > 10 \text{ GeV}^2 \quad , \tag{5.20}$$
$$Q^2 > 1 \text{ GeV}^2 \tag{5.21}$$

ensure that the invariant mass of the photon nucleon system is above the conditions of the resonance region and that perturbative QCD can be applied. Furthermore

$$\text{leptoncharge} = \text{beam charge} \tag{5.22}$$
$$E' > 3.5 \text{ GeV} \tag{5.23}$$

were applied. If the charges of the scattered lepton and beam are opposite the event is subtracted as a charge-symmetric background event.

The leptons can be accompanied by several hadrons identified by

$$\mathrm{PID}_3 + \mathrm{PID}_5 < -1 \quad .$$

All identified hadrons where taken when they also fulfilled the fiducial volume and vertex cuts:

$$\begin{aligned} -18\ \text{cm} &\leq z_{\text{vertex}} \leq 18\ \text{cm} \quad , & (5.24)\\ |x_{\text{calo}}| &< 175\ \text{cm} \quad , & (5.25)\\ 30\ \text{cm} < |y_{\text{calo}}| &< 108\ \text{cm} \quad . & (5.26)\end{aligned}$$

Additionally the following semi-inclusive cuts were applied:

$$\begin{aligned} 2\ \text{GeV} < P_h &< 15\ \text{GeV} & (5.27)\\ 0.2 < z &< 0.7 & (5.28)\\ \theta_{\gamma,h} &> 0.02\ \text{rad} \quad , & (5.29)\end{aligned}$$

where $\theta_{\gamma,h}$ is the angle between the virtual photon and the produced hadron. The momentum range of hadrons is limited by the identification region of the RICH. The plots containing data binned in the kinematic variable z include also two additional bins between $z = 0.7$ and 1.2 which do not anymore belong to the semi-inclusive region as they might be populated mainly by exclusive events. The opening angle cut was motivated already in the Monte Carlo section. It avoids miscalculation of the azimuthal angles.

Results for charged pions and kaons are obtained using the RICH for the identification. Since the RICH can not be used for hadron identification for the data before run 809 its information is taken only for the runs starting with run 809.

$$\begin{aligned} \text{smRICH.iType} &= 3 \quad (\pi^+,\ \pi^-)\\ \text{smRICH.iType} &= 4 \quad (K^+,\ K^-)\\ \text{smRICH.rQp} &> 0\ , \end{aligned}$$

where rQp also contains a decadic logarithmic likelihood ratio for the 2 most probable hadron type hypotheses.

Additionally also neutral pions are identified by their two decay photons. The photons are detected with the calorimeter as trackless clusters. They must have an energy of

$$E_\gamma > 1\ \text{GeV}\ .$$

Due to their neutral charge photons were not bent in the spectrometer magnet. The fiducial volume cut for photons is therefore tighter, since photons at larger positions would have passed through the spectrometer magnet material.

$$\begin{aligned} |x_{\text{calo}}| &< 125\ \text{cm}\\ 33\ \text{cm} < |y_{\text{calo}}| &< 105\ \text{cm}\ . \end{aligned}$$

Two of these clusters must have an invariant mass close to the π^0 mass

$$0.1\ \text{GeV} < M_{\gamma\gamma} < 0.17\ \text{GeV}$$

and have to fulfill the above mentioned cuts on P_h, z, and $\theta_{\gamma,h}$. For the evaluation of the combinatorial γ background and its asymmetries the sidebands in the two-photon invariant mass distribution below and above the π^0 mass were taken:

$$(0.075 \text{ GeV} < M_{\gamma\gamma} < 0.1 \text{ GeV}) \quad || \quad (0.17 \text{ GeV} < M_{\gamma\gamma} < 0.195 \text{ GeV}) \quad .$$

5.3.3 Number of Events

In Table 5.1 the numbers of inclusive and semi-inclusive DIS events are summarized.

Table 5.1: Particle yields after data quality and (SI)DIS cuts.

	# of DIS	# of π^+	# of π^-	# of π^0	# of K^+	# of K^-
this analysis	606678	58613	41543	16338	13047	5075

5.4 Systematic studies

5.4.1 Correcting the effects of the target magnetic field

Measurements with transverse target polarization allow to distinguish between Collins type and Sivers type moments. Unfortunately, the necessary transverse magnetic field has visible effects on charged tracks – they are all deflected horizontally. This could in principle cause false asymmetries. Luckily, those cancel out in the method used. Nevertheless, correcting the tracks for additional deflection is necessary to regain the loss in resolutions. This is done by using the new TMC (Target Magnet Correction) program which has been explained in chapter 4. Both methods mentioned there use the most recent transverse target magnetic field map which was measured during the shutdown in March 2003 by a Hall probe.

Since the Monte Carlo studies did not show big differences in the extracted asymmetries with or without TMC it is not expected to see a significant variation in the data either. Fig. 5.19 shows the deviations from the asymmetries extracted with TMC method 2 in units of the statistical error and confirms the expectations. One can therefore conclude that since the reconstructed moments are independent of the track correction method the obtained results are not an artefact of the transverse target magnet.

5.4.2 Further studies on the data sample

Extraction method revisited As discussed in detail in the MC section it is also of interest, to compare the three moment reconstruction methods with real data. Fig. 5.20 shows the comparison expressed in deviations in units of the statistical error from the 2-dimensional fit method. One can see some deviations in the regions where both asymmetries

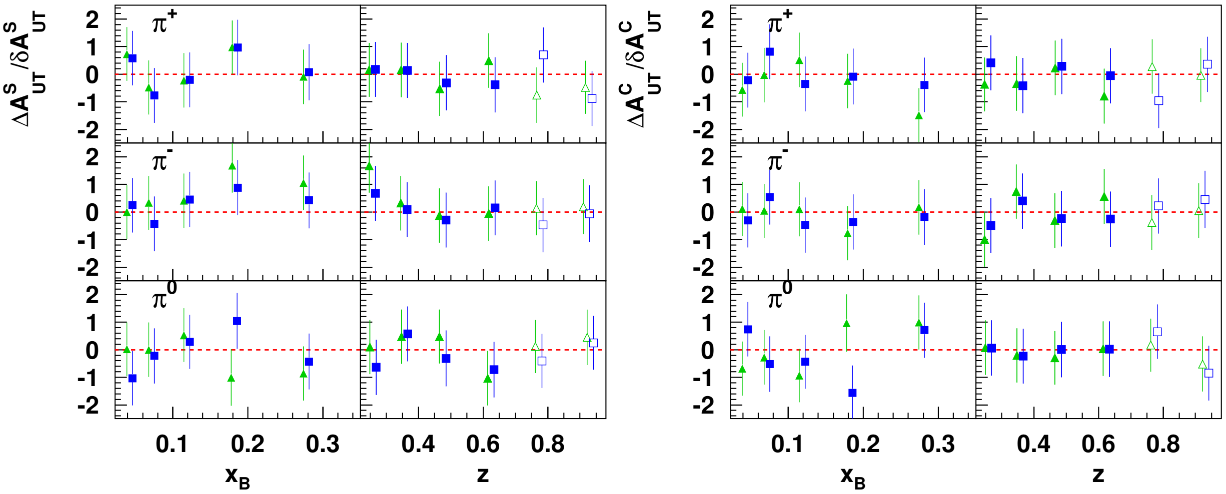

Figure 5.19: Comparison of the moments extracted without TMC (triangles) and extracted with TMC method 1 (squares) expressed in deviations from the moments extracted with TMC method 2. The open symbols represent the high z-points which are not part of the semi-inclusive sample. The π^0 results have not been corrected for combinatorial background. The left panel show the deviations for the Sivers type moments, the right panel that of the Collins moments.

are sizeable. This is the expected result of the mixing seen in the method comparison for MC data.

Higher moments As pointed out in the MC section the 2-dimensional fit method allows to fit more harmonics simultaneously. Fits have been performed including $\sin(3\phi - \phi_S)$ and other (higher twist) moments as well. The first moment is proportional to the Collins fragmentation function but contains $h_{1T}^{\perp}$ as a distribution function which measures the difference of the probabilities to find transversely polarized quarks in two transversely polarized nucleon states. This moment is fluctuating around 0 for all pion types. Including it in the overall fit also does not change the results for the Collins and Sivers asymmetries significantly. The stability of these moments including higher moments in the fit can be seen in Fig. 5.21, where also $\sin(3\phi + \phi_S)$, $\sin(\phi_S)$ and $\sin(2\phi + \phi_S)$ have been added to the fit successively. All these other moments are consistent with zero (Fig. 5.22).

Subsamples In the limited amount of statistics only a few stability tests can be done with different subsamples of the data:

- Events where the lepton is either in the top or in the bottom part of the detector
- Events where the hadron is either in the top or in the bottom part of the detector
- Any combination of the previous 2.

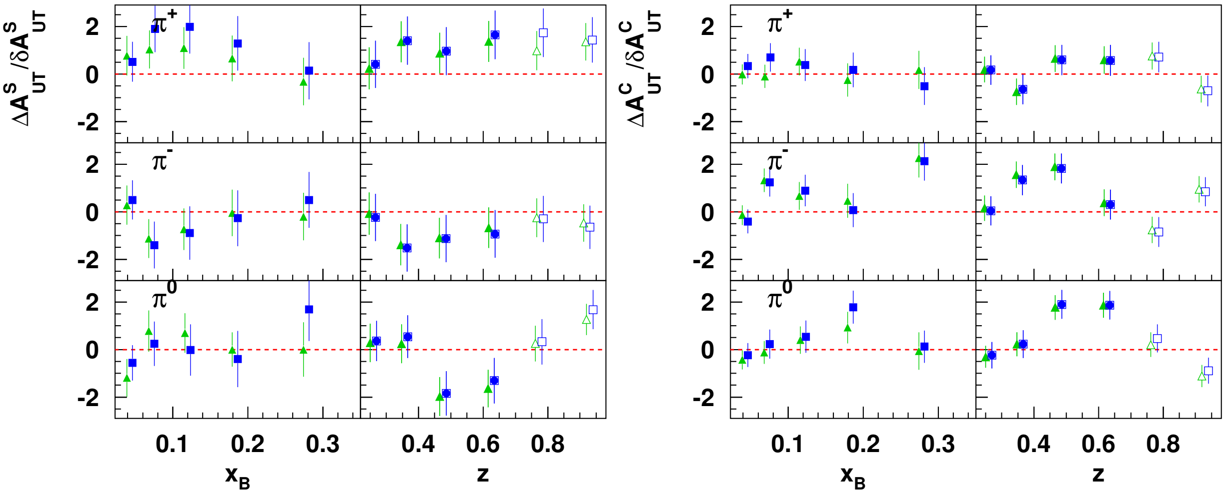

Figure 5.20: Comparison of the weighted(triangles) and the 1-dimensional fit (squares) method expressed in deviations from the 2-dimensional fit method. The open symbols represent the high z-points which are not part of the semi-inclusive sample. The π^0 results have not been corrected for combinatorial background. The left panel shows the deviations for the Sivers type moments, the right panel that of the Collins moments.

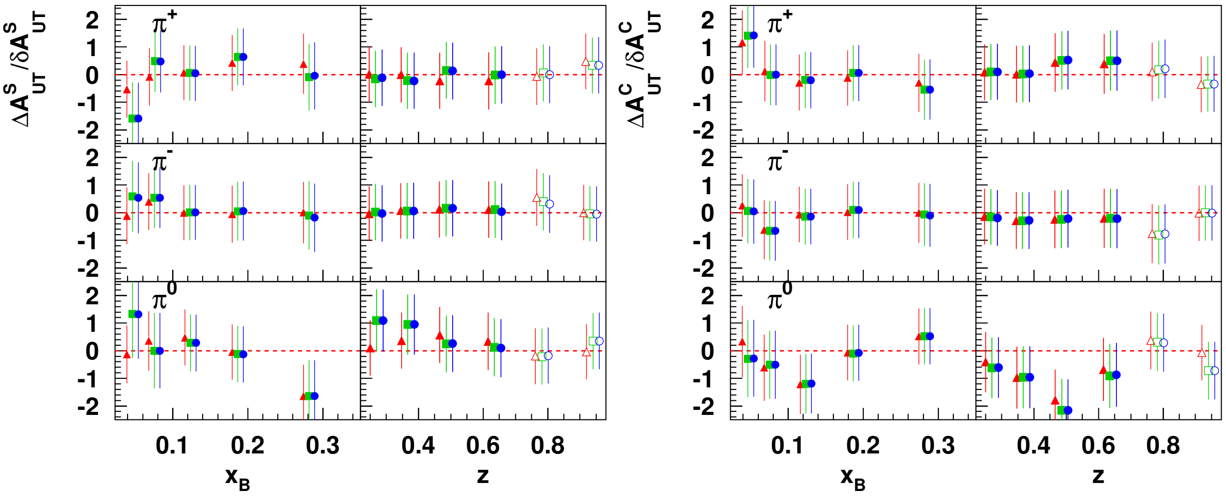

Figure 5.21: Deviations of the Sivers and Collins asymmetries in units of the statistical errors when successively including a $\sin(3\phi + \phi_S)$ (triangles), a $\sin(\phi_S)$ (squares) and a $\sin(2\phi + \phi_S)$ (circles) moment into the fit. The open symbols represent the high z-points which are not part of the semi-inclusive sample. The π^0 results have not been corrected for combinatorial background. The left panel shows the stability of the Sivers moments, the right panels that for the Collins moments.

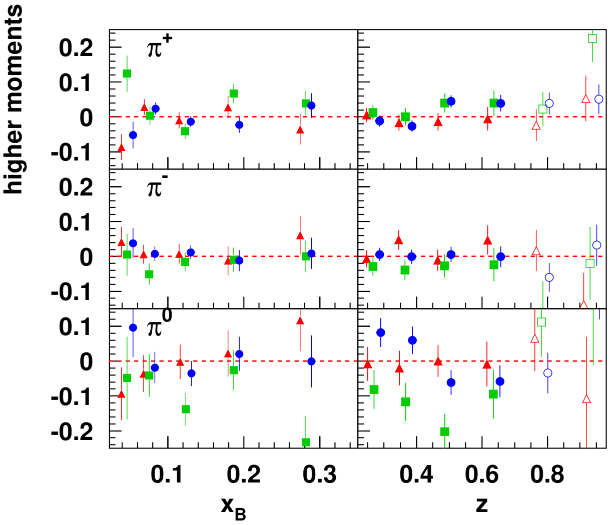

Figure 5.22: The $\sin(3\phi+\phi_S)$ (triangles), the $\sin(\phi_S)$ (squares) and the $\sin(2\phi+\phi_S)$ moments (circles) when fit simultaneously with the Sivers and Collins moments vs. x and z. The open symbols represent the high z-points which are not part of the semi-inclusive sample. The π^0 results have not been corrected for combinatorial background.

The results for those samples are summarized in Table 5.2 for the Collins type and in Table 5.3 for the Sivers type asymmetry. They agree within the statistical errors, although due to the general event topology the statistics for the sample where both particles are in the same detector half is extremely small.

Further tests were also preformed by splitting the data into two samples of consecutive runs with roughly equal statistics . This test would show any dependence of the asymmetries on the running conditions of the experiment. The results are in good agreement within statistical errors as displayed in table E.9.

Neutral pions The π^0 and its background can provide also another stability test on the asymmetries, as here a different event topology exists. Instead of detecting the charged hadrons in a combination of the PID-detector responses, the π^0 are only identified by the two photons in the calorimeter. It can be seen for the Collins asymmetries that the values of the charged pions seem always smaller than the theory predictions which will be discussed in greater detail in the next chapter. This cannot be explained by a wrong assumption on the magnitude of the Collins FF only. The question of a systematic error arises here. Therefore looking on the x and z behavior of the π^0's and the sidebands can give some hints on possibly hidden systematic effects. The asymmetries from the sideband of the π^0 peak should not contain a significant moment, while the π^0 peak should be roughly a combination of the π^+ and π^- moments. Indeed, as can be seen on Fig. F.3, the background is comparable with zero while the π^0 do show a slightly negative signal for the Collins type asymmetry and a positive signal for the Sivers type.

	π^+		
	TOP	BOT	ALL
e^+ TOP	-0.116 ± 0.067	0.022 ± 0.021	0.027 ± 0.019
e^+ BOT	0.047 ± 0.021	0.107 ± 0.066	0.051 ± 0.019
e^+ ALL	0.045 ± 0.019	0.032 ± 0.019	0.039 ± 0.014
	π^-		
	TOP	BOT	ALL
e^+ TOP	0.014 ± 0.077	-0.049 ± 0.025	-0.047 ± 0.023
e^+ BOT	-0.041 ± 0.026	-0.309 ± 0.073	-0.080 ± 0.023
e^+ ALL	-0.045 ± 0.023	-0.082 ± 0.023	-0.064 ± 0.016

Table 5.2: Collins type asymmetry for positrons/hadrons in the upper or lower part of the detector.

Entrance window, ghosts The entrance window to the spectrometer magnet is located at $z = 172$ cm and is defined by $|x| < 63$ cm and 6.8 cm $< |y| <$ 32.2 cm. In order to calculate the x and y position of the tracks at $z = 172$ cm one has to take the angles not corrected for the transverse target field as those angles define the track's geometry in the detector. When cutting out tracks which do not fulfill these acceptance cuts, the number of DIS events gets reduced by about 1%.
Another cut was additionally imposed as a check to the data sample. Sometimes, for example when a particle decays within the region of the spectrometer magnet, HRC cannot determine the correct bending of the track [Lie] and therefore gives a wrong momentum and/or charge. Following [Lie] a check for the correct bending of the tracks was performed and only tracks with the correct charge-bending relation were allowed. These wrong events only happened a few times for the whole semi-inclusive data sample.

The comparison of the asymmetries imposing these two cuts was shown in [BESS]. As there is no difference visible the cuts will be neglected in order to increase the already very limited statistics.

Asymmetries vs. $P_{h\perp}$ and Q^2 Figs. 5.23 show the unweighted Sivers and Collins asymmetries for pions versus Q^2 and $P_{h\perp}$. The asymmetries show hardly any significant dependence on $P_{h\perp}$ or Q^2 except possibly for the π^- Collins case, where one can see an increasing asymmetry with increasing $P_{h\perp}$ and also with Q^2. The non-existing Q^2 dependence for the other pions is quite promising, as assuming that the observed signals were higher twist, the asymmetries would decrease in higher Q^2 bins which is, however, not seen. Therefore this Q^2 behavior is showing, that one in fact sees the leading twist functions. Especially the

	π^+		
	TOP	BOT	ALL
e^+ TOP	-0.136 ± 0.061	0.024 ± 0.013	0.020 ± 0.012
e^+ BOT	0.047 ± 0.013	0.098 ± 0.061	0.049 ± 0.012
e^+ ALL	0.044 ± 0.012	0.023 ± 0.012	0.035 ± 0.009
	π^-		
	TOP	BOT	ALL
e^+ TOP	0.011 ± 0.068	0.011 ± 0.015	0.007 ± 0.015
e^+ BOT	-0.005 ± 0.015	0.030 ± 0.065	0.008 ± 0.014
e^+ ALL	-0.004 ± 0.014	0.022 ± 0.014	0.007 ± 0.010

Table 5.3: Sivers type asymmetry for positrons/hadrons in the upper or lower part of the detector.

Sivers asymmetries versus Q^2 are almost completely flat. In the plots vs. $P_{h\perp}$ no clear trend is visible. Except for the highest bins of the Collins asymmetries for π^- and π^0, the dependence seems rather flat as well. This is also convincing since the Collins function as well as the Sivers function should be sizeable only in the region of transverse momenta of up to the order of the nucleon mass.

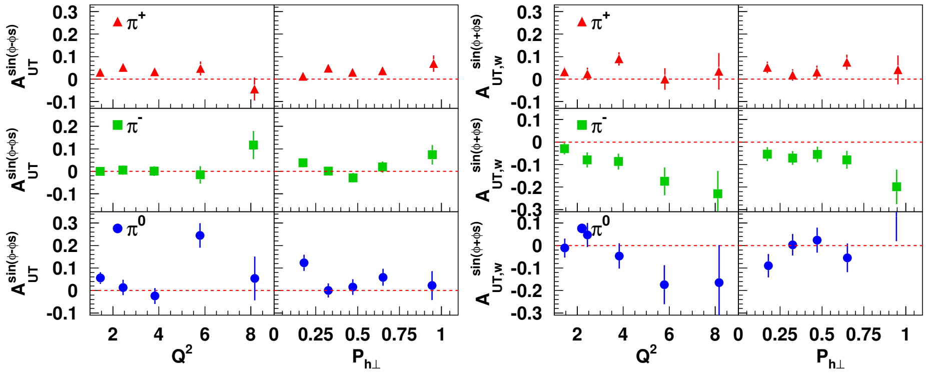

Figure 5.23: Unweighted asymmetries vs. Q^2 and $P_{h\perp}$. The Sivers moments are shown on the left panel, the Collins moments on the right panel. The π^0 results have not been corrected for combinatorial background.

Moments for one target spin state In the section on the MC studies 5.2 it was shown that a residual moment exists due to the transverse field of the target magnet, which vanished when using the target magnet corrected tracks. In the data there is still such a residual moment visible after applying the target magnet correction although it is already substantially smaller than for uncorrected tracks. For the complete semi-inclusive range the moments for pions in the two target spin states are summarized in Table 5.4 for the tracking correction method 2 and in 5.5 without tracking correction.

Table 5.4: Weighted moments for $\pi^{\pm}$ and π^0 in the semi-inclusive range for each target spin state and the combined results with track correction method 2

Moment	P_z^+	P_z^-	$1/2(A^+ - A^-)$	$1/2(A^+ + A^-)$
$A_{UT,\pi^+}^{\sin(\phi+\phi_S)}$	0.049 ± 0.013	-0.050 ± 0.013	0.050 ± 0.009	0.001 ± 0.009
$A_{UT,\pi^+}^{\sin(\phi-\phi_S)}$	0.072 ± 0.013	-0.040 ± 0.013	0.056 ± 0.009	0.016 ± 0.009
$A_{UT,\pi^-}^{\sin(\phi+\phi_S)}$	-0.095 ± 0.015	-0.018 ± 0.015	-0.038 ± 0.011	-0.057 ± 0.011
$A_{UT,\pi^-}^{\sin(\phi-\phi_S)}$	-0.064 ± 0.015	-0.050 ± 0.015	-0.007 ± 0.011	-0.057 ± 0.011
$A_{UT,\pi^0}^{\sin(\phi+\phi_S)}$	-0.000 ± 0.024	-0.038 ± 0.024	0.019 ± 0.017	-0.019 ± 0.017
$A_{UT,\pi^0}^{\sin(\phi-\phi_S)}$	0.011 ± 0.023	-0.060 ± 0.023	0.035 ± 0.017	-0.025 ± 0.017

Table 5.5: Weighted moments for $\pi^{\pm}$ and π^0 in the semi-inclusive range for each target spin state and the combined results without track correction

Moment	P_z^+	P_z^-	$1/2(A^+ - A^-)$	$1/2(A^+ + A^-)$
$A_{UT,\pi^+}^{\sin(\phi+\phi_S)}$	0.212 ± 0.012	0.129 ± 0.012	0.041 ± 0.009	0.171 ± 0.009
$A_{UT,\pi^+}^{\sin(\phi-\phi_S)}$	0.336 ± 0.013	0.217 ± 0.012	0.057 ± 0.009	0.277 ± 0.009
$A_{UT,\pi^-}^{\sin(\phi+\phi_S)}$	-0.127 ± 0.015	-0.053 ± 0.015	-0.036 ± 0.010	-0.090 ± 0.010
$A_{UT,\pi^-}^{\sin(\phi-\phi_S)}$	-0.205 ± 0.015	-0.196 ± 0.015	-0.003 ± 0.010	-0.201 ± 0.010
$A_{UT,\pi^0}^{\sin(\phi+\phi_S)}$	0.105 ± 0.023	0.075 ± 0.024	0.015 ± 0.017	0.180 ± 0.017
$A_{UT,\pi^0}^{\sin(\phi-\phi_S)}$	0.058 ± 0.023	0.011 ± 0.023	0.024 ± 0.016	0.035 ± 0.017

It can be seen that the results for the sum of the two spin states becomes a lot smaller when applying the target magnet correction . Nevertheless this sum still does not reach zero as expected for a perfect target field correction. Recall also that the MC-studies show a residual moment in the weighted moments without a target magnet correction, which vanish when using TMC. Significant residual moments in the data thus would show, that possibly the transverse target field map used in the MC and as well as a basis for the TMC programs still does not describe the transverse target field perfectly. On the other hand it was already shown that even while containing these residual moments the moments are reconstructed well. It was also shown in Fig. 5.19 that in the data the track correction method does not change the asymmetries. This is again confirmed by Table 5.5.

Fake asymmetries In Fig. F.4 the asymmetries for polarized data with randomly assigned target status are displayed. Of course these asymmetries should vanish, which apart from quite large fluctuations does happen. The integrated asymmetries are shown in Table 5.6 for the $P_{h\perp}/(zM_h)$-weighted and the unweighted case. One clearly sees that all asymmetries are within 1 σ around zero.

Table 5.6: Unweighted and $P_{h\perp}/(zM_h)$-weighted asymmetries for $\pi^\pm$and π^0 in the semi-inclusive range for arbitrary assigned spin states. The π^0 results are not background corrected.

	unweighted		$P_{h\perp}/(zM_h)$-weighted	
	$A_{UT}^{\sin(\phi-\phi_S)}$	$A_{UT}^{\sin(\phi+\phi_S)}$	$A_{UT}^{\sin(\phi-\phi_S)}$	$A_{UT}^{\sin(\phi+\phi_S)}$
π^+	-0.002 ± 0.009	-0.006 ± 0.014	-0.005 ± 0.012	0.012 ± 0.139
π^-	-0.016 ± 0.010	0.001 ± 0.016	-0.022 ± 0.015	0.082 ± 0.172
π^0	-0.005 ± 0.016	0.022 ± 0.026	-0.001 ± 0.023	0.235 ± 0.253

5.5 Sources of dilution

5.5.1 Combinatorial π^0 Background

For the neutral pions the contribution of the background $\gamma\gamma$-pairs has to be evaluated. As already stated in earlier works [A$^+$01b, A$^+$00, A$^+$03b] the invariant mass distribution is fit in each kinematic bin by a Gaussian for the π^0 contribution and a 2nd order polynomial for the background. The number of events as well as the signal to noise ratio are displayed in Fig. 5.24. Just as expected the background contribution almost vanishes when approaching the exclusive limit at high z, where no energy is left for any further photons.

The $\sin(\phi \pm \phi_S)$ moments of the background were also calculated for each kinematic bin, taking the 25 MeV sidebands of the π^0 peak from $0.75\ GeV < M_{\gamma\gamma} < 0.1\ GeV$ and $0.17\ GeV < M_{\gamma\gamma} < 0.195\ GeV$. Even though the statistics of these sidebands were very low it was possible to evaluate the asymmetries for almost every kinematic bin (for the highest z bin no asymmetry could be calculated, which therefore was assumed to be 0). After knowing the amount of background per bin as well as its magnitude the asymmetries

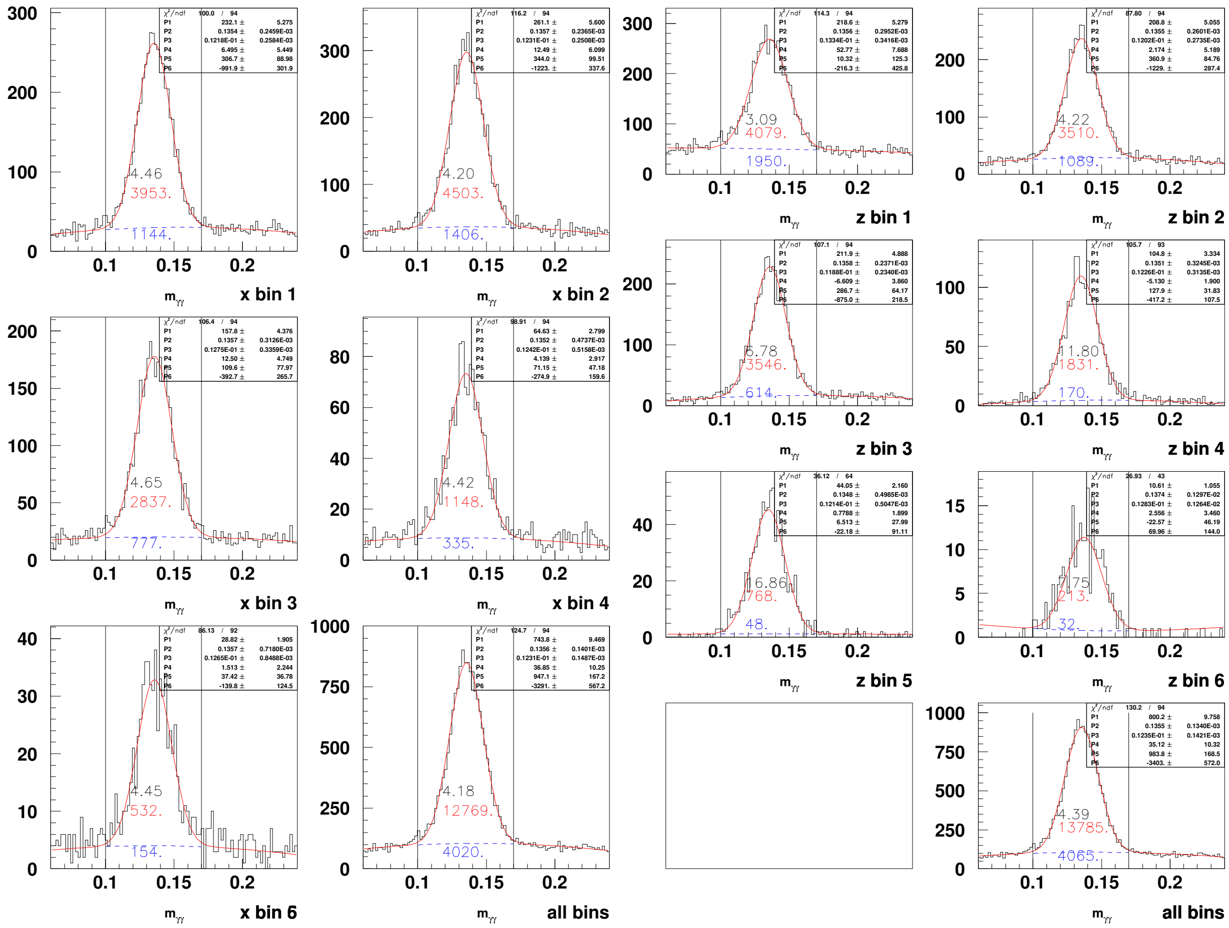

Figure 5.24: Left: invariant mass $m_{\gamma\gamma}$ fit by a Gaussian and a 2nd order polynomial in each of the x bins, right: invariant mass $m_{\gamma\gamma}$ fit by a Gaussian and a 2nd order polynomial in each of the z bins. The middle numbers are the π^0 events, the lower numbers are the BG events and the top number is the signal/noise ratio. Note that the last plot always represents all bins together, which includes in the z-binning also the 2 high z points above $z = 0.7$.

could be corrected for background using

$$A_{corr}^{\sin(\phi\pm\phi_S)} = A_{measured}^{\sin(\phi\pm\phi_S)} \left(\frac{N_{tot}}{N_{\pi^0}}\right) - A_{BG}^{\sin(\phi\pm\phi_S)} \left(\frac{N_{BG}}{N_{\pi^0}}\right) \quad . \tag{5.30}$$

The contribution to the statistical error was also taken into account as calculated in Appendix C.

5.5.2 Dilution and asymmetry transfer from exclusive vector-mesons

Dilution: Studies [Lie] concerning the dilution of semi-inclusive pseudo-scalar mesons by decay particles originating from exclusive vector mesons (i.e. ρs and ωs) showed that these effects can be quite sizable . As these studies were performed using the semi-inclusive cuts applied in the analysis of the helicity distributions Δq [A$^+$04, Wen, Bec], the dilutions had to be reevaluated using the cuts applied for the transversity analysis as stated before. For this purpose more statistics with a PYTHIA6 [SLMS03] setup recently tuned to HERMES kinematics [ALS03] were generated and analyzed. The process type of these events can be found in the MC data structure by (*g1MEvent.bProcess* $\gg$ 4 & 0xFF). The three exclusive processes

- Process 91: elastic diffractive vector meson dominance (VMD)
- Process 92: single diffractive VMD (broken up vector mesons)
- Process 93: single diffractive VMD (broken up proton)

can then be selected. By calculating the ratios of reconstructed pions originating from these processes to all pions within the transversity cuts it was possible to determine the dilutions for each x and z bin for all 3 pion charges. As an example Fig. 5.25 shows the dilutions of charged and neutral pions vs. x and z. They are in this study comparable to what was found in [Lie]. The dilutions vs. z are quite similar as the upper z-cut was released here. Differences show up in the dilution for the various x-bins since in the transversity analysis the upper cut on z is lower (0.7) than the one for the helicity analysis (0.8). Since the dilution increases strongly with z, [Lie] sees an on average larger contribution from exclusive VM production than seen in the present analysis.

Basically these studies can be performed similarly for the π^0s and their dilution originating from VMD processes, mostly the ω. One problem is that the PYTHIA MC files are generated with the smearing generator HSG97 [Men], which simulates the detector response for charged tracks, and thus neither the π^0 nor their decay photons get reconstructed. Therefore one had to rely on the generated π^0, requesting that their decay-gammas were in the box acceptance corresponding to the detector geometry. Then, their dilutions could be calculated as well and are also displayed in Fig. 5.25. These dilutions have been rescaled by a factor 1.5 as the cross section ratio of $\frac{\sigma_\omega}{\sigma_\rho}$ is a factor 1.5 too small in the tuned PYTHIA compared to HERMES measurements. In summary one can state that the π^0 dilution is less then 5 % for all x-bins while the dilutions for the charged pions are below 7 %. The dilutions of exclusive vector meson decay pions into the semi-inclusive data sample are also summarized in tables E.3 and E.4.

Asymmetry transfer: If π's originating from exclusive vector meson production would only constitute a dilution one could treat them like an unpolarized background, i.e. scale the measured asymmetries according to the amount of the dilution. However, there are predictions suggesting non-vanishing and in fact quite sizeable azimuthal asymmetries for those vector mesons themselves [GPV01]. If these asymmetries in the azimuthal angle of the vector meson with respect to the virtual photon also produce azimuthal asymmetries for the decay π's (i.e. when the momentum direction of one decay particle is basically the same as the one of the parent vector meson), then they will also affect the reconstructed

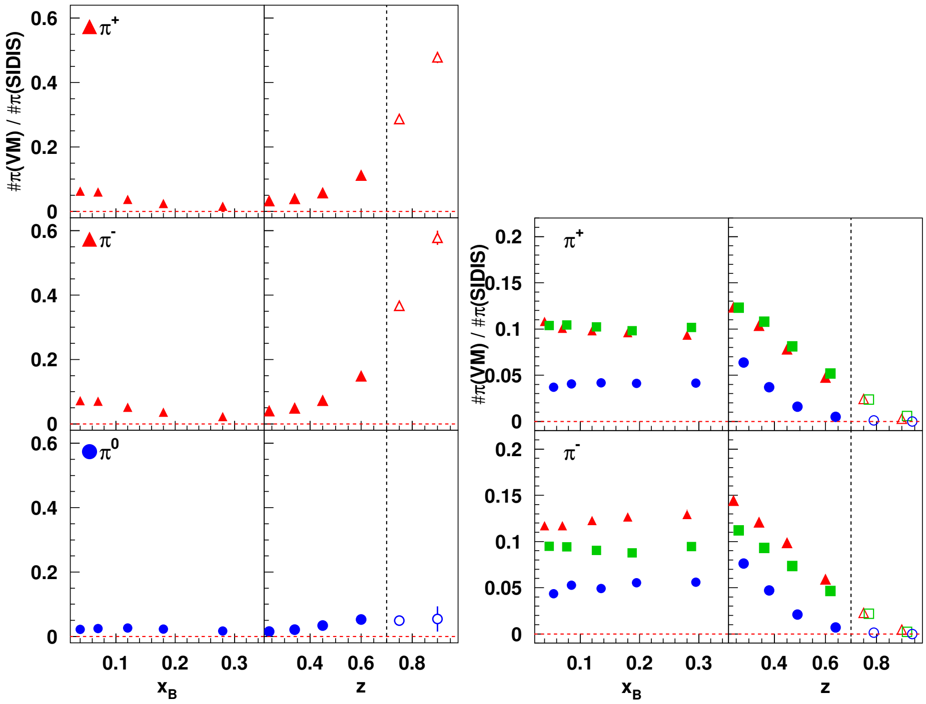

Figure 5.25: Left panel: Dilutions of the semi-inclusive pion data samples by pions from exclusive vector meson decay displayed vs. x and z. Right panel: Dilutions of the semi-inclusive pion data sample by pions from semi-inclusive vector meson decay displayed vs. x and z; the triangles, squares and circles represent the ρ^0 , $\rho^{\pm}$ and ω^0 contributions.

asymmetries for pions. To evaluate this asymmetry transfer azimuthal asymmetries were generated by weighting pions originating from VMD processes according to the azimuthal angle of the vector meson. For the semi-inclusive pions no asymmetry was generated. By reconstructing the azimuthal asymmetries one is able to calculate the transfer from the vector meson asymmetry to the overall pion asymmetry. As an example the π^+ asymmetries in the 6 z-bins are shown versus the generated ρ^0 asymmetry of Sivers type in Fig. F.5 and of Collins type in Fig. F.6.

These asymmetries can then be fit by a first order polynomial in the generated asymmetry. It can be clearly seen that a generated asymmetry gives a contribution to both types of pion asymmetries, i.e. Sivers and Collins. Therefore a most general formulation of the interpretative uncertainty due to exclusive vector meson background of the pion asymmetries contains always two elements of the transfer-matrix $T^{ij}(A^i_{UT,\mathrm{VM}} \rightarrow A^j_{UT,\pi})$:

$$\Delta A^j_{UT,\pi,\mathrm{VM}} = \frac{N_{BG}}{N_\pi} \left(\sum_{i \in \{Siv,Col\}} T^{ij} A^i_{UT,\mathrm{VM}} \right) \quad , \tag{5.31}$$

where each element is still a first order polynomial of its VM asymmetry although the constant term is small and can be neglected.

For this formalism one needs to know the actual exclusive VM moments. Once enough data will be collected one might be able to measure them including their kinematical dependences. At the moment, due to lack of data and theory predictions (at least for the Collins type asymmetry), on has to make assumptions on their magnitude, taking into account the positivity constraints: $|A_{UT,\mathrm{VM},Collins} \pm A_{UT,\mathrm{VM},Sivers}| \leq 1/2$ for the unweighted moments.

The standard deviation of this constraint gives an asymmetry of $1/2\sqrt{6}$ for each of the asymmetries which has been taken for the vector meson asymmetry values. The dilutions $D = \dfrac{N_{BG}}{N_{all}}$, the transfer values T^{ij} and the interpretative uncertainties $\Delta A^j_{UT,\pi,\mathrm{VM}}$ are summarized in tables E.5 and E.7 in appendix E. Since some people argue [BHM+02] that even diffractive processes are an intrinsic component of DIS, its contribution to the systematic uncertainty is assigned as additional interpretative uncertainty to the results to be shown.

5.5.3 Pions as semi-inclusive vector meson decay products

Similar to the exclusive vector mesons also vector mesons produced in the fragmentation process can be a source of dilution. Conventionally these are absorbed into the definition of the fragmentation functions. While this is certainly reasonable for the well known unpolarized fragmentation functions it is at least necessary to know the dilutions of semi-inclusive vector mesons when addressing the Collins function, since here according to some models [Art93] the spin of the outgoing hadron can define the sign of the Collins function. A large contribution of decayed semi-inclusive vector mesons to the pion sample could thus alter the magnitude of the Collins type asymmetries severely. Fortunately, as the transversity distribution part of the vector meson Collins type asymmetries is the same as that for the pseudo-scalar mesons its magnitude together with the (still valid) transfer values from tables E.5 to E.8 will be quite small even if the dilutions (see E.3 and E.4) are large.

Unlike the contribution of exclusive vector mesons which have the quantum numbers of the virtual photon, which therefore allowed only contributions of neutral vector mesons, also charged vector mesons will give a contribution in the semi-inclusive case. The basis to calculate these dilutions is again PYTHIA6 MC modified for HERMES where now the number of pions originating from vector mesons not created in the processes 91 to 93 were divided by all the pions which fulfilled the cuts. The dilutions for the charged pions are about 10% for both the charged and neutral ρ mesons vs. x while their magnitude is half as large for omega decays as shown in Fig. 5.25. As expected the dilutions vs. z are falling off quite rapidly with rising z as there energy conservation allows only few high-z pions being decay products. Note that due to the different treatment in the produced MC, no semi-inclusive π^0 dilutions have been calculated.

6

Results and interpretations

> *The theoretical knowledge of the transversity distributions is at this point comparable to that of the helicity distribution. What is called for is an experimental study of this object.*
> *Barone, Ratcliffe*

In this chapter the results will be presented for the two weighting methods. The asymmetries are then discussed and interpreted within the framework of simple phenomenological models. These models can explain some of the rather unexpected behavior although they are crude oversimplifications. Also the comparison with more sophisticated model predictions will be shown.

6.1 Integrated results

As mentioned already in the MC section (see 5.2) the events were binned in a 2-dimensional $\phi \times \phi_S$ binning with 8 bins each and the asymmetries were evaluated. The statistical errors on the 2-dimensional asymmetries were calculated according to equation C.3 for the unweighted asymmetries and according to equation C.2 for the $w_i = P_{h\perp}/(zM_h)$-weighted asymmetries. The moments were χ^2 minimized (see. appendix C) with a LU decomposition adapted from [PFTV88] and used in a separate PERL routine. A test [Els03] has been performed on the stability of different fitting procedures such as MINUIT [JR75] and a single value decomposition [PFTV88]. No significant deviations have been found.

The average kinematic values for the data sample for which the results will be presented here are integrated over the experimental acceptance $\langle x\rangle = 0.09$, $\langle y\rangle = 0.54$, $\langle z\rangle = 0.36$, $\langle Q^2\rangle = 2.41$ GeV^2 and $\langle P_{h\perp}\rangle = 0.41$ GeV. A detailed summary of the mean values for each kinematic bin can be found in appendix E in table E.10.

The pre-factors defined in equation 3.13 are generally integrated over when extracting these asymmetries. In order to obtain virtual photon asymmetries which only depend on the ratio of the products of the relevant distribution functions and fragmentation functions over their unpolarized counterparts one has to correct for these pre-factors. One possibility would be to weight each event with the inverse of $\frac{B(x,y)}{A(x,y)}$ for the Collins case, to get rid of its dependence. This would result in an effectively harder scale but badly affects the statistical precision due to the additional weights. A second possibility applied here is to correct for these factors after the fit by multiplying the Collins results with the inverse of $\frac{B(\langle x\rangle,\langle y\rangle)}{A(\langle x\rangle,\langle y\rangle)}$, using the mean values of these kinematic variables within each kinematic bin extracted. The virtual photon asymmetries to be presented are thus defined as

$$A^h_{UT}(\phi,\phi_s) = 2\bar{A}^h_C \frac{B(\langle x\rangle,\langle y\rangle)}{A(\langle x\rangle,\langle y\rangle)} \sin(\phi+\phi_s) + 2\bar{A}^h_S \sin(\phi-\phi_s) \tag{6.1}$$

for the unweighted case and

$$A^h_{UT}(\phi,\phi_s) = 2M_h A^h_C \frac{B(\langle x\rangle,\langle y\rangle)}{A(\langle x\rangle,\langle y\rangle)} \sin(\phi+\phi_s) + 2M_N A^h_S \sin(\phi-\phi_s) \quad , \tag{6.2}$$

for the $P_{h\perp}/z$-weighted case. The factor 2 takes care of the fact, that the cross section asymmetries give twice the ratio of polarized to unpolarized distribution and fragmentation functions. These asymmetries for a given z and x bin directly correspond to the charge weighted ratios integrated over the range of the corresponding bins:

$$A^h_C(\langle x\rangle,\langle z\rangle) = \frac{\sum_q e_q^2 \int dx \delta q(x) \int dz H_1^{\perp,(1),q\to h}(z)}{\sum_q e_q^2 \int dx q(x) \int dz D_1^{q\to h}(z)} \quad , \tag{6.3}$$

and

$$A^h_S(\langle x\rangle,\langle z\rangle) = \frac{\sum_q e_q^2 \int dx f_{1T}^{\perp,(1),q}(x) \int dz D_1^{q\to h}(z)}{\sum_q e_q^2 \int dx q(x) \int dz D_1^{q\to h}(z)} \tag{6.4}$$

for the weighted asymmetries.

The reduced χ^2 values of the fits fall in the range 0.74-1.89 for the unweighted asymmetries and 0.67-1.35 for the $P_{h\perp}/z$-weighted asymmetries. When fitting only the Sivers and Collins asymmetries, leaving out higher moments, which is the basis for the results to be shown in this chapter, the fits returned a correlation between the Sivers and Collins results between -0.6 and -0.5.

The weighted and unweighted Sivers and Collins asymmetries were also calculated within the whole kinematic range of the semi-inclusive DIS events, as can be seen in table 6.1.

	π^+	π^-	π^0	K^+	K^-
A_C	0.142 ± 0.070	-0.252 ± 0.086	-0.125 ± 0.200	-0.034 ± 0.039	0.079 ± 0.069
$\bar{A}_C$	0.020 ± 0.007	-0.032 ± 0.008	-0.021 ± 0.020	0.001 ± 0.014	0.021 ± 0.023
A_S	0.022 ± 0.006	0.004 ± 0.008	0.018 ± 0.018	0.058 ± 0.014	0.007 ± 0.023
$\bar{A}_S$	0.017 ± 0.005	0.004 ± 0.005	0.024 ± 0.013	0.037 ± 0.009	0.009 ± 0.015

Table 6.1: Sivers and Collins asymmetries with and without $P_{h\perp}/(zM_h)$ weighting evaluated for the whole semi-inclusive range of $0.2 < z < 0.7$.

6.2 Collins type asymmetries

6.2.1 Unweighted results

Fig. 6.1 shows the virtual photon asymmetries for the unweighted Collins moments. The data shows a positive π^+ asymmetry which seems to be slightly rising with x as is expected when approaching the valence region. The x behavior of the π^- asymmetries seems to be similar although negative and with higher magnitude than the π^+. The π^0 asymmetries are in between as expected and seem to favor slightly negative values. The Collins function should rise with z which seems to be the case when including the high-z points. The high z data is not completely semi-inclusive anymore since a certain fraction of these events originates from exclusive pion production.

6.2.2 $\frac{P_{h\perp}}{zM_\pi}$ weighted results

The $\frac{P_{h\perp}}{zM_\pi}$ Collins type asymmetries should give a cleaner interpretation than the unweighted asymmetries due to the assumption-independent deconvolution. Fig. 6.2 displays these virtual photon asymmetries for pions. An x-behavior similar to the unweighted asymmetries can be observed. Also here the π^- asymmetries are larger in magnitude than the π^+ asymmetries. Due to the additional weighting with $1/z$ one would expect an almost flat z-dependence of the Collins function. The data agree with such a behavior within errors.

6.2.3 Simple model calculations and internal consistency

The results for the Collins asymmetries, are quite surprising, since the asymmetries for the π^- are larger in magnitude than the corresponding π^+ asymmetries. Assuming a similar behavior for the transversity distributions as for the helicity distributions on would also have u-quark dominance for the transversity case, $|\delta u(x)| > |\delta d(x)|$ and an extra enhancement by the squared quark charges. When assuming for the Collins function a similar behavior as for the unpolarized fragmentation function $D_1(z)$, then unfavored fragmentation is literally

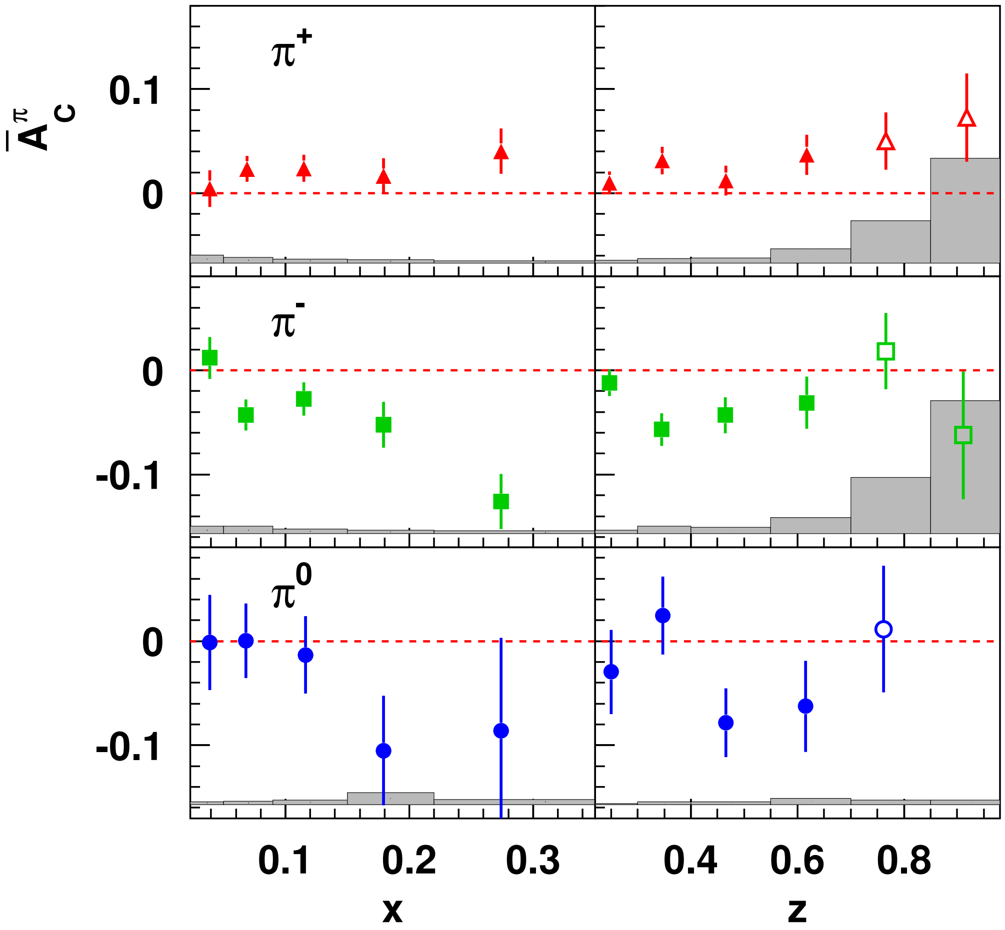

Figure 6.1: Collins type asymmetries for the pions as labeled, as a function of x and z. The error bars represent the statistical uncertainties, while the lower band represents the possible interpretive uncertainty from diffractive vector meson production. In addition, there is a common overall scale uncertainty in the asymmetries of 5% of the central value in each bin due to the target polarization uncertainties.

suppressed, ie.

$$H_1^{\perp,u\to\pi^+} > H_1^{\perp,u\to\pi^-} \tag{6.5}$$

$$H_1^{\perp,d\to\pi^-} > H_1^{\perp,d\to\pi^+} \quad . \tag{6.6}$$

The combination of these two assumptions would lead to a larger magnitude of the π^+ asymmetry than the π^- asymmetry which seems to be not supported by the data. Even though the magnitude of the transversity distributions still differs in various models, the previous assumption is valid in all of the models. One could therefore stick to the u-quark dominance assumptions while releasing the theoretically far less supported assumption for the relation between favored and unfavored Collins fragmentation. Let us assume that the Collins function is universal for different quark types and hence contains only a favored and

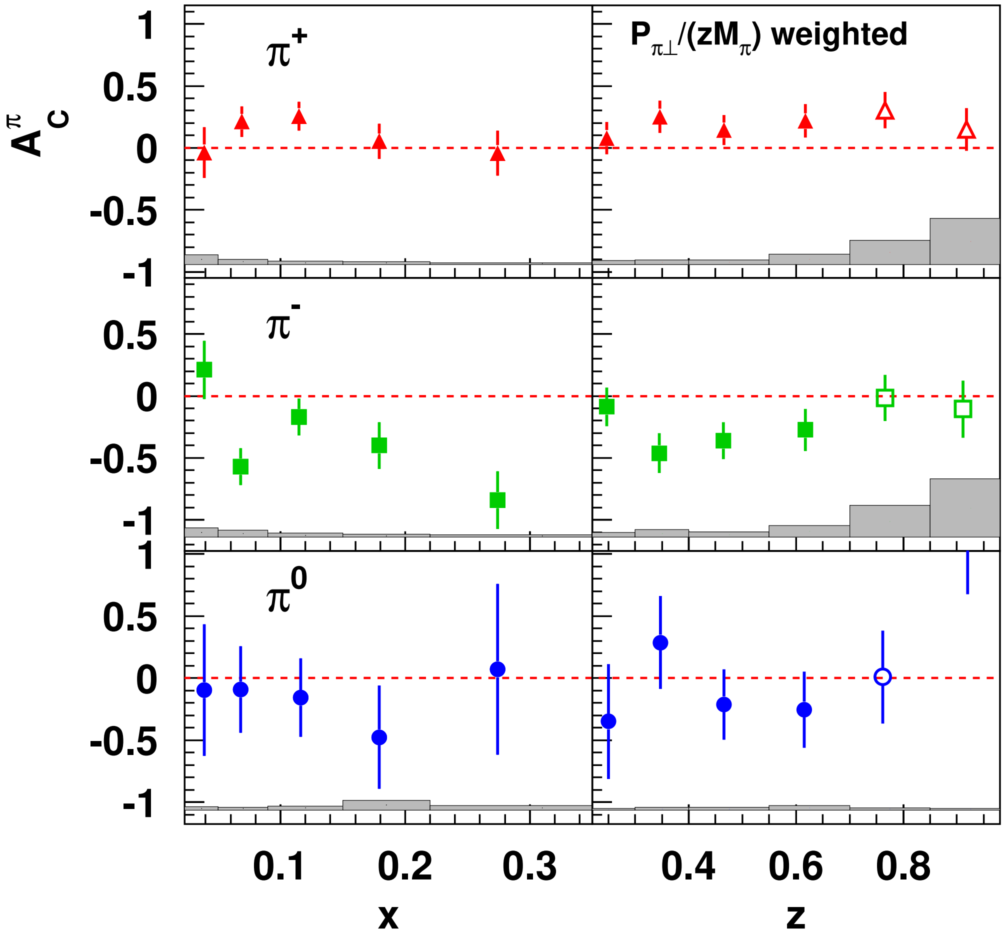

Figure 6.2: $|P_{h\perp}/(zM_h)|$-weighted Collins type asymmetries for the pions as labeled, as a function of x and z. The error bars represent the statistical uncertainties, while the lower band represents the possible interpretive uncertainty from diffractive vector meson production. In addition, there is a common overall scale uncertainty in the asymmetries of 5% of the central value in each bin due to the target polarization uncertainties.

a disfavored part:

$$H_{1,fav}^{\perp,(1)}(z) = H_1^{\perp,(1),u\to\pi^+}(z) = H_1^{\perp,(1),d\to\pi^-}(z) \tag{6.7}$$

$$H_{1,dis}^{\perp,(1)}(z) = H_1^{\perp,(1),u\to\pi^-}(z) = H_1^{\perp,(1),d\to\pi^+}(z) \quad . \tag{6.8}$$

A similar assumption can also be made for the corresponding (1/2) moments. Having these assumptions at hand one can rewrite the 3 measured $P_{h,\perp}/(zM_\pi)$ weighted asymmetries according to their quark content, neglecting strange quarks:

$$A_C^{\pi^+} = \frac{\sum_q e_q^2 \delta q(x) H_{1,q\to\pi^+}^{\perp,(1)}(z)}{\sum_q e_q^2 q(x) D_{1,q\to\pi^+}(z)} \tag{6.9}$$

$$= \frac{\big(\delta u(x) + 1/4\delta\bar{d}(x)\big)\, H_{1,fav} + \left(1/4\delta d(x) + \delta\bar{u}(x)\right) H_{1,dis}}{\big(u(x) + 1/4\bar{d}(x)\big)\, D_{1,fav} + \left(1/4 d(x) + \bar{u}(x)\right) D_{1,dis}} \tag{6.10}$$

$$A_C^{\pi^-} = \frac{\left(1/4\delta d(x) + \delta\bar{u}(x)\right) H_{1,fav} + \big(\delta u(x) + 1/4\delta\bar{d}(x)\big)\, H_{1,dis}}{\left(1/4 d(x) + \bar{u}(x)\right) D_{1,fav} + \big(u(x) + 1/4\bar{d}(x)\big)\, D_{1,dis}} \tag{6.11}$$

$$A_C^{\pi^0} = \frac{\big(\delta u(x) + 1/4\delta\bar{d}(x) + 1/4\delta d(x) + \delta\bar{u}(x)\big)\left(H_{1,fav} + H_{1,dis}\right)}{\big(u(x) + 1/4\bar{d}(x) + 1/4 d(x) + \bar{u}(x)\big)\left(D_{1,fav} + D_{1,dis}\right)}. \tag{6.12}$$

It is then possible to regroup these terms in ratios of polarized and unpolarized distribution and fragmentation functions, which are defined as

$$r(x) \equiv \frac{d(x) + 4\bar{u}(x)}{u(x) + 1/4\bar{d}(x)} \tag{6.13}$$

$$\mathcal{D} \equiv \frac{D_{1,dis}(z)}{D_{1,fav}(z)} \tag{6.14}$$

for the unpolarized (and thus known) quantities and

$$\delta r(x) \equiv \frac{\delta d(x) + 4\delta\bar{u}(x)}{\delta u(x) + 1/4\delta\bar{d}(x)} \tag{6.15}$$

$$\eta_H \equiv \frac{H_{1,dis}(z)}{H_{1,fav}(z)} \tag{6.16}$$

for the polarized (and thus unknown) quantities. The ratios of the fragmentation functions simply describe the ratio between disfavored to favored fragmentation of a quark into a hadron. For the unpolarized part this can be evaluated by fits to be around 0.55 [KLC01, KLC02] while the value extracted from a phenomenological assumption of $\mathcal{D} = \frac{1-z}{1+z}$ [FF78] gives 0.38. These ratios were calculated by integrating the parameterizations over the measured z range from 0.2 to 0.7. The ratio $r(x)$ of unpolarized distribution functions can also be determined by fits [P$^+$02], giving in leading order a value of 1.20 which is integrated over the whole experimental HERMES acceptance (ie. between $0.023 < x < 0.4$ with a mean value of $\langle x \rangle = 0.09$). Using these ratios the redefined asymmetries can be described as

$$A_C^{\pi^+}(x,z) = \mathcal{K}(x,z)\,\frac{1 + 1/4\delta r(x)\eta_H(z)}{1 + 1/4 r(x)\mathcal{D}(z)} \tag{6.17}$$

$$A_C^{\pi^-}(x,z) = \mathcal{K}(x,z)\,\frac{\eta_H(z) + 1/4\delta r(x)}{\mathcal{D}(z) + 1/4 r(x)} \tag{6.18}$$

$$A_C^{\pi^0}(x,z) = \mathcal{K}(x,z)\,\frac{(1 + 1/4\delta r(x))(1 + \eta_H(z))}{(1 + 1/4 r(x))(1 + \mathcal{D}(z))} \quad , \tag{6.19}$$

where the common pre-factor

$$\mathcal{K}(x,z) = \frac{(\delta u(x) + 1/4\delta\bar{d}(x))H_{1,fav}^{\perp}(z)}{(u(x) + 1/4\bar{d}(x))D_{1,fav}(z)} \tag{6.20}$$

describes the supposedly leading part of the π^+ asymmetry. This set of three equations with three unknowns can unfortunately not be solved, since the equations are not independent. They can be combined in such a way that no unknown quantities appear in the remaining equation

$$A_C^{\pi^+}(x,z) + C(x,z)A_C^{\pi^-}(x,z) - (1 + C(x,z))A_C^{\pi^0}(x,z) = 0 \quad , \tag{6.21}$$

where the pre-factor $C(x,z)$ is defined as

$$C(x,z) = \frac{r(x) + 4\mathcal{D}(z)}{r(x)\mathcal{D}(z) + 4} \quad . \tag{6.22}$$

Although equation 6.21 will not allow to solve the set of equations it provides a useful test of consistency on the measured asymmetries. Inserting these together with $C = 0.728$ yields 0.174 ± 0.358 for the weighted asymmetries which is quite promising, as it tells that the data is consistent within the 1σ level. The statistical error has been calculated treating the 3 statistical errors of the asymmetries independently.

Since $\mathcal{K}$ appears in all of the 3 equations 6.17, 6.18 and 6.19 dividing the last 2 by equation 6.17 gives two limiting relationships between δr and η_H. These relations allow to define trajectories in the $\delta r, \eta_H$ space. Additionally one can sample possible asymmetry values by Gaussian distributions of the asymmetries around their measured values with a variation of their statistical errors. For this purpose the CERNLIB function RNORML has been applied to give the sampled asymmetries as

$$A_{sampled,i} = A_{meas,i} + \delta A_{meas,i} \cdot \mathrm{RNORML}_i \quad \text{with} \quad i \in \{\pi^+, \pi^-, \pi^0\}\,, \tag{6.23}$$

since RNORML throws a Gaussian distribution with width one around zero. Such a result for 10000 sampled sets of asymmetries is displayed in Fig. 6.3. The horizontal lines represent the limits of a plausible Collins ratio $-1 < \eta_H < 1$ since it is not expected to find a disfavored Collins function larger than its favored counterpart. The vertical lines represent the plausible limits around the central value of $\delta r \approx -0.26$ as taken from chiral quark soliton model predictions by [WK99] and $\delta r \approx -0.34$ [S$^+$01] which were also integrated over the measured x-range. One sees that the majority of the trajectories within the plausible ranges has a tendency to η_H values below zero, close to -1 while the δr value seems to be quite unconstrained by the sampled values. The region with the highest likelihood far outside the plausible ranges corresponds to a pole in the asymmetry ratios and is therefore unphysical.

When displaying just the slice of δr at exactly the predicted value as presented in Fig. 6.4 one sees that the likelihood of η_H tends to a value of η_H close to -1. While the Figs. 6.3 and 6.4 where generated sampling *data* points around the measured asymmetry values ignoring the consistency equation it is also possible to use this constraint and hence produce only 2

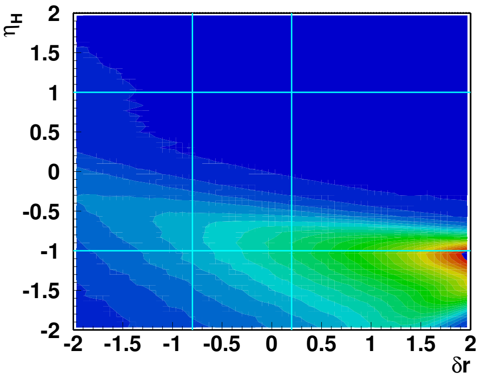

Figure 6.3: Likelihood distribution of η_H vs δr based on statistical uncertainties of the measured asymmetries around their central values.

independent arbitrary asymmetries taking the third asymmetry by implying the consistency equation. Such a procedure is displayed in Fig. 6.5, where one clearly sees that the enhancement of trajectories stays unchanged with respect to the unconstrained sampling method. Since the highest likelihood region within the plausibility ranges stays almost horizontally one has only little sensitivity to the δr ratio. Nevertheless one can use the applied sampling method as well to populate other combinations of the 3 unknown quantities. For example taking a uniform distribution in δr it is possible to visualize the likelihood distributions of $\mathcal{K}$ versus δr and η_H against $\mathcal{K}$ as displayed in Fig. 6.6.

One can see that a small but positive $\mathcal{K}$ value is favored similar to most of the predictions while η_H is again likely to be negative.

Shifted center values When one applies the same procedure to asymmetries whose center values were shifted one still would end up with an increased likelihood for a negative η_H. As an example the solution space for sampled asymmetries with π^- and π^0 moments shifted by the statistical error upwards displays a favorable η_H which is still slightly negative (see Fig. 6.7). Only when one shifts all asymmetries upward by one sigma a small value for η_H close to 0 is preferred. Note that in this case one obtains also a sensitivity in δr since now the highest likelihood region is not anymore flat in η_H.

6.2.4 Interpretation

The findings of the population of solution space in the previous section do favor a negative disfavored to favored Collins function ratio $\eta_H \approx -1$ while showing little sensitivity to the δr ratio. Since the unpolarized fragmentation functions give just the probability for the

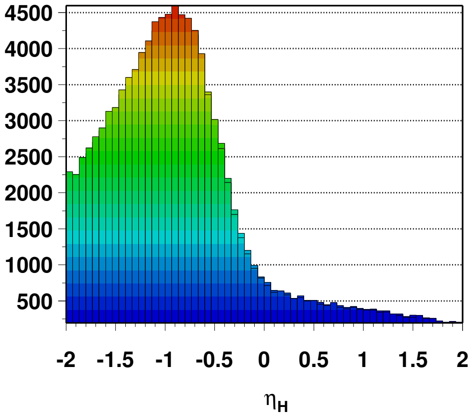

Figure 6.4: A slice of the likelihood distribution of 6.3 at $\delta r = -0.3$ which is the mean value of those predicted by the CQSM in [WK99] and [S$^+$01].

fragmentation of a quark q into a hadron h those functions have to contain only positive values. In the case of the Collins fragmentation function a left-right asymmetry is produced in the fragmentation process, thus including an orientation into the fragmentation function. Then this orientation allows for a sign which seems to come into play between the favored and disfavored part of $H_1^\perp$. This would mean that the favored part $H_{1,fav}^\perp$ creates hadrons in a $\sin(\phi+\phi_S)$ distribution while the unfavored part $H_{1,disf}^\perp$ creates hadrons in a $-\sin(\phi+\phi_S)$ distribution. How can this be understood?

A possible explanation can be found in the description of the Collins function proposed by Artru [Art93] following a string model description of fragmentation [Sjo95]. The struck quark flips its transverse spin and is kicked out of the nucleon. Since it is a colored object it carries a gluonic string connecting the quark with the remainders of the nucleon. At some distance the energy of the string becomes large enough to produce a quark-antiquark pair whose antiquark will form a meson together with the struck quark. Further mesons might be created in successive string breakings of the remaining string between the remains of the nucleon and the just created quark. Note that the string breaking can occur at any point in this gluonic string, resulting in several hadrons without any hierarchy of their energies. Therefore the struck quark does not necessarily end up in the leading (i.e. most energetic) hadron as some people mistakenly assume [Kot03]. The quark-antiquark pairs created in this process are expected to preserve the vacuum quantum numbers $J^P = 0^+$. Since a positive parity cannot be created by anti-aligning the spins of the quark and the antiquark they have to be aligned and compensated by a total angular momentum $L = 1$. This means that the quarks are rotating around each other which creates additional transverse momentum when the antiquark will eventually form a pseudo-scalar meson with the struck quark. Since the transverse spin of the struck quark has a definitive orientation the antiquark has to have

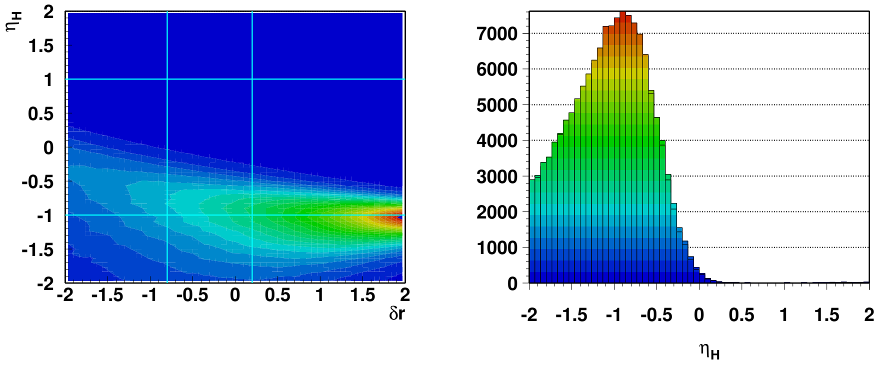

Figure 6.5: Likelihood distribution of η_H vs δr based on statistical uncertainties of the measured asymmetries around their central value taking into account the consistency equation 6.21.

the opposite orientation in order to form a pseudo-scalar meson. Therefore the transverse momentum the formed meson has gained will have a definitive direction, too. In the transverse spin orientation of the struck quark as in Fig. 6.8 the first pseudo-scalar meson would be going out of the paper plane creating a positive Collins function. Following this line of thought once more the quark which was created in the first string break and has the spin in the opposite direction as the struck quark already contains some transverse momentum in the opposite direction as the first meson and will eventually gain even more transverse momentum in that direction by the next string break, picking up the orbital angular momentum of the second antiquark with which it forms the second meson. This second meson will therefore create a negative Collins function. Any further mesons will consequently appear with alternating Collins functions. Accordingly the favored Collins function and the disfavored Collins function within this model are always of opposite sign. To some extend this reflects just momentum conservation, as the transverse momentum of all created final states has to vanish and gives a trivial manifestation of the Terayev-Schäfer sum rule.

Semi-inclusive VM production For semi-inclusive vector meson production the transverse spin of the struck quark and the antiquark have to be aligned giving the formed meson the transverse momentum in the opposite direction as for pseudo-scalar mesons. This results in an opposite Collins fragmentation function for semi-inclusive vector mesons with respect to the pseudo-scalar mesons and should be observable.

The longitudinally polarized deuteron data was analyzed for semi-inclusive ρ^0-mesons in a similar way as reported for the pseudo-scalar pions [A$^+$03b] imposing an additional cut on the invariant mass of the $\pi^+\pi^-$ pair between 0.6 GeV $< M_{hh} <$ 0.9 GeV. Unfortunately even in that mass region the combinatorial background dominates over the signal. Applying

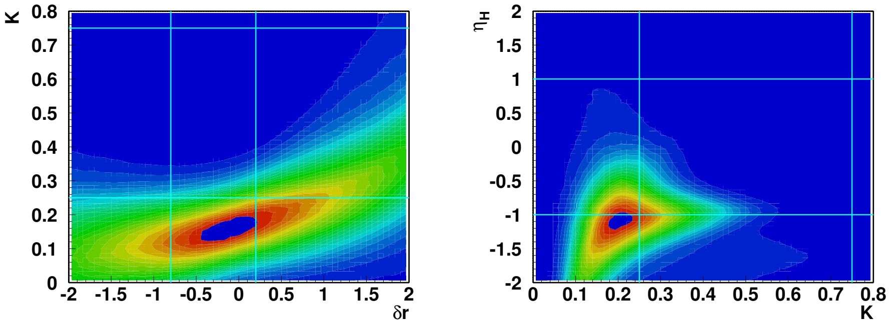

Figure 6.6: Left: Likelihood distribution of $\mathcal{K}$ versus δr , right: Likelihood distribution of η_H versus $\mathcal{K}$.

a background correction on the $\sin\phi$ moments by the moments of a background normalized wrong charge combination of pions one sees $A_{UL}^{\sin\phi}$ moments compatible to zero, although with quite large statistical errors due to that background correction.
Since the Sivers contribution to the UL asymmetries should not change its sign relative to the pseudo-scalar mesons this zero result is already an indication for a sign change of the Collins function relative to the pseudo-scalar asymmetries, which supports this string fragmentation picture.

6.2.5 Comparison with theory predictions

Several models can give predictions for transversity. The two different predictions from the chiral quark soliton model [Wak01, WK99, KPG96a] are displayed in panel 6.9 for $x(4/9\delta u + 1/9\delta\bar{d})$ and $x(1/9\delta d + 4/9\delta\bar{u})$ at $Q^2 = 2.5$ GeV, which is close to the scale of HERMES. Both models agree on a positive δu and a negative δd which are of similar magnitude as the corresponding quark helicities Δu and Δd. The antiquark transversities seem to have a larger magnitude in [Wak01]. Further predictions have been calculated in [MSY02b, MSY02a] for the quark-diquark model and a perturbative QCD approach.

Additionally also a few model calculations for the Collins function have been reported recently by [GGO04], following the gauge link description of Brodsky first proposed to describe the Sivers function. It is based on the idea to create a naive T-odd function by the interference of amplitudes with and without a gluon link between the non-perturbative part and the quark propagator. This mechanism, when applied to the fragmentation part of the semi-inclusive diagrams, is also applicable to create the Collins function.

[Bac02, BKMM02] did also predict weighted asymmetries based on modeling the $u \rightarrow \pi^+$ Collins function with the constituting quark model while taking the nonrelativistic limit $\delta u = \Delta u$ and the Soffer bound $\delta u = \frac{1}{2}(\Delta u + u)$ where the simple parameterizations of

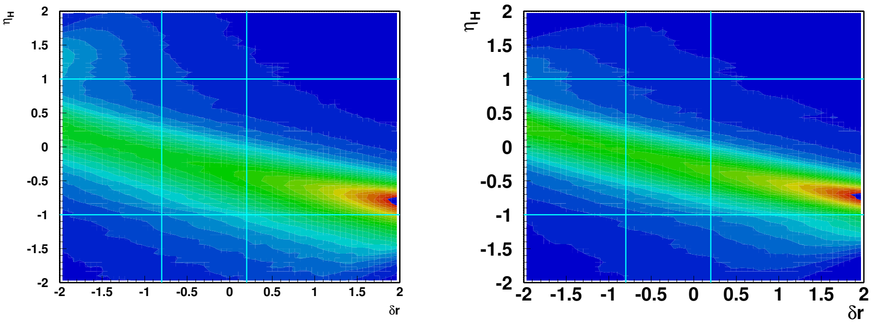

Figure 6.7: Likelihood distribution of η_H vs δr based on statistical uncertainties of the measured asymmetries around their central values. Left: Both the π^- and π^0 center values were shifted by 1 standard deviation in the stat. error. Right: All center values were shifted by 1 standard deviation in the stat. error.

[BBS95] were used for the unpolarized and helicity distributions.

Unfortunately none of these Collins predictions has calculated more than the favored Collins fragmentation function. The predictions show an increasing Collins function with z and of sizeable magnitude. The combinations of the transversity with the Collins calculations allows also to predict the magnitude of the single spin asymmetries measurable in SIDIS. Some theorists also used a private fit to DELPHI e^+e^- fragmentation data giving a z-averaged value of $\frac{\langle H_1^{\perp,(1/2)}\rangle}{\langle D_1\rangle} = 6.3\ldots 12.5\%$ [EST99] or tried to fit the Collins function to longitudinally polarized HERMES single spin asymmetries by assuming their chiral quark soliton predictions to be correct [EGS02a] giving a value of $\frac{\langle H_1^{\perp,(1/2)}\rangle}{\langle D_1\rangle} = 12.8\%$. Due to recent developments in the understanding of the Sivers function, which were not known at that time, its contribution to the A_{UL} asymmetries was also neglected. Also some of the higher twist terms appearing in the cross section 3.23 were not taken into account.

The predictions of [MSY02b] also use the Efremov result, taking into account the possibility of unfavored Collins fragmentation based on the relations for the unpolarized fragmentation functions. They therefore do get contributions to the asymmetries due to the unfavored Collins function although based on their assumptions these have the same sign as for the favored function. The comparison with theory predictions is shown in Fig. 6.10. It can be seen that at least the π^+ asymmetries show a behavior comparable to the theory predictions although the magnitude is generally lower. The statistical errors would not allow to distinguish between models, as all give quite similar predictions. Such a distinction would anyway be questionable as only one of the models takes into account a disfavored Collins fragmentation as may be indicated by the data. Therefore it is not surprising that the theory predictions seem to underestimate the large negative π^- asymmetry. The few negative data

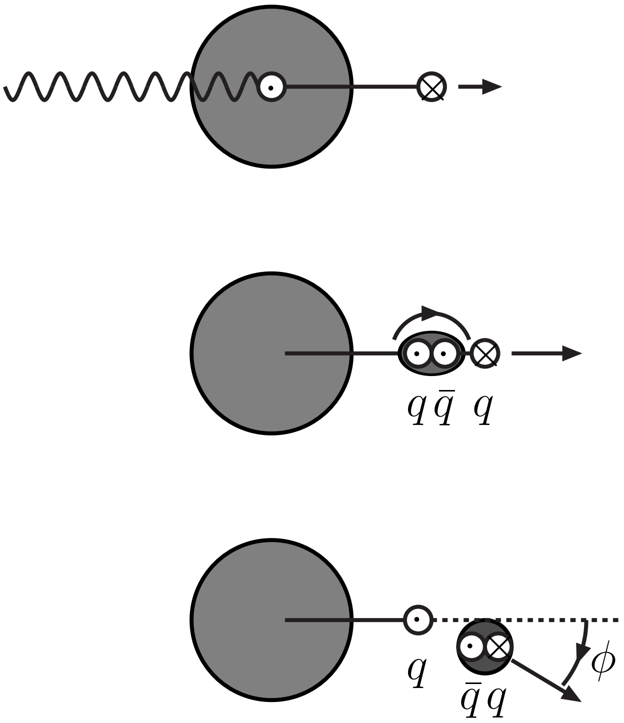

Figure 6.8: A schematic view of the fragmentation of a quark into a pseudo-scalar hadron gaining transverse momentum by the orbital angular momentum of the quark-antiquark pair created in the string breaking.

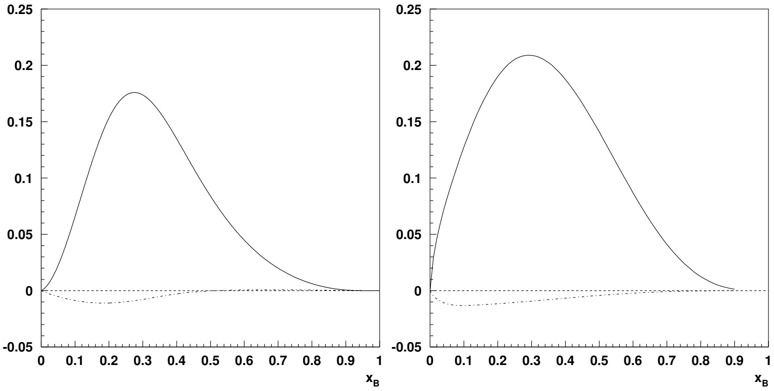

Figure 6.9: Predictions for $x(4/9\delta u + 1/9\delta\bar{d})$ (solid lines) and $x(1/9\delta d + 4/9\delta\bar{u})$ (dash-dotted lines). Left: predictions from [Wak01]; right: predictions from [KPG96a].

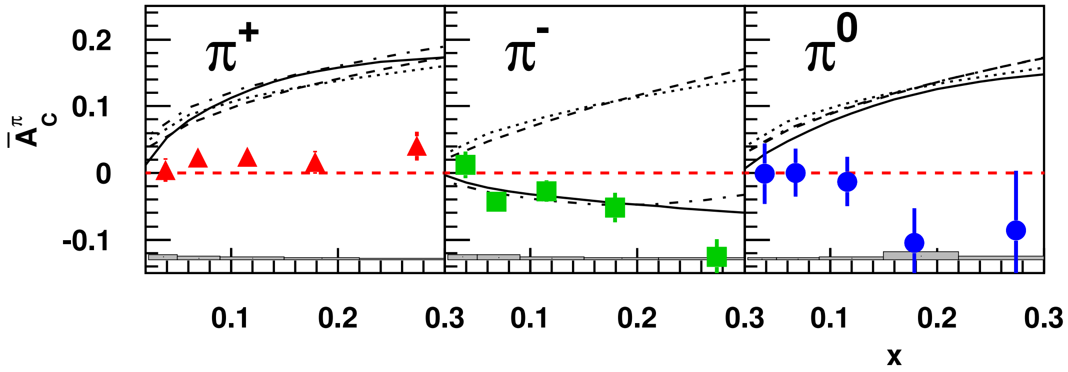

Figure 6.10: Unweighted Collins type asymmetries for π^+, π^- and π^0 (data points) compared to theory predictions. The full lines represent the predictions from the chiral soliton model [EGS03] taking into account only favored fragmentation. The dotted lines also include disfavored fragmentation in the quark-diquark model [MSY02b]. Dashed and dash-dotted lines represent the pQCD predictions from [MSY02b] for favored only and favored and disfavored fragmentation.

points of the unweighted π^0 asymmetry cannot be explained at all since they are proportional to $(\delta u + \delta d)(H_{1,fav} + H_{1,disf})$ which can only get negative when either $-\delta d > \delta u$ or $-H_{1,disf} > H_{1,fav}$ which is unlikely. They can only be explained by the large error bars allowing for zero or even slightly positive values for most of the bins.
An interesting ansatz was used by [SB04] applying transversity predictions from [S$^+$01] together with the Collins fragmentation prediction [BKMM02]. Two different assumptions on the intrinsic transverse momentum dependence in the nucleon were investigated. Either the intrinsic momentum dependence was omitted by applying a δ-distribution or a Gaussian ansatz with a width of $\langle \mathbf{p}_T^2 \rangle = 0.5$ GeV^2 was taken. The model predicts a quite sizeable difference of the asymmetries for higher z values as can be seen in the comparison plot with the HERMES data in Fig. 6.11. Unfortunately the overall magnitude seems to be described by neither of the assumptions very well. As argued already before the picture could be quite different when a disfavored Collins fragmentation with negative sign will be taken into account in the model predictions. Then, the two quite different assumptions can be really compared with the data, especially the π^+ asymmetries will then allow to even distinguish between them.

Additionally [SB04] and [BKMM02] did also provide predictions for $P_{h\perp}/M_\pi$-weighted asymmetries. Those are compared in Fig. 6.12 after dividing the theory predictions with z to compare the same quantities. Both the theory and the data seem to favor an almost flat z dependence although the magnitudes are again rather different. Also shown in Fig. 6.12 are the predictions of [GGO04, GHO04, GGO03b] which are based on an ansatz for the T-odd distribution and fragmentation functions by implementing a model for the gauge link proposed by [BHS02] and adding a Gaussian dependence of the intrinsic transverse momentum $\mathbf{k}_T$.

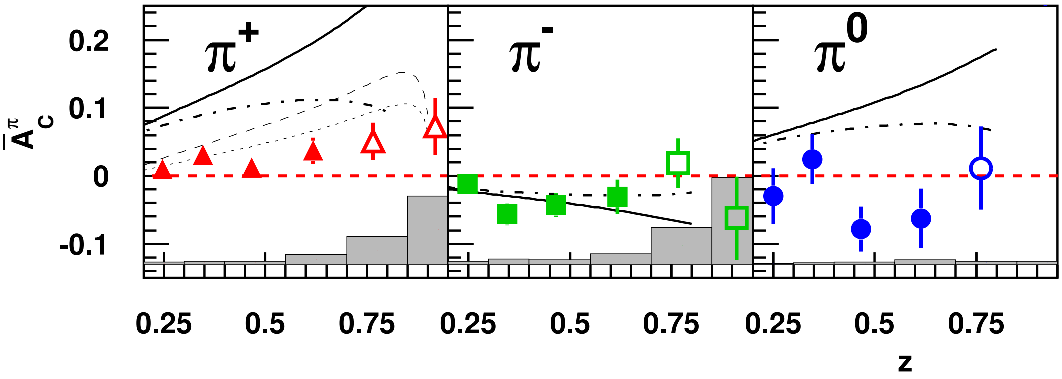

Figure 6.11: Unweighted Collins type asymmetries for π^+, π^- and π^0 (data points) compared to theory predictions. The full lines represent the predictions from [SB04] taking into account only favored fragmentation and assuming a vanishing transverse momentum dependence; the dash-dotted lines assume a Gaussian transverse momentum dependence. The dotted lines are predictions from [BKMM02] assuming $\delta u = \Delta u$, while the dashed lines assume $\delta u = 1/2(\Delta u + u)$.

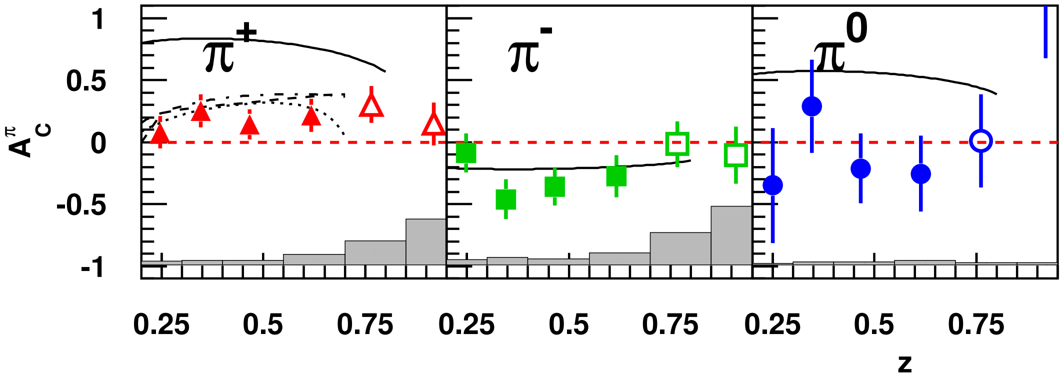

Figure 6.12: $P_{h\perp}/(zM_\pi)$-weighted Collins type asymmetries for π^+, π^- and π^0 (data points) compared to theory predictions. The lines represent the predictions from [SB04] taking into account only favored fragmentation. The dotted lines are predictions from [BKMM02] assuming $\delta u = \Delta u$, while the dashed-dotted lines assume $\delta u = 1/2(\Delta u + u)$. The dashed line in the π^+ asymmetries is from [GHO04, GGO03b] using a quark-diquark model including an additional gauge link to create the Collins function.

6.3 Sivers type asymmetries

6.3.1 Unweighted results

HERMES has measured the first Sivers asymmetries in semi-inclusive DIS. These measurements are also the first direct measurement of the Sivers function. Fig. 6.13 shows the unweighted Sivers asymmetries versus the kinematic variables x and z. As can be seen in the figure the π^+ asymmetries contain a sizeable nonzero result for the low x data points which seem to rise with rising z. A similar observation can be seen for the π^0. The asymmetries for π^- seem to be compatible with zero. Therefore one can already conclude that the Sivers function is not vanishing.

6.3.2 $\frac{P_h^\perp}{zM_N}$ weighted results

The hint of a positive Sivers asymmetry for the π^+ and a zero results for the π^- shown in the unweighted asymmetries does also appear in the $\frac{P_h^\perp}{zM_N}$ weighted asymmetries. The first measurements are displayed in Fig. 6.14 versus x and z. As already mentioned before these weighted asymmetries are the theoretically cleaner objects as they de-convolute the quark distribution and fragmentation part.

6.3.3 Simple model calculations and internal consistency

A similar procedure as for the Collins asymmetries can also be performed for the Sivers asymmetries. Due to the unpolarized fragmentation function D_1 appearing both in the denominator and the numerator the three asymmetries are directly proportional to the Sivers functions. Taking into account only u and d quarks and isospin symmetry for the fragmentation functions the three asymmetries can be rewritten as

$$A_S^{\pi^+} = \frac{\sum_q e_q^2 f_{1T}^{\perp,(1),q}(x) D_{1,q\to\pi^+}(z)}{\sum_q e_q^2 q(x) D_{1,q\to\pi^+}(z)} \tag{6.24}$$

$$= \frac{\left(f_{1T}^{\perp,(1),u}(x) + 1/4 f_{1T}^{\perp,(1),\bar{d}}(x)\right) D_{1,fav} + \left(1/4 f_{1T}^{\perp,(1),d}(x) + f_{1T}^{\perp,(1),\bar{u}}(x)\right) D_{1,dis}}{\left(u(x) + 1/4 f_{1T}^{\perp,(1),\bar{d}}(x)\right) D_{1,fav} + \left(1/4 d(x) + f_{1T}^{\perp,(1),\bar{u}}(x)\right) D_{1,dis}} \tag{6.25}$$

$$A_S^{\pi^-} = \frac{\left(1/4 f_{1T}^{\perp,(1),d}(x) + f_{1T}^{\perp,(1),\bar{u}}(x)\right) D_{1,fav} + \left(f_{1T}^{\perp,(1),u}(x) + 1/4 f_{1T}^{\perp,(1),\bar{d}}(x)\right) D_{1,dis}}{\left(1/4 d(x) + f_{1T}^{\perp,(1),\bar{u}}(x)\right) D_{1,fav} + \left(u(x) + 1/4 f_{1T}^{\perp,(1),\bar{d}}(x)\right) D_{1,dis}} \tag{6.26}$$

$$A_S^{\pi^0} = \frac{\left(f_{1T}^{\perp,(1),u}(x) + 1/4 f_{1T}^{\perp,(1),\bar{d}}(x) + 1/4 f_{1T}^{\perp,(1),d}(x) + f_{1T}^{\perp,(1),\bar{u}}(x)\right) (D_{1,fav} + D_{1,dis})}{\left(u(x) + 1/4 f_{1T}^{\perp,(1),\bar{d}}(x) + 1/4 d(x) + f_{1T}^{\perp,(1),\bar{u}}(x)\right) (D_{1,fav} + D_{1,dis})} \tag{6.27}$$

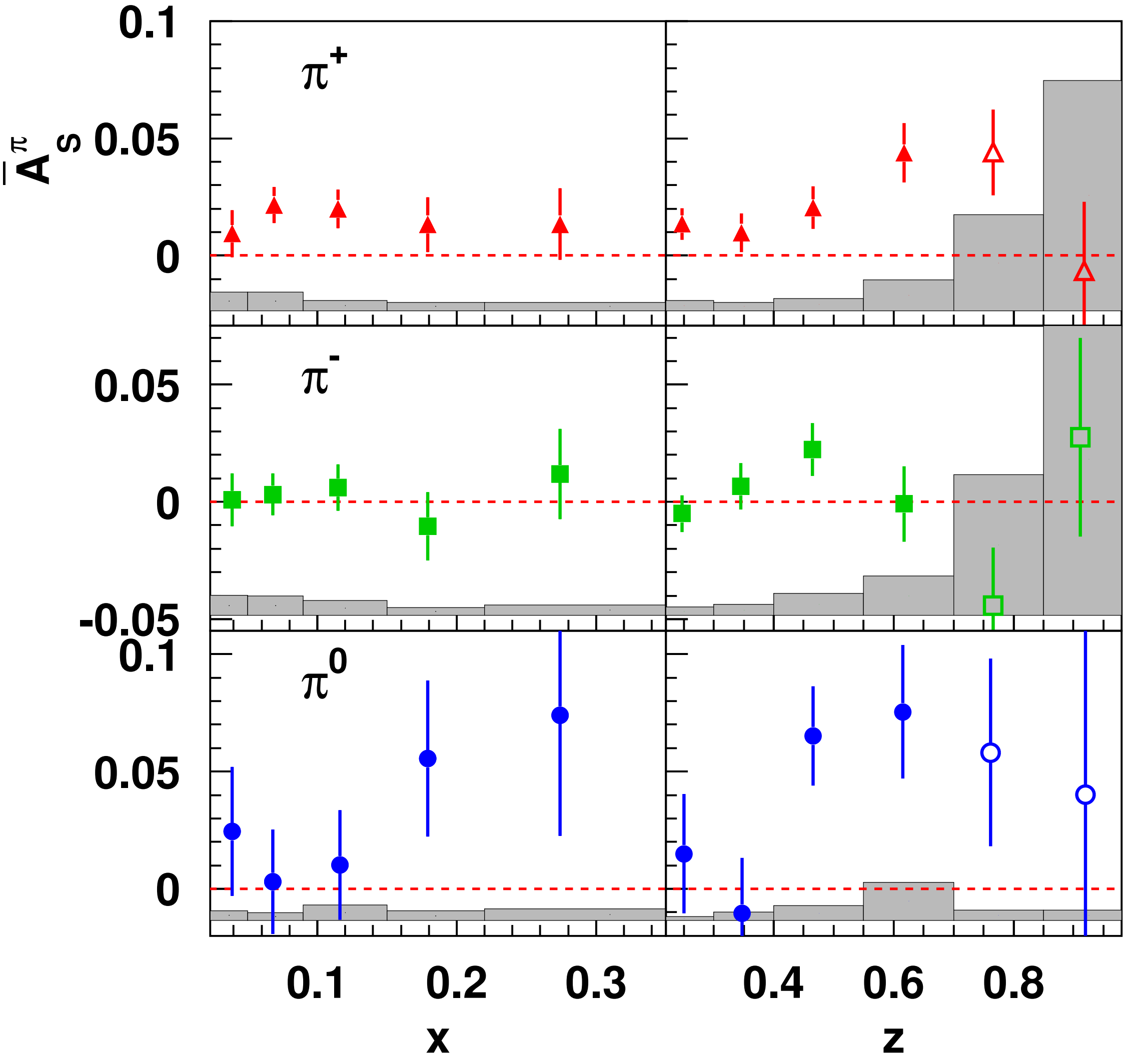

Figure 6.13: Sivers type asymmetries for the pions as labeled, as a function of x and z. The error bars represent the statistical uncertainties, while the lower band represents the possible interpretive uncertainty from diffractive vector meson production. In addition, there is a common overall scale uncertainty in the asymmetries of 5% of the central value in each bin due to the target polarization uncertainties.

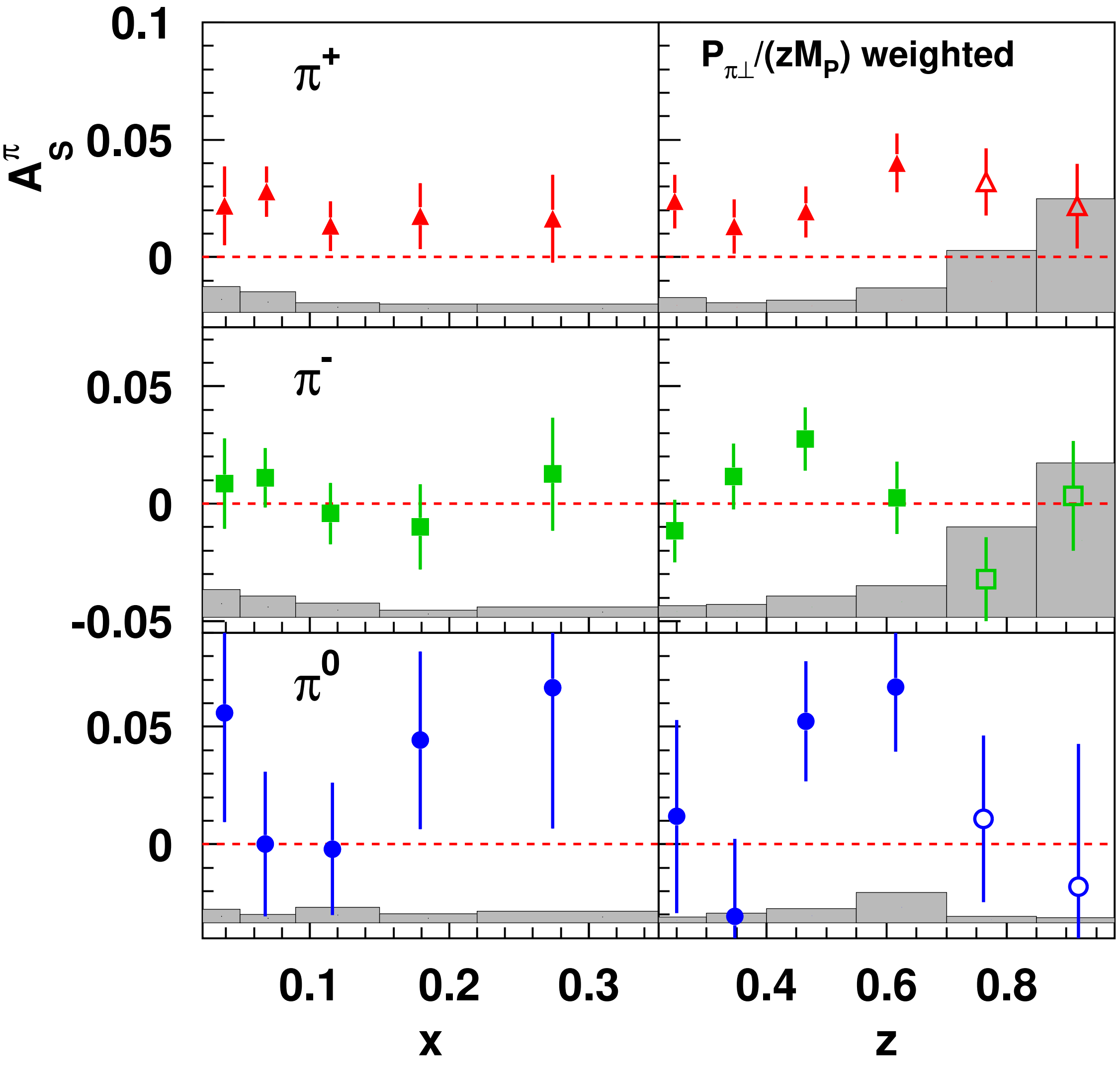

Figure 6.14: $|P_{h\perp}/(zM_N)|$-weighted Sivers type asymmetries for the pions as labeled, as a function of x and z. The error bars represent the statistical uncertainties, while the lower band represents the possible interpretive uncertainty from diffractive vector meson production. In addition, there is a common overall scale uncertainty in the asymmetries of 5% of the central value in each bin due to the target polarization uncertainties.

Following the same procedure as outlined in section 6.2.3 the asymmetries can be rewritten as

$$
\begin{aligned}
A_S^{\pi^+}(x,z) &= \mathcal{K}^\star(x,z)\,\frac{1+1/4\delta r^\star(x)\mathcal{D}(z)}{1+1/4r(x)\mathcal{D}(z)} && (6.28)\\
A_S^{\pi^-}(x,z) &= \mathcal{K}^\star(x,z)\,\frac{\mathcal{D}(z)+1/4\delta r^\star(x)}{\mathcal{D}(z)+1/4r(x)} && (6.29)\\
A_S^{\pi^0}(x,z) &= \mathcal{K}^\star(x,z)\,\frac{(1+1/4\delta r^\star(x))(1+\mathcal{D}(z))}{(1+1/4r(x))(1+\mathcal{D}(z))} \quad , && (6.30)
\end{aligned}
$$

where the unpolarized quantities $\mathcal{D}$ and r are defined as specified in equations 6.13, $\delta r^\star$ now contains the ratio

$$
\delta r^\star(x) \equiv \frac{f_{1T}^{\perp,(1),d}(x)+4f_{1T}^{\perp,(1),\bar{u}}(x)}{f_{1T}^{\perp,(1),u}(x)+1/4f_{1T}^{\perp,(1),\bar{d}}(x)} \quad , \tag{6.31}
$$

and $\mathcal{K}^\star$ is defined as the ratio between Sivers function and the corresponding unpolarized quantity:

$$
\mathcal{K}^\star(x,z) = \frac{f_{1T}^{\perp,(1),u}(x)+1/4f_{1T}^{\perp,(1),\bar{d}}(x)}{u(x)+1/4\bar{d}(x)} \quad . \tag{6.32}
$$

The consistency equation thus becomes:

$$
A_S^{\pi^+}(x,z)+C(x,z)A_S^{\pi^-}(x,z)-(1+C(x,z))A_S^{\pi^0}(x,z)=0 \quad . \tag{6.33}
$$

For the weighted asymmetries one obtains a value of -0.0067 ± 0.0319 and the consistency condition is therefore almost perfectly fulfilled. As a consequence of such a good agreement of the data it is possible to extract the Sivers *polarizations*, lacking better words.

$$
\begin{aligned}
\frac{f_{1T}^{\perp,(1),u}(x)+1/4f_{1T}^{\perp,(1),\bar{d}}(x)}{u(x)+1/4\bar{d}(x)} &= -0.035 \pm 0.011 && (6.34)\\
\frac{f_{1T}^{\perp,(1),d}(x)+4f_{1T}^{\perp,(1),\bar{u}}(x)}{d(x)+4\bar{u}(x)} &= 0.056 \pm 0.036 && (6.35)\\
f_{1T}^{\perp,(1),u}(x)+1/4f_{1T}^{\perp,(1),\bar{d}} &= -0.046 \pm 0.015 && (6.36)\\
f_{1T}^{\perp,(1),d}(x)+4f_{1T}^{\perp,(1),\bar{u}} &= 0.088 \pm 0.056 \quad . && (6.37)
\end{aligned}
$$

One sees that the Sivers functions are already rather well constrained by the data. Furthermore there is a clear indication that u and d quark Sivers functions have an opposite sign. The $f_{1T}^{\perp,(1),d}(x)+4f_{1T}^{\perp,(1),\bar{u}}$ component seems to be larger in magnitude than the $f_{1T}^{\perp,(1),u}(x)+1/4f_{1T}^{\perp,(1),\bar{d}}$ component, although they still could be of the same size within the errors. Unfortunately one cannot relate this large value directly to a larger Sivers function for down quarks relative to up quarks since the sea contributions might become quite sizeable even at mean $\langle x\rangle$ of 0.09.

6.3.4 Interpretation

The observation of nonzero Sivers functions can give already a hint to the contributions of the orbital angular momentum of u and d quarks to the spin of the nucleon. Following the idea of [Bur02] one can describe the scattering also in an impact parameter formalism. Such a formalism is usually only important in exclusive reactions measuring generalized parton distributions where the proton stays intact and only gains additional four momentum $t = (\mathbf{P}^T - \mathbf{P}'^T)^2$ which is the Fourier transformed of the impact parameter $\mathbf{b}^T$ (see chapter B). In semi-inclusive DIS all amplitudes are related by the optical theorem to forward amplitudes, where the nucleon does not gain any additional momentum, corresponding to $t = 0$. Fourier transforming this integral over the $\delta(t)$ distribution (in momentum space) corresponds to a flat integration in impact parameter (i.e. position) space. As a consequence one is averaging over all impact parameters in semi-inclusive DIS. If the quark distribution in impact parameter space is not centered it could still be observable as left-right asymmetries around the center. This is in fact what the Sivers function is producing. Since the rescattering by the gluons forces the struck quark to turn to the left, when a quark to the right of the center of the nucleon is hit and vice versa, it creates a sensitivity to where in impact parameter space the struck quark was. The question is still how such a de-central impact parameter distribution of the quarks can be created?

Figure 6.15: A top view of the re-scattering process when a quark left(right) of the nucleon center was hit is displayed on the left(right).

As already mentioned in chapter 3 the Sivers function is only non-vanishing when one does not integrate over the intrinsic transverse quark momentum. The transverse momentum dependence in the Sivers function requires a nonzero orbital angular momentum of the quarks in the nucleon. Assume in a classical picture, that the quarks of flavor q have a nonzero angular momentum $\mathbf{L_q}$ parallel to the spin of the transversely polarized nucleon at a nonzero distance $\mathbf{b}$. This corresponds to a non-vanishing intrinsic quark momentum $\mathbf{p}'$ which adds to the fractional nucleon momentum xP^+ carried by the quark. Therefore the x_{obs} calculated by the lepton kinematics corresponds to the sum of the quark's momenta collinear with the virtual photon:

$$x_{obs}P^+ = xP^+ + p^+(\mathbf{b})' \quad , \tag{6.38}$$

or by dividing with P^+ to

$$x_{obs} = x + x'(\mathbf{b}) \tag{6.39}$$

at a given $\mathbf{L}_q$. Since the unpolarized quark distribution $q(x)$ is not flat in x the probabilities to find quarks at a fixed x_{obs} depend on the x' and thus also on the impact parameter $\mathbf{b}$. This corresponds to the fact that the probability to find quarks on one side is higher than that to find quarks on the other side which results in the observable single spin asymmetries. Such a model was proposed and calculated by [Bur02] showing indeed a non-centered quark distribution in the nucleon when allowing the quarks to have a orbital angular momentum transverse to the virtual photon direction as displayed in Fig. 6.16.

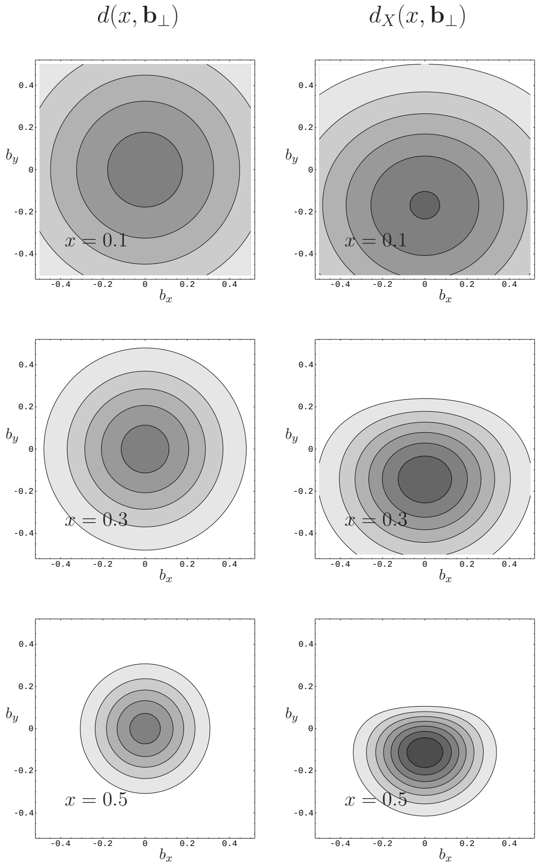

Figure 6.16: d quark distributions in impact parameter space for 3 different x values. Left panel: without orbital angular momentum of the quarks, right panel: with orbital angular momentum pointing in the positive x-direction.

6.3.5 Comparison with theory predictions

Brodsky [BHS02] presented a first model calculation of a non-vanishing Sivers-function by adding the gauge link showing that the Collins proof of vanishing T-odd distribution and fragmentation functions is only valid when interchanging initial and final state. The interference of the tree level graph and the one-loop graph including a gluon line are creating such a T-odd function. The asymmetries were calculated in a quark-spectator diquark model. Here only the intrinsic transverse momentum difference transferred by the additional gluon line was taken into account but no intrinsic transverse momentum dependence of the quarks in general was modeled, leading to transverse asymmetries of the order of 20 to 30%. Several groups refined this idea and were able to calculate predictions for the Sivers asymmetries as well. These predictions are based on the same model adding a Gaussian dependence on the intrinsic transverse momentum $\mathbf{p}_T$ which already yields reasonable magnitudes of the asymmetry. The predictions by [GGO03a] are shown in Fig. 6.17. One clearly sees that the absolute magnitude of the predictions is too large but the x- and z-behavior of the predictions is quite similar to the data. This can probably be explained by the fact that [GGO03a] used only a scalar coupling in the quark-diquark model to calculate the u-quark Sivers function. When applying the same model but calculating also a vector coupling, it is possible to obtain the u-quark and the d-quark Sivers function. This has been performed by [LM04] and [BSY04]. This results in a large u-quark Sivers function and a negative d-quark Sivers function of almost one order smaller magnitude. For the fragmentation process both groups used the parameterization of [KLC01]. The small differences in their predictions, as can be seen in Fig. 6.17 and Fig. 6.18, originate in a slightly different treatment of the couplings in their models.

One can see that these two predictions do almost agree with the measured π^+ asymmetries while they overestimate the π^- and π^0 asymmetries which can be explained by their quite smaller predictions for the d-quark Sivers function relative to the ones extracted in the previous section. Note that at least the predictions from [BSY04] use a different angular definition such that the comparison plots should be understood as a comparison of magnitudes but the overall sign of their predictions and the measured asymmetries differs.

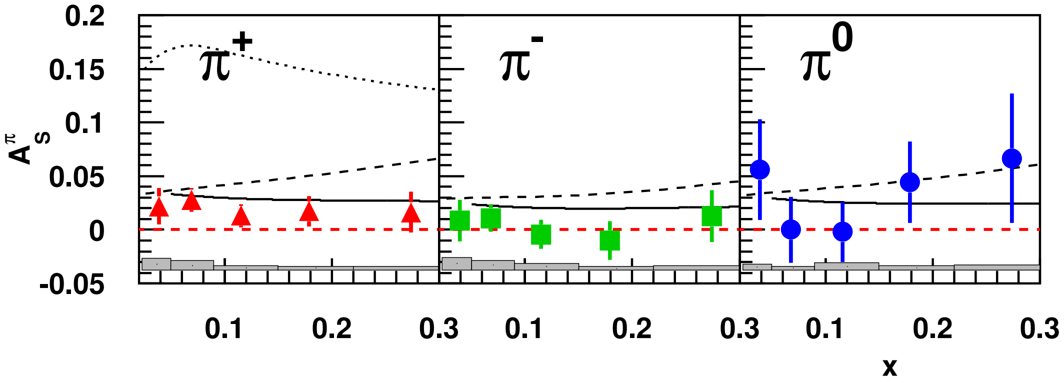

Figure 6.17: $P_{h\perp}/(zM)$-weighted Sivers type asymmetries vs. x compared to theory predictions. The dotted line represents the predictions from [GGO03a], the dashed lines are the predictions from [LM04] and the full lines those of [BSY04].

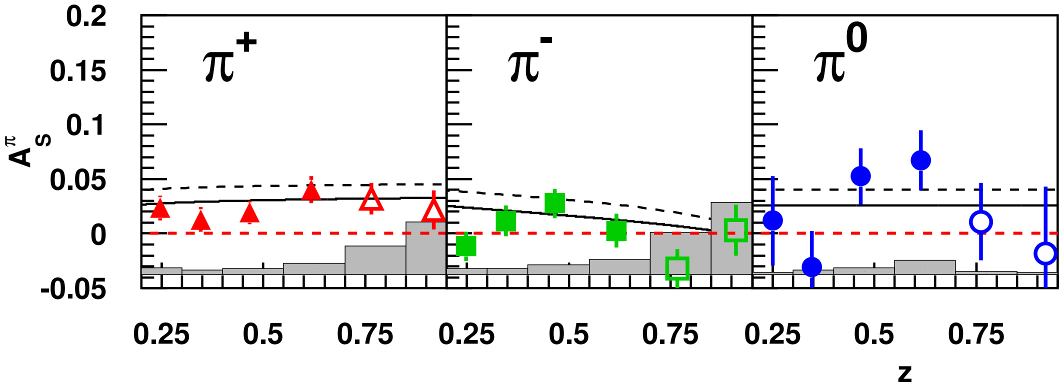

Figure 6.18: $P_{h\perp}/(zM)$-weighted Sivers type asymmetries vs. z compared to theory predictions. The dotted line represents the predictions from [GGO03a], the dashed lines are the predictions from [LM04] and the full lines those of [BSY04].

7

Extraction of distribution and fragmentation functions, outlook

The simple interpretations of the previous chapter do still depend on the applied assumptions and parameterizations. It is therefore favorable to extract the unknown distribution and fragmentation functions in an almost model independent way on the quark level. In the following section a formalism already applied in the extraction of the quark helicity distribution [Wen, Bec] is explained. This formalism is almost directly applicable for the extraction of the Sivers function but not for the extraction of the combination of transversity and Collins function since here it involves two unknown quantities. As a consequence at least another independent measurement of either of them is needed. Possible measurements at HERMES, other existing experiments and future experiments are addressed as an outlook.

7.1 Purity formalism

In the Sivers case the cross section ratios defining the asymmetries (equation 6.25 to 6.27) contain only unpolarized quantities as well in the denominator as partially also in the numerator. The unpolarized distribution function is already very well measured and parameterized. Also the unpolarized fragmentation functions for HERMES kinematics can be extracted. It is therefore straightforward to proceed in a similar way as in the extraction of the longitudinal quark polarizations [Wen, Bec] and to regroup the cross section ratios in an completely unpolarized part and the polarization dependent part. Multiplication with $1 = \frac{q(x)}{q(x)}$ gives for the Sivers asymmetries

$$
\begin{aligned}
A_S^h(\langle x\rangle, \langle z\rangle) &= \frac{\sum_q e_q^2 \int dx f_{1T}^{\perp,(1),q}(x) \int dz D_1^{q\to h}(z)}{\sum_q e_q^2 \int dx q(x) \int dz D_1^{q\to h}(z)} && (7.1)\\
&= \sum_q \underbrace{\frac{e_q^2 \int dx q(x) \int dz D_1^{q\to h}(z)}{\sum_q e_q^2 \int dx q(x) \int dz D_1^{q\to h}(z)}} \frac{f_{1T}^{\perp,(1),q}(x)}{q(x)} && (7.2)\\
&= \sum_q \qquad \mathcal{P}_h^q(x) \cdot \quad \frac{f_{1T}^{\perp,(1),q}(x)}{q(x)} \quad , && (7.3)
\end{aligned}
$$

where the so-called purity $\mathcal{P}_h^q(x)$ is the probability that a quark of type q has been struck when a hadron h is detected and $\frac{f_{1T}^{\perp}(x)}{q(x)}$ is the *Sivers polarization* in the nucleon. With the HERMES Monte Carlo it is possible to calculate these purities for each x-bin by taking parameterizations for $q(x)$ based on F_2 measurements. This gives linear equations of the measured asymmetries. At the moment only the $\pi^\pm$ and π^0 asymmetries are taken into account, but in the future, when a larger amount of statistics is analyzed, probably also kaon asymmetries can be taken. With only 3 asymmetries measured it is not possible to perform a complete flavor separation of the *Sivers polarizations*, one has to make assumptions on the quark sea. Assuming a SU(3) symmetric light quark sea in the Sivers function

$$
\begin{aligned}
&\frac{f_{1T}^{\perp,\bar u}(x)}{\bar u(x)} = \frac{f_{1T}^{\perp,\bar d}(x)}{\bar d(x)} = \frac{f_{1T}^{\perp,\bar s}(x)}{\bar s(x)} \quad = \\
&\frac{f_{1T}^{\perp,u_s}(x)}{u_s(x)} = \frac{f_{1T}^{\perp,d_s}(x)}{u_s(x)} = \frac{f_{1T}^{\perp,s}(x)}{s(x)} \qquad (7.4)
\end{aligned}
$$

leaves the three polarizations to solve the set of equations. The analysis of the flavor decomposition is ongoing by the HERMES group at the Tokyo Institute of Technology [Tan04], and will be presented soon.

The extraction of transverse quark polarizations $\delta q(x)/q(x)$ cannot be performed as the asymmetries (equation 6.10 to 6.12) contain two unknown functions, the transversity distribution and the Collins function. Therefore one has to rely on additional information. Parameterizations of the Collins function from other measurements as for example from BELLE data would be very helpful.

7.2 Further DIS measurements of transversity and Collins at HERMES

In addition to the single spin asymmetries presented here other observables connected to transversity are accessible at HERMES, but unfortunately they all rely on much more data as their particle yields are smaller.

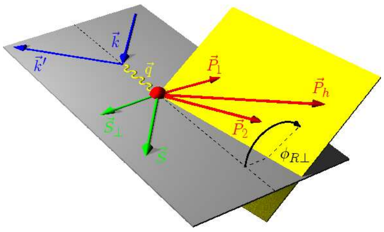

Figure 7.1: Definition of the azimuthal angles ϕ_R and ϕ_S

7.2.1 Interference fragmentation

The probably best candidate to be analyzed soon is the 2-hadron channel, where azimuthal asymmetries in the hadron decay plane around the virtual photon axis are measured. This was already proposed by [Jaf97] and denoted as interference fragmentation. It has the advantages that it does not include transverse momentum dependent fragmentation functions which implies that factorization is certain [Bac04].

This interference fragmentation function $H_{1,UT}^{\sphericalangle}(z, M_{\pi\pi}^2)$ is created by an interference of the two hadrons which can be created either in the s-wave p-wave channel or in a p-wave p-wave channel. The transverse cross section is [BR03]:

$$\frac{d^7\sigma_{UT}}{d\zeta dM_{\pi\pi}^2 d\phi_R dz dx dy d\phi_S} = \tag{7.5}$$

$$\sum_q \frac{2\alpha^2 e_q^2}{sM_{\pi\pi}^2} |\mathbf{S}_T||R|B(x,y)\sin(\phi_R+\phi_S)\sin\Theta\delta q\left[H_{1,UT}^{\sphericalangle q} + H_{1,LT}^{\sphericalangle q}\cos\Theta\right] \quad , \tag{7.6}$$

where $|R| = 1/2\sqrt{M_{\pi\pi}^2 - 4M_\pi^2}$, ζ is the momentum asymmetry between the two pions and Θ is the polar decay angle of one pion in the center of mass system with respect to the direction of the two-pion system in the target rest frame. The azimuthal angle ϕ_R is defined between the lepton scattering plane and the plane defined by the two hadrons as illustrated in Fig. 7.1. $H_{1,LT}^{\sphericalangle q}$ corresponds to fragmentation function in the pp-channel.

The invariant mass dependence of the sp-channel could be similar to that obtained in a low energy $\pi\pi$ scattering phase shift analysis [EM74] as displayed in Fig. 7.2.

A model calculation by [RJB02] results in the invariant mass dependence of the predicted asymmetries as displayed in Fig. 7.3. Instead of a clear sign change at the ρ mass, the different channels (s,p-wave) all contain a linear behavior versus the invariant mass. It will be interesting to see, which model is favored. HERMES is currently analyzing this two-pion channel, based on the high statistics obtained with the longitudinally polarized deuteron target. In the future, when enough data will be available, also the transversely polarized hydrogen data will be analyzed.

7.2.2 Vector mesons and Λ polarimetry

Another possibility to access transversity is by polarimetry of the final hadronic state if the produced hadron is either of spin 1/2 (Λ) or of spin 1 (vector mesons). The easiest

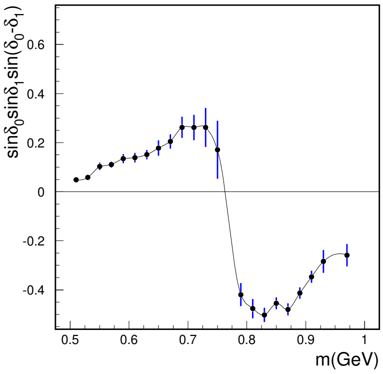

Figure 7.2: Phase shift factor $\sin\delta_0 \sin\delta_1 \sin(\delta_0 - \delta_1)$ versus the invariant mass of the 2 pions system.

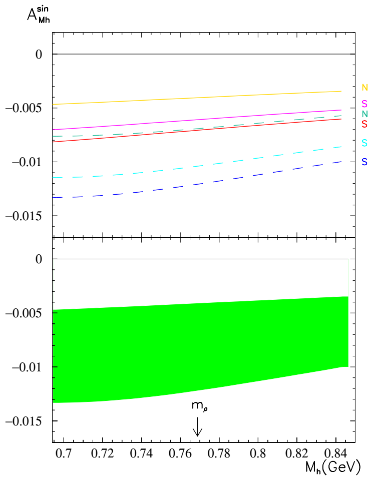

Figure 7.3: Invariant mass dependence of the two-pion asymmetries as predicted by [RJB02].

case would be to measure the double spin asymmetry produced with an unpolarized beam and a transversely polarized target and transverse polarization of the outgoing Λs [Art91, AM90]. This asymmetry contains a $\cos(\phi_S + \phi_{S_h})$ moment, where ϕ_{S_h} is the azimuthal angle of the transverse Λ polarization with respect to the lepton scattering plane. The great advantage of this cosine moment is that it contains the transversity distribution of quarks in the nucleon and a similar fragmentation function H_1^q which does not need the inclusion of intrinsic transverse momentum since it is only chiral-odd but naive time reversal even [BM98]. Therefore no convolution integrals over intrinsic transverse momenta are involved and factorization certainly holds. Unfortunately the amount of produced Λs at HERMES energies is rather limited, the ratio of semi-inclusive Λ events to DIS events is only 0.023% [Berb], such that one will need huge amounts of DIS events to measure these asymmetries. Another channel to access transversity, which is not so much suppressed is the analysis of vector mesons [Bac02]. Here the amount of fragmentation functions is huge due to the fact, that in a spin one hadron many more projections of the spins are possible. The easiest way to access transversity is by a fragmentation function $H_{1,LT}(z)$ which is similar to the Collins function in the pseudo-scalar meson case. As already mentioned before this would also be very interesting to test the Artru model presented earlier. Although here reasonable statistics can be expected, but the amount of non-resonant pseudo-scalar meson pairs will produce a large background.

7.3 Measurements in other experiments

The fact that several unknown distribution and fragmentation functions are involved in these single spin asymmetries, which cannot be mapped entirely by SIDIS experiments alone calls for a global analysis of these functions in whatever process they appear. I addition to polarized SIDIS also e^+e^- annihilation jet analysis, polarized hadroproduction of mesons and polarized Drell-Yan can shed light on them from different perspectives, although not all universality issues have been settled yet.

7.3.1 Existing experiments

COMPASS The COMPASS [Mal04] experiment uses the 160 GeV muon beam at CERN. The experiment is currently running with an either longitudinally or transversely polarized LiD solid state target. The target density thus is about eleven orders of magnitude higher than at HERMES although the deuteron nuclei contain a smaller average polarization than in a gas target and the lithium, which can be seen as a unpolarized α nucleus and a polarized deuteron nucleus, gives an additional dilution. Also the lepton currents are about ten orders of magnitude smaller than those at HERA, resulting in an only slightly increased rate of polarized DIS events.

As reported recently (e.g. [Web04, Fis04]) COMPASS has also released first measurements of Collins type asymmetries for charged pions. The magnitude seems to be smaller than for the HERMES proton data which can be understood by isospin symmetry between the proton and the neutron. Analysis of the Sivers type asymmetries is in progress. The Collins type asymmetries seem to be compatible with zero, the statistical uncertainties, however, are at present still very large. In the next years the statistics will be increased by a factor of four, such that COMPASS will contribute valuable information on the transverse spin asymmetries, especially in the deuteron case which is unlikely to be measured elsewhere in the near future.

CEBAF The Jefferson Lab currently operates a 6 GeV electron beam which runs at very high luminosity. Due to the low energy of the electrons most of the measurements are performed in a low Q^2, low W^2 region where nuclear resonances dominate and one merely accesses the deep inelastic region. Nevertheless non-zero azimuthal beam spin asymmetries have been reported [A$^+$03d] at CLAS in the deep inelastic regime. At present no transversely polarized target exists, but CLAS already ran with a longitudinally polarized solid state target. An upgrade of the accelerator to a maximal energy of 12 GeV will allow to increase the statistical precision for (SI)DIS.

BELLE As mentioned earlier it is necessary to obtain additional information on the Collins fragmentation function in order to extract the quark transversities. Especially the high luminosity $e^+e^- \rightarrow b\bar{b}$ production experiments investigating CP-violation of the B-meson decays can provide high precision fragmentation data. BELLE [A$^+$02a] uses the KEKB storage ring colliding 8 GeV electrons with 3.5 GeV positrons producing $b\bar{b}$ pairs on the Υ(4S) resonance, while 10% of the data is obtained off resonance. This data set can then be analyzed in order to study the azimuthal dependencies of pion pairs produced with transverse momentum relative to its jet axes, where the azimuthal angles are defined around the jet axes relative to the lepton-jet plane [HGPO$^+$03]. The cosine moment of the sum of these azimuthal angles is proportional to the product of the Collins functions $A \propto \cos(\phi_1+\phi_2)\cdot H_1^\perp(z_1)H_1^\perp(z_2)$. As a second analysis relevant to the general understanding of transversity from the SIDIS experiments also the product of the interference fragmentation functions discussed earlier in this chapter can be obtained by measuring the azimuthal dependencies around the common jet axis of the plane defined by $\pi^+\pi^-$ pairs.

RHIC-SPIN The two experiments PHENIX [A$^+$03c] and STAR [A$^+$03a] which are both located at the RHIC facility at BNL started also their spin physics program, which will mostly concentrate on the investigation of the quark and gluon helicity distributions $\Delta q(x), \Delta g(x)$ in the nucleon. Both experiments use the two polarized proton beams for their spin program. In addition to the helicity distributions also transversity and transverse momentum dependent distribution or fragmentation functions in hadroproduction can be accessed via azimuthal asymmetries. In the far future statistics may even be sufficient to analyze DY-pairs, which can give a direct access to the combination of quark and antiquark transversity when colliding transversely polarized protons.

7.3.2 Future experiments

While the previously presented experiments already produce results and more detailed information on transversity, the Sivers and Collins function and interference fragmentation is just a matter of months or years, the two last experiments to be discussed here won't even be build within this decade. They could therefore be seen as an outlook into the future of transversity measurements with high precision.

EIC EIC is planned to be a high luminosity **E**lectron **I**on **C**ollider, with the possibility to have both a polarized electron as well as a polarized proton beam. At present two competing realizations of this project are possible both including the combination of an already existing accelerator with a second accelerator yet to be built. One possibility, called the eRHIC solution would be to add an electron accelerator of up to 10 GeV energy to the existing RHIC facility with proton energies of $50 - 250$ GeV. The second possibility is to use the existing or by then upgraded electron beam at CEBAF and add a polarized proton beam at reasonable high energies. In both scenarios one or two interaction regions with nearly 4π detectors and a good lepton hadron identification are planned, such that one can expect a new generation of high precision, high luminosity polarized DIS experiments able to extract the polarized quark and gluon distribution functions. Also the measurement of generalized parton distributions can then be performed in a wider range than now.

PAX PAX is an experiment proposed for the already approved **H**igh **E**nergy antiproton **S**torage **R**ing at the GSI in Germany. The possibility to collide transversely polarized antiprotons with a transversely polarized fixed target would allow, at high enough luminosities, to directly measure transversity via DY processes. The fact that one is using antiprotons improves the situation largely, since then one is able to measure two valence quark transversities instead of a valence and a sea transversity in proton proton scattering. As all theoretical models agree that transversity is mostly valence quark dominated the resulting DY rates should be high enough to be measurable.

7.4 Summary

First transversely polarized single spin asymmetries accessing the Sivers function, the Collins function and transversity have been reported. Possible systematic uncertainties have been studied in Monte Carlo data and real data and were found to be negligible except for the contributions of exclusive vector mesons to the semi-inclusive pion data sample. The statistics of the measurements presented are still limited, but based on the observed asymmetries first conclusions on the magnitude of the Sivers functions of positively and negatively charged light quarks could be extracted. The nonzero values for the Sivers function could be related to quark densities at an average impact parameter, which is not coinciding with the center of the nucleon. Such a behavior was already proposed in a model including nonzero angular momentum of the quarks. Therefore one can possibly see a first effect of the angular momentum of the quarks.

Also valuable information on the Collins function and its disfavored to favored ratio could be obtained. This findings are quite unexpected but can be explained in simple string fragmentation models. Due to the fact that both, the Collins function and the transversity distribution are unknown objects, one could not yet obtain much information on transversity.

We are still standing at the beginning of the measurements of the functions mentioned, but our knowledge will increase rapidly in the near future. The hope to access the quark's orbital angular momentum and the prospects for transversity make it a subject worth further investigation.

A

Light cone variables

The metric tensor is defined as

$$g_{\mu\nu} = \begin{pmatrix} 1 & 0 & 0 & 0 \\ 0 & -1 & 0 & 0 \\ 0 & 0 & -1 & 0 \\ 0 & 0 & 0 & -1 \end{pmatrix} \quad , \tag{A.1}$$

where Greek indices are running from 0 to 3. Latin indices are used for three-vectors which are running from 1 to 3. The Einstein summation convention is applied where not specified otherwise.

Commonly the direction of the incoming leptons is taken as the z-axis. Therefore the light-cone coordinates are defined as

$$\left[P^-, P^+, \mathbf{P}^T\right] = \left[\frac{P^0 - P^3}{\sqrt{2}}, \frac{P^0 + P^3}{\sqrt{2}}, P^1, P^2\right] \quad , \tag{A.2}$$

where the transverse parts will be denoted with a subscript T and are running from 1 to 2.

The metric tensor becomes for light-cone variables

$$g_{\mu\nu} = \left(\begin{array}{cccc} 0 & 1 & 0 & 0 \\ 1 & 0 & 0 & 0 \\ 0 & 0 & -1 & 0 \\ 0 & 0 & 0 & -1 \end{array} \right) \quad , \tag{A.3}$$

giving for the product of two light-cone vectors

$$a_\mu b^\mu = a^+ b^- + a^- b^+ - \mathbf{a}_T \mathbf{b}_T \quad . \tag{A.4}$$

The light-cone description defines the so-called infinite momentum frame, in which the nucleon contains an almost infinite momentum. The nucleon can be seen as collection of almost free massless partons as the interaction with the virtual photon is localized to a region $\Delta x^+ \sim 1/Q$. In this frame the virtual photon with light-cone momentum $1/\sqrt{2}(-Q, Q, \mathbf{0}^T)$ interacts with a parton of light-cone momentum of $1/\sqrt{2}(Q, x^2 m_N^2/Q, \mathbf{p}^T)$, such that the scattered parton is moving in the x^- direction.

The Gell-Mann matrices are

$$\lambda^1 = \left(\begin{array}{ccc} 0 & 1 & 0 \\ 1 & 0 & 0 \\ 0 & 0 & 0 \end{array} \right) \quad \lambda^2 = \left(\begin{array}{ccc} 0 & -i & 0 \\ i & 0 & 0 \\ 0 & 0 & 0 \end{array} \right) \quad \lambda^3 = \left(\begin{array}{ccc} 1 & 0 & 0 \\ 0 & -1 & 0 \\ 0 & 0 & 0 \end{array} \right)$$

$$\lambda^4 = \left(\begin{array}{ccc} 0 & 0 & 1 \\ 0 & 0 & 0 \\ 1 & 0 & 0 \end{array} \right) \quad \lambda^5 = \left(\begin{array}{ccc} 0 & 0 & -i \\ 0 & 0 & 0 \\ i & 0 & 0 \end{array} \right) \quad \lambda^6 = \left(\begin{array}{ccc} 0 & 0 & 0 \\ 0 & 0 & 1 \\ 0 & 1 & 0 \end{array} \right)$$

$$\lambda^7 = \left(\begin{array}{ccc} 0 & 0 & 0 \\ 0 & 0 & -i \\ 0 & i & 0 \end{array} \right) \quad \lambda^8 = \tfrac{1}{\sqrt{3}} \left(\begin{array}{ccc} 1 & 0 & 0 \\ 0 & 1 & 0 \\ 0 & 0 & -2 \end{array} \right) \quad . \tag{A.5}$$

The Dirac matrices applied are in the Weyl or chiral representation:

$$\gamma^0 = \left(\begin{array}{cc} 0 & \mathbf{1} \\ \mathbf{1} & 0 \end{array} \right) \quad \gamma^i = \left(\begin{array}{cc} 0 & -\sigma^i \\ \sigma^i & 0 \end{array} \right) \quad \gamma^5 = \left(\begin{array}{cc} \mathbf{1} & 0 \\ 0 & -\mathbf{1} \end{array} \right) \quad , \tag{A.6}$$

where $\mathbf{1}$ corresponds to the 2×2 unit matrix and σ^i are the Dirac matrices. Since the regular Dirac matrices γ^μ behave as a Lorentz vector one can similarly define the γ^+ and γ^- matrices as combinations of the γ^0 and γ^3 matrices.

B

Parton distributions in impact parameter space

It is possible to relate the transverse momentum dependent parton distributions to parton distribution in impact parameter space. To see that, one starts with an operator O of the forward Compton scattering amplitude, for example the unpolarized quark distribution as in equation 2.27 after application of the delta function in +-momentum and Fourier transformation:

$$\langle P^+, \mathbf{P}'^T, S| \int \frac{d\xi^-}{4\pi} e^{ixP^+\xi^-} \bar{\psi}(0)\gamma^+\psi(\xi^-)|P^+, \mathbf{P}^T, S\rangle \quad . \tag{B.1}$$

In this formula one allows the initial and final transverse nucleon momenta to be different for the moment as it would be for generalized parton distributions. Following [Die04], one can now start with the same operator acting on the initial and final nucleon described in the basis of P^+ and the impact parameters $\mathbf{b}^T$ and $\mathbf{b}'^T$, which are the space coordinates corresponding to the transverse momenta:

$$\langle P^+, \mathbf{b}'^T, S|O|P^+, \mathbf{b}^T, S\rangle \quad . \tag{B.2}$$

Fourier transformation of the impact parameter leads back to the transverse momentum picture:

$$\frac{1}{(2\pi)^4} \int d^2\mathbf{P}'^T \int d^2\mathbf{P}^T e^{i\mathbf{P}'^T\cdot\mathbf{b}'^T} e^{-i\mathbf{P}^T\cdot\mathbf{b}^T} \langle P^+, \mathbf{P}'^T, S|O|P^+, \mathbf{P}^T, S\rangle \quad . \tag{B.3}$$

This can be reorganized in integrals over the sums and differences of the transverse momenta:

$$\frac{1}{(2\pi)^4}\frac{1}{4}\int d^2(\mathbf{P}'^T+\mathbf{P}^T)\int d^2(\mathbf{P}'^T-\mathbf{P}^T)e^{i(\mathbf{P}'^T-\mathbf{P}^T)\cdot\frac{(\mathbf{b}'^T+\mathbf{b}^T)}{2}}e^{-i(\mathbf{P}'^T+\mathbf{P}^T)\cdot\frac{(\mathbf{b}'^T-\mathbf{b}^T)}{2}}\cdot \\ \langle P^+,\mathbf{P}'^T,S|O|P^+,\mathbf{P}^T,S\rangle \quad . \tag{B.4}$$

Since the matrix element cannot depend on the sum of the transverse momenta as this would fail momentum conservation, the integral over the sums of the transverse momenta is just a Dirac delta function on the impact parameters:

$$\frac{1}{(2\pi)^2}\delta^2(\mathbf{b}'^T-\mathbf{b}^T)\int d^2(\mathbf{P}'^T-\mathbf{P}^T)e^{i(\mathbf{P}'^T-\mathbf{P}^T)\frac{(\mathbf{b}'^T+\mathbf{b}^T)}{2}}\langle P^+,\mathbf{P}'^T,S|O|P^+,\mathbf{P}^T,S\rangle \quad . \tag{B.5}$$

On has reached the expression of equation B.1 and can therefore identify the transverse momentum dependent forward amplitude with the Fourier transform of the same amplitude in impact parameter space. The parton distributions can accordingly be seen as parton densities of x and the impact parameter $\mathbf{b}$.

The difference of the transverse momenta $-t := (\mathbf{P}'^T - \mathbf{P}^T)$ describes the amount of transverse momentum the recoiling nucleon has gained in the Compton scattering process. For (semi-)inclusive DIS one has to take the imaginary part of the forward scattering amplitude, in which the transverse momenta of the initial and final state are the same, which can be expressed by a delta function in $-t$. A back transformation of equation B.5, applying this constraint as well as the delta function in the impact parameters $\delta^2(\mathbf{b}'^T - \mathbf{b}^T)$ returns the distribution function integrated over the complete impact parameter space:

$$\int d^2\mathbf{b}^T\langle P^+,\mathbf{b}^T,S|O|P^+,\mathbf{b}^T,S\rangle \quad . \tag{B.6}$$

This amplitude is now diagonal in the impact parameter and averages over the complete impact parameter space. As a consequence, if the parton distribution is not centered, one measures the parton distributions at a nonzero mean $\mathbf{b}^T$.

C

Statistical error calculations

C.1 Weighted asymmetries

Taking into account the fact that the statistical error of a w_i-weighted sum $X := \sum_i^N w_i$ is the sum of the squared weight $\delta X := \sqrt{\sum_i^N w_i^2}$, one can calculate the statistical error of the asymmetry

$$A_w^i(\phi, \phi_S) := \frac{\sum_i^{N^+} w_i - \sum_i^{N^-} w_i}{N^+ + N^-} \tag{C.1}$$

in each ϕ and ϕ_S bin to be:

$$\delta A_{w_i}(\phi, \phi_S) = \frac{\sqrt{(N^+ + N^-) \cdot \left(\sum_i^{N^+} w_i - \sum_i^{N^-} w_i\right)^2 + (N^+ + N^-)^2 \cdot \left(\sum_i^{N^+} w_i^2 + \sum_i^{N^-} w_i^2\right)}}{(N^+ + N^-)^2} \; . \tag{C.2}$$

A possible correlation between $N^\pm$ and $\sum_i^{N^\pm} w_i$ has not been taken into account. Formula C.2 further simplifies, when the weight is 1, i.e. one is calculating the unweighted asymmetries. Here the sums coincide with the event numbers and the statistical error becomes

$$\delta A(\phi, \phi_S) = \frac{2 \cdot \sqrt{N^+ N^- \left(N^+ + N^-\right)}}{\left(N^+ + N^-\right)^2} \quad . \tag{C.3}$$

The statistical errors of each azimuthal bin enter the fit procedure when calculating the basis $M_{ij} := f_j(\phi^i, \phi_S^i)/\delta A_i$ and the asymmetry $y_i := A_i/\delta A_i$. The basis or design matrix contains the M basis functions (i.e. a constant, $\sin(\phi - \phi_S)$,$\sin(\phi + \phi_S)$ and possible higher harmonics) evaluated at the bin centers of each of the N ϕ,ϕ_S bins. For the final results a basis of $M = 3$ and a $\phi \times \phi_S$ binning of $N = 8 \times 8 = 64$ was applied.

The corresponding system of equations $M_{ij}x_j = y_i$ can then be solved for the M moments x_j by solving the normal equation

$$\left(\mathbf{M}^T\mathbf{M}\right) x = \mathbf{M}^T y \quad . \tag{C.4}$$

This procedure is similar to a χ^2 minimization for the moments x_j:

$$\chi^2 = \sum_i^N \left(y_i - M_{ij}x_j\right)^2 \quad . \tag{C.5}$$

C.2 Background corrections

π^0 background In the case of the neutral pions which can only be detected via their decay products one will have combinatorial background. Since it is possible to determine its contribution one has to correct the statistical errors accordingly. As the statistical errors of the (diluted) π^0 asymmetries as well as those of the background are known, one can derive the statistical errors directly from equation 5.30.

$$\delta A_{corr}^{\sin(\phi\pm\phi_S)} = \frac{\sqrt{\left((N_{tot} \cdot \delta A_{meas})^2 + (N_{BG} \cdot \delta A_{BG})^2 + (A_{meas} - A_{BG})^2 \cdot (1 + \frac{N_{BG}}{N_\pi^0})^2\right)}}{N_\pi^0} . \tag{C.6}$$

D

Transverse momentum integrations

D.1 Direct $\mathbf{P}_{h\perp}$ integration

In a measurement the dependence on the intrinsic transverse momenta is not a priori known. Therefore the best possibility is to obtain a de-convoluted expression of the involved functions by weighting such that the convolution integrals can be separated in one containing the distribution function to be integrated over the intrinsic quark momentum in the nucleon and in one containing the fragmentation function integrated over the transverse momentum generated in the fragmentation process. For the transverse asymmetries treated in this work, this can be achieved by weighting with $\frac{\mathbf{P}_{h\perp}}{zM_h}$.

D.1.1 Collins function

The transverse momentum dependent part of the $\frac{\mathbf{P}_{h\perp}}{zM_h}$ weighted cross section is

$$\int d^2\mathbf{P}_{h\perp}\int d^2\mathbf{k}_T\int d^2\mathbf{p}_T \sin(\phi+\phi_S)\frac{|\mathbf{P}_{h\perp}|}{zM_h}\frac{\mathbf{k}_T\cdot\mathbf{P}_{h\perp}}{M_h|\mathbf{P}_{h\perp}|}\delta q(x,\mathbf{p}_T^2)H_1^\perp(z,\mathbf{k}_T^2)\delta^2(\mathbf{p}_T-\frac{\mathbf{P}_{h\perp}}{z}-\mathbf{k}_T)\quad . \tag{D.1}$$

Changing to spherical coordinates this expression becomes

$$\begin{aligned}&\int d|\mathbf{P}_{h\perp}||\mathbf{P}_{h\perp}|d\phi\int d^2\mathbf{k}_T\int d^2\mathbf{p}_T\sin(\phi+\phi_S)\tfrac{|\mathbf{P}_{h\perp}|}{zM_h}\tfrac{\mathbf{k}_T\cdot\mathbf{P}_{h\perp}}{M_h|\mathbf{P}_{h\perp}|}\\ &\delta q(x,\mathbf{p}_T^2)H_1^\perp(z,\mathbf{k}_T^2)\tfrac{z}{|\mathbf{P}_{h\perp}|}\delta(|\mathbf{p}_T|-\tfrac{|\mathbf{P}_{h\perp}|}{z}-|\mathbf{k}_T|)\delta(\phi-\phi_{pk})\quad ,\end{aligned} \tag{D.2}$$

Where ϕ_{pk} is the azimuthal angle created in this process. The integration over the absolute value of $\mathbf{P}_{h\perp}$ can now be performed, leaving

$$\int d\phi \int d^2\mathbf{k}_T \int d^2\mathbf{p}_T \sin(\phi+\phi_S)\frac{z^2}{M_h^2}\mathbf{k}_T\cdot(\mathbf{p}_T-\mathbf{k}_T)\delta q(x,\mathbf{p}_T^2)H_1^\perp(z,\mathbf{k}_T^2)\delta(\phi-\phi_{pk}) \quad . \tag{D.3}$$

Since the product of $\mathbf{k}_T$ with $\mathbf{p}_T$ is odd in both variables, either integration would yield zero and only the $\mathbf{k}_T^2$ survives. Regrouping the expressions one can identify the 0^{th} moment of the transversity distribution and the first moment of the Collins function:

$$\begin{aligned}-\int d\phi 2z^2\sin(\phi+\phi_S)\delta(\phi-\phi_{pk})\int d\mathbf{k}_T^2\delta q(x,\mathbf{p}_T^2)\int d\mathbf{p}_T^2\tfrac{\mathbf{k}_T^2}{2M_h^2}H_1^\perp(z,\mathbf{k}_T^2) = \\ -\int d\phi 2z^2\sin(\phi+\phi_S)\delta(\phi-\phi_{pk})\delta q(x)H_1^{\perp,(1)}(z) \quad .\end{aligned} \tag{D.4}$$

The still remaining integration of ϕ and the not mentioned ϕ_S integration would now also be performed in the weighted moment extraction method (as in equation 5.6) and yield an additional factor $2\pi^2$. Together with the additional factor 2 originating from the definition of the first moment it cancels out in an asymmetry with the factor $(2\pi)^2$ obtained in the integration over the (angular independent) unpolarized cross section. In the two fitting methods mentioned the modulations are fit and the remaining angular integration yields $(2\pi)^2$, which also cancels with the unpolarized cross section in the denominator. Therfore in the fit methods an additional factor 2 remains in the numerator.

D.1.2 Sivers function

Similarly the integration over the convolution integral for the Sivers function gives

$$\begin{aligned}\int d\phi \int d^2\mathbf{k}_T \int d^2\mathbf{p}_T \sin(\phi-\phi_S)\tfrac{z^2}{M_h^2}\mathbf{p}_T\cdot(\mathbf{p}_T-\mathbf{k}_T)f_{1T}^\perp(x,\mathbf{p}_T^2)D_1(z,\mathbf{k}_T^2)\delta(\phi-\phi_{pk}) = \\ -\int d\phi 2z^2\sin(\phi-\phi_S)\delta(\phi-\phi_{pk})f_{1T}^{\perp,(1)}(x)D_1(z) \quad .\end{aligned} \tag{D.5}$$

Also here the fit method produces an additional factor 2 in the asymmetry.

D.2 Gaussian ansatz

The deconvolution of the previous section does not work for the unweighted asymmetries since here application of the delta functional gives a factor $\frac{\mathbf{k}_T\cdot(\mathbf{p}_T-\mathbf{k}_T)}{M_h|\mathbf{p}_T-\mathbf{k}_T|}$ (in the Collins case) which cannot be further decoupled without any knowledge on the dependence on the intrinsic transverse momentum of the distribution and fragmentation functions. As an assumption the intrinsic transverse momentum dependence of the distribution and fragmentation functions is taken to be Gaussian with widths of $\langle \mathbf{k}_T^2 \rangle$ and $\langle \mathbf{p}_T^2 \rangle$, i.e.:

$$\begin{aligned}
\delta q(x, \mathbf{p}^T) &= \delta q(x) \frac{e^{\frac{-\mathbf{p}_T^2}{\langle \mathbf{p}_T^2 \rangle}}}{\pi \langle \mathbf{p}_T^2 \rangle} && \text{(D.6)}\\
f_{1T}^{\perp}(x, \mathbf{p}^T) &= f_{1T}^{\perp}(x) \frac{e^{\frac{-\mathbf{p}_T^2}{\langle \mathbf{p}_T^2 \rangle}}}{\pi \langle \mathbf{p}_T^2 \rangle} && \text{(D.7)}\\
D_1(z, \mathbf{k}^T) &= \delta D_1(z) \frac{e^{\frac{-\mathbf{k}_T^2}{\langle \mathbf{k}_T^2 \rangle}}}{\pi z^2 \langle \mathbf{k}_T^2 \rangle} && \text{(D.8)}\\
H_1^{\perp}(z, \mathbf{k}^T) &= H_1^{\perp}(z) \frac{e^{\frac{-\mathbf{k}_T^2}{\langle \mathbf{k}_T^2 \rangle}}}{\pi z^2 \langle \mathbf{k}_T^2 \rangle} && \text{(D.9)}\\
& && \text{(D.10)}
\end{aligned}$$

Sivers function With the Gaussian ansatz for the $\mathbf{p}_T$ dependence of the Sivers function one can get an analytic expression for the convolution integral $\mathcal{I}[f_{1T}^{\perp}(x, \mathbf{p}_T^2) D_1(z, \mathbf{k}_T^2) \frac{\mathbf{p}_T \cdot \mathbf{P}_{h\perp}}{M_N |P_{h\perp}|}]$.

This is necessary as for a MC generator the events will be thrown under the cross section for the given Sivers and Collins asymmetry. These cross sections only contain the already convoluted expressions without knowledge of the intrinsic transverse momenta. It is also of importance to derive an expression for the unweighted asymmetries.

The fully written convolution integral is, omitting the overall normalization for the Gaussian transverse momentum distribution of the distribution and fragmentation function $(\frac{1}{\pi^2 z^2 \langle \mathbf{p}_T^2 \rangle \cdot \langle \mathbf{k}_T^2 \rangle})$:

$$f_{1T}^{\perp}(x) \cdot D_1(z) \cdot \int \int d^2\mathbf{p}_T d^2\mathbf{k}_T \delta^{(2)}(\mathbf{p}_T - \frac{\mathbf{P}_{h\perp}}{z} - \mathbf{k}_T) \frac{\mathbf{p}_T \cdot \mathbf{P}_{h\perp}}{M_p |P_{h\perp}|} e^{\frac{\mathbf{p}_T^2}{\langle \mathbf{p}_T^2 \rangle}} e^{\frac{\mathbf{k}_T^2}{\langle \mathbf{k}_T^2 \rangle}} \quad . \tag{D.11}$$

Applying the delta function by integration over $d^2\mathbf{k}_T$ gives

$$f_{1T}^{\perp}(x) \cdot D_1(z) \cdot \int d^2\mathbf{p}_T \frac{\mathbf{p}_T \cdot \mathbf{P}_{h\perp}}{M_p |P_{h\perp}|} e^{\frac{\mathbf{p}_T^2}{\langle \mathbf{p}_T^2 \rangle}} e^{\frac{(\mathbf{p}_T - P_{h\perp}/z)^2}{\langle \mathbf{k}_T^2 \rangle}} \quad . \tag{D.12}$$

In order to integrate also over $\mathbf{p}_T$ one has to expand the exponent to a quadratic form of the intrinsic transverse momentum which yields:

$$\begin{aligned}
f_{1T}^{\perp}(x) \cdot D_1(z) \cdot \int d^2\mathbf{p}_T \frac{\mathbf{p}_T \cdot \mathbf{P}_{h\perp}}{M_p |P_{h\perp}|} \quad \exp\left[-(\tfrac{1}{\langle \mathbf{p}_T^2 \rangle} + \tfrac{1}{\langle \mathbf{k}_T^2 \rangle}) \left(\mathbf{p}_T - \tfrac{P_{h\perp}/z}{\langle \mathbf{k}_T^2 \rangle (\frac{1}{\langle \mathbf{p}_T \rangle^2} + \frac{1}{\langle \mathbf{k}_T^2 \rangle})} \right)^2 \right] \cdot \\
\cdot \exp\left[-\tfrac{P_{h\perp}^2}{z^2} \left(\tfrac{1}{\langle \mathbf{k}_T^2 \rangle + \langle \mathbf{p}_T^2 \rangle} \right) \right] \quad .
\end{aligned} \tag{D.13}$$

By the variable transformation $\mathbf{p}'_T = \left(\mathbf{p}_T - \frac{P_{h\perp}/z}{\langle \mathbf{k}_T^2 \rangle (\frac{1}{\langle \mathbf{p}_T \rangle^2} + \frac{1}{\langle \mathbf{k}_T^2 \rangle})} \right)$ one obtains another Gaussian. To perform the 2-dimensional integration one changes to Cartesian coordinates and calculates the scalar product for the new variable which will be hereafter called $\mathbf{p}_T$ again. The result is:

$$f_{1T}^{\perp}(x)\cdot D_1(z)\cdot \frac{\exp\left[-\frac{P_{h\perp}^2}{z^2}\left(\frac{1}{\langle \mathbf{k}_T^2\rangle+\langle \mathbf{p}_T^2\rangle}\right)\right]}{M_p|P_{h\perp}|}\cdot$$
$$\int d\mathbf{p}_{T,1}\int d\mathbf{p}_{T,2}\left((p_{T,1}+\frac{P_{h\perp,1}/z}{\langle \mathbf{k}_T^2\rangle(\frac{1}{\langle \mathbf{p}_T\rangle^2}+\frac{1}{\langle \mathbf{k}_T^2\rangle})})P_{h\perp,1}+(p_{T,2}+\frac{P_{h\perp,2}/z}{\langle \mathbf{k}_T^2\rangle(\frac{1}{\langle \mathbf{p}_T\rangle^2}+\frac{1}{\langle \mathbf{k}_T^2\rangle})})P_{h\perp,2}\right)$$
$$\cdot\exp\left[-(\tfrac{1}{\langle \mathbf{p}_T^2\rangle}+\tfrac{1}{\langle \mathbf{k}_T^2\rangle})\left(\mathbf{p}_T\right)^2\right] \tag{D.14}$$

The linear terms in $\mathbf{p}_T$ preceeding the Gaussian do not survive the integration as they are odd, and only the the constant terms remain. The two Gaussian integrals can now easily be solved giving $\pi(\frac{1}{\frac{1}{\langle \mathbf{p}_T^2\rangle}+\frac{1}{\langle \mathbf{k}_T^2\rangle}})$. Together with the normalization of the Gaussian transverse momentum dependences this gives:

$$f_{1T}^{\perp}(x)\cdot D_1(z)\cdot \frac{|P_{h\perp}|}{M_p\pi z^3}\frac{\langle \mathbf{p}_T^2\rangle}{\left(\langle \mathbf{k}_T^2\rangle+\langle \mathbf{p}_T^2\rangle\right)^2}\exp\left[-\frac{P_{h\perp}^2}{z^2}\left(\frac{1}{\langle \mathbf{k}_T^2\rangle+\langle \mathbf{p}_T^2\rangle}\right)\right]. \tag{D.15}$$

Collins function This ansatz for a Gaussian intrinsic transverse momentum dependence can also be applied for modeling the Collins fragmentation function. Here, the transverse momentum in question is that produced in the fragmentation process. The convolution $\mathcal{I}[\delta q(x,\mathbf{p}_T^2)H_1^{\perp}(z,\mathbf{k}_T^2)\frac{\mathbf{k}_T\cdot\mathbf{P}_{h\perp}}{M_\pi|P_{h\perp}|}]$ is similar and the same procedure can be applied here as well by interchanging $\mathbf{k}_T\leftrightarrow\mathbf{p}_T$ in the Gaussians and in the convolution. The integrations are therefore also interchanged, since now the $\mathbf{p}_T$ integration does not appear in the product with the transverse hadron momentum. As a consequence of this interchange one gets an additional minus sign coming from the delta function. As a result one obtains for the convolution integral

$$-\delta q(x)\cdot H_1^{\perp(1/2)}(z)\cdot\frac{|P_{h\perp}|}{M_\pi\pi z^3}\frac{\langle \mathbf{k}_T^2\rangle}{\left(\langle \mathbf{p}_T^2\rangle+\langle \mathbf{k}_T^2\rangle\right)}\exp\left[-\frac{P_{h\perp}^2}{z^2}\left(\frac{1}{\langle \mathbf{p}_T^2\rangle+\langle \mathbf{k}_T^2\rangle}\right)\right] \tag{D.16}$$

D.2.1 $\mathbf{P}_{h\perp}$ integration

Unweighted moments With these results for the convolution integrals it is only straightforward to carry out the $\mathbf{P}_h^{\perp}$ integrated moments which appear in the measured asymmetries. For the unweighted moments, the integration over the transverse hadron momentum and the azimuthal target angle for the Sivers case reads

$$\int d\phi_S\int dP_{h\perp}^2\sin(\phi-\phi_S)f_{1T}^{\perp}(x)\cdot D_1(z)\cdot\frac{|P_{h\perp}|}{M_p\pi z^3}\frac{\langle \mathbf{p}_T^2\rangle}{\left(\langle \mathbf{k}_T^2\rangle+\langle \mathbf{p}_T^2\rangle\right)^2}\cdot$$
$$\exp\left[-\frac{P_{h\perp}^2}{z^2}\left(\frac{1}{\langle \mathbf{k}_T^2\rangle+\langle \mathbf{p}_T^2\rangle}\right)\right]\quad. \tag{D.17}$$

Changing to polar coordinates it is possible to separate the angular part and the radial part just corresponds to a $P_{h\perp}^2$ weighted Gaussian, which can be solved by applying partial derivatives as $P_{h\perp}^2 e^{-cP_{h\perp}^2} = -\frac{\partial}{\partial c} e^{-cP_{h\perp}^2}$. Interchanging the integration and the derivative, the Gaussian can be solved, and the still ϕ dependent result is

$$\frac{\sqrt{\pi}}{4M_p} \frac{\langle \mathbf{p}_T^2 \rangle}{\sqrt{\langle \mathbf{k}_T^2 \rangle + \langle \mathbf{p}_T^2 \rangle}} \cdot f_{1T}^{\perp}(x) \cdot D_1(z) \cdot \int d\phi_S \int d\phi \quad \sin(\phi - \phi_S). \tag{D.18}$$

Bearing in mind, that this moment is accompanied by a $\sin(\phi - \phi_S)$ modulation, the integration of the ϕ dependency can only be performed after substitution of $\phi_S' = \phi - \phi_S$. On can immediately see, that without any additional $\sin(\phi - \phi_S)$ weighting, the remaining integrals would give zero. Using the relation for Gaussian distributions $\langle |\mathbf{k}_T| \rangle^2 = \pi \langle \mathbf{k}_T^2 \rangle / 4$ one can convert equation D.18 into

$$\frac{2}{\sqrt{1 + \frac{\langle \mathbf{k}_T^2 \rangle}{\langle \mathbf{p}_T^2 \rangle}}} \cdot f_{1T}^{\perp,(1/2)}(x) \cdot D_1(z) \cdot \int d\phi_S \int d\phi \quad \sin(\phi - \phi_S) \quad , \tag{D.19}$$

absorbing the mean $\mathbf{p}_T$ and the pre-factors into the 1/2 moment of the Sivers function.

The similar calculations can also be performed for the Collins case, giving:

$$-\frac{2}{\sqrt{1 + \frac{\langle \mathbf{p}_T^2 \rangle}{\langle \mathbf{k}_T^2 \rangle}}} \cdot \delta q(x) \cdot H_1^{\perp,(1/2)}(z) \cdot \int d\phi_S \int d\phi \quad \sin(\phi - \phi_S). \tag{D.20}$$

$\frac{\mathbf{P}_h^{\perp}}{zM}$weighted moments The same procedure can be also performed for the $\frac{\mathbf{P}_h^{\perp}}{zM}$weighted moments in conjunction with the Gaussian transverse momentum dependence. Here the integrals over the transverse hadron momentum are already quadratic and one can perform the integration in Cartesian coordinates after applying the same partial derivative. One gets after absorption into the (1) moments:

$$2 f_{1T}^{\perp,(1)}(x) \cdot D_1(z) \cdot \int d\phi_S \int d\phi \quad \sin(\phi - \phi_S) \quad , \tag{D.21}$$

and

$$-2\delta q(x) \cdot H_1^{\perp,(1)}(z) \cdot \int d\phi_S \int d\phi \quad \sin(\phi - \phi_S). \tag{D.22}$$

D.2.2 A skewed Gaussian ansatz for a Monte Carlo generator

After realizing that the normal Gaussian ansatz for the $\mathbf{p}_T$ dependence of the Sivers function $f_{1T}^{\perp}(x, \mathbf{p}_T^2)$ generally fails the positivity constraint for large intrinsic transverse momenta

$$f_{1T}^{\perp(1/2)}(x, \mathbf{p}_T) \leq 1/2 f_1(x, \mathbf{p}_T) = 1/2 f_1(x) \frac{e^{-\frac{\mathbf{p}_T^2}{\langle \mathbf{p}_T^2 \rangle}}}{\pi \langle \mathbf{p}_T^2 \rangle} \quad , \tag{D.23}$$

an ansatz was taken, which just skews the previously mentioned Gaussian $\mathbf{p}_T$ distribution:

$$f_{1T}^{\perp}(x, \mathbf{p}_T) = f_{1T}^{\perp}(x)(1 + C) \frac{e^{-\frac{(1+C)\mathbf{p}_T^2}{\langle \mathbf{p}_T^2 \rangle}}}{\pi \langle \mathbf{p}_T^2 \rangle} \quad , \tag{D.24}$$

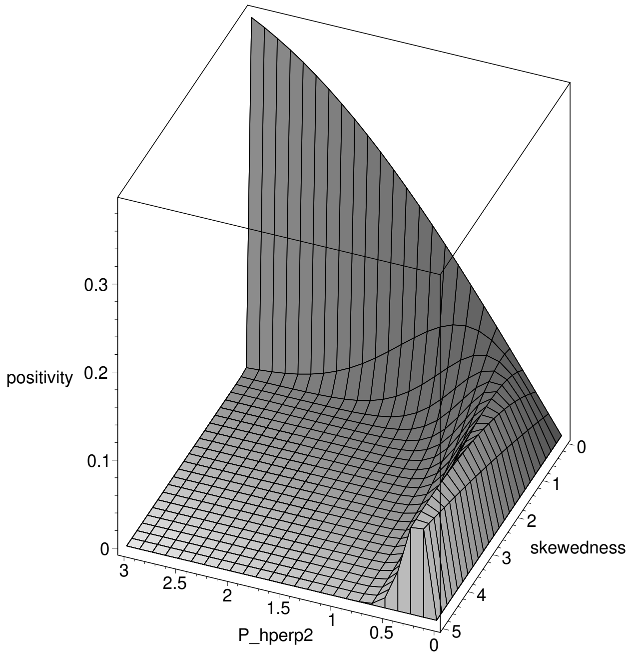

Figure D.1: Positivity value $|\mathbf{p}_T|(1+C)\cdot e^{\frac{-C\mathbf{p}_T^2}{\langle\mathbf{p}_T^2\rangle}}$ for various Skewdnesses C vs. $\mathbf{p}_T^2$ (denoted as P_hperp2 in the figure) in arbitrary units.

where C is an arbitrary skewing parameter. Using this new parameterization the positivity limit becomes

$$f_{1T}^{\perp,(1/2)}(x,\mathbf{p}_T) = f_{1T}^{\perp}(x)\frac{|\mathbf{p}_T|(1+C)}{2M_P}\frac{e^{-\frac{(1+C)\mathbf{p}_T^2}{\langle\mathbf{p}_T^2\rangle}}}{\pi\langle\mathbf{p}_T^2\rangle} \leq 1/2 f_1(x)\frac{e^{\frac{\mathbf{p}_T^2}{\langle\mathbf{p}_T^2\rangle}}}{\pi\langle\mathbf{p}_T^2\rangle} \quad , \tag{D.25}$$

and the previous Gaussian distribution can be divided out. This leaves a positivity limit which can be fulfilled for a reasonable choice of $f_{1T}^{\perp}(x)$ and C, when generating MC events. For the $\mathbf{p}_T$ dependent part together with the pre-factors this is illustrated in Fig. D.1. It can be seen, that already for small skewedness parameters C the function is bound for a large transverse momentum range. It shows also, that large values of this parameter should not be used, as it will immediately limit the transverse momentum range of the intrinsic momentum dependent functions to quite unphysical values; in the limit of an infinite value the distribution corresponds to that of a Dirac delta function. Obviously even such a Gaussian distribution will eventually, for large transverse momenta, create a transversely polarized cross section larger than the unpolarized one. This is of course not allowed by positivity, but one can restrict the transverse momenta to a range, which is not as small as without skewing the transverse momentum distribution.

E

Tables

E_h/GeV	$\Delta\phi$	$\Delta\phi_S$	$\Delta(\phi+\phi_S)$	$\Delta(\phi-\phi_S)$	ΔE_h	Δz	$\Delta P_{h\perp}$
2.599	0.157 ± 0.006	0.015 ± 0.006	0.157 ± 0.006	0.158 ± 0.006	0.047 ± 0.006	0.028 ± 0.006	0.044 ± 0.006
3.545	0.172 ± 0.004	0.015 ± 0.004	0.173 ± 0.004	0.172 ± 0.004	0.063 ± 0.004	0.026 ± 0.004	0.043 ± 0.004
4.504	0.174 ± 0.003	0.015 ± 0.003	0.174 ± 0.003	0.173 ± 0.003	0.078 ± 0.003	0.026 ± 0.003	0.047 ± 0.003
5.478	0.183 ± 0.004	0.016 ± 0.004	0.183 ± 0.004	0.183 ± 0.004	0.093 ± 0.004	0.027 ± 0.004	0.051 ± 0.004
6.474	0.192 ± 0.004	0.015 ± 0.004	0.192 ± 0.004	0.192 ± 0.004	0.109 ± 0.004	0.029 ± 0.004	0.057 ± 0.004
7.470	0.197 ± 0.005	0.015 ± 0.005	0.198 ± 0.005	0.197 ± 0.005	0.124 ± 0.005	0.030 ± 0.005	0.060 ± 0.005
8.463	0.199 ± 0.006	0.016 ± 0.006	0.200 ± 0.006	0.199 ± 0.006	0.141 ± 0.006	0.031 ± 0.006	0.065 ± 0.006
9.451	0.194 ± 0.008	0.015 ± 0.008	0.195 ± 0.008	0.194 ± 0.008	0.157 ± 0.008	0.032 ± 0.008	0.068 ± 0.008
10.441	0.206 ± 0.011	0.015 ± 0.011	0.206 ± 0.011	0.206 ± 0.011	0.172 ± 0.011	0.034 ± 0.011	0.068 ± 0.011
11.442	0.199 ± 0.016	0.016 ± 0.016	0.198 ± 0.016	0.198 ± 0.016	0.184 ± 0.016	0.033 ± 0.016	0.072 ± 0.016
12.439	0.201 ± 0.023	0.016 ± 0.023	0.202 ± 0.023	0.201 ± 0.023	0.198 ± 0.023	0.037 ± 0.023	0.076 ± 0.023
13.432	0.182 ± 0.033	0.016 ± 0.033	0.176 ± 0.033	0.182 ± 0.033	0.210 ± 0.033	0.037 ± 0.033	0.076 ± 0.033
14.437	0.163 ± 0.054	0.016 ± 0.054	0.166 ± 0.054	0.161 ± 0.054	0.245 ± 0.054	0.041 ± 0.054	0.065 ± 0.054

E_h/GeV	ΔE_e	Δx_B	$\Delta\theta_\gamma$	Δy	$\Delta\theta_{\gamma,had}$	$\Delta\theta_h$	$\Delta\phi_h$	$\Delta\theta_e$	$\Delta\phi_e$
2.599	0.408 ± 0.006	0.025 ± 0.006	0.020 ± 0.006	0.027 ± 0.006	0.018 ± 0.006	0.003 ± 0.006	0.021 ± 0.006	0.018 ± 0.006	0.007 ± 0.006
3.545	0.355 ± 0.004	0.022 ± 0.004	0.017 ± 0.004	0.028 ± 0.004	0.012 ± 0.004	0.002 ± 0.004	0.016 ± 0.004	0.012 ± 0.004	0.007 ± 0.004
4.504	0.318 ± 0.003	0.022 ± 0.003	0.016 ± 0.003	0.029 ± 0.003	0.011 ± 0.003	0.002 ± 0.003	0.014 ± 0.003	0.011 ± 0.003	0.007 ± 0.003
5.478	0.311 ± 0.004	0.023 ± 0.004	0.015 ± 0.004	0.029 ± 0.004	0.010 ± 0.004	0.002 ± 0.004	0.013 ± 0.004	0.010 ± 0.004	0.007 ± 0.004
6.474	0.308 ± 0.004	0.023 ± 0.004	0.015 ± 0.004	0.029 ± 0.004	0.010 ± 0.004	0.001 ± 0.004	0.011 ± 0.004	0.010 ± 0.004	0.007 ± 0.004
7.470	0.303 ± 0.005	0.023 ± 0.005	0.014 ± 0.005	0.030 ± 0.005	0.010 ± 0.005	0.001 ± 0.005	0.010 ± 0.005	0.010 ± 0.005	0.007 ± 0.005
8.463	0.298 ± 0.006	0.023 ± 0.006	0.015 ± 0.006	0.029 ± 0.006	0.010 ± 0.006	0.001 ± 0.006	0.010 ± 0.006	0.010 ± 0.006	0.007 ± 0.006
9.451	0.289 ± 0.008	0.023 ± 0.008	0.014 ± 0.008	0.030 ± 0.008	0.010 ± 0.008	0.001 ± 0.008	0.010 ± 0.008	0.010 ± 0.008	0.007 ± 0.008
10.441	0.276 ± 0.011	0.024 ± 0.011	0.014 ± 0.011	0.031 ± 0.011	0.010 ± 0.011	0.001 ± 0.011	0.008 ± 0.011	0.010 ± 0.011	0.007 ± 0.011
11.442	0.263 ± 0.016	0.024 ± 0.016	0.014 ± 0.016	0.031 ± 0.016	0.010 ± 0.016	0.001 ± 0.016	0.009 ± 0.016	0.010 ± 0.016	0.008 ± 0.016
12.439	0.246 ± 0.023	0.027 ± 0.023	0.014 ± 0.023	0.036 ± 0.023	0.011 ± 0.023	0.001 ± 0.023	0.008 ± 0.023	0.011 ± 0.023	0.008 ± 0.023
13.432	0.235 ± 0.033	0.023 ± 0.033	0.012 ± 0.033	0.032 ± 0.033	0.008 ± 0.033	0.001 ± 0.033	0.011 ± 0.033	0.008 ± 0.033	0.009 ± 0.033
14.437	0.221 ± 0.054	0.029 ± 0.054	0.015 ± 0.054	0.036 ± 0.054	0.012 ± 0.054	0.001 ± 0.054	0.008 ± 0.054	0.012 ± 0.054	0.009 ± 0.054

Table E.1: Resolutions in the kinematic variables for π^+ after application of the target magnet correction.

E_h/GeV	$\Delta\phi$	$\Delta\phi_S$	$\Delta(\phi+\phi_S)$	$\Delta(\phi-\phi_S)$	ΔE_h	Δz	$\Delta P_{h\perp}$
2.616	0.150 ± 0.008	0.015 ± 0.008	0.151 ± 0.008	0.150 ± 0.008	0.044 ± 0.008	0.025 ± 0.008	0.041 ± 0.008
3.553	0.158 ± 0.005	0.015 ± 0.005	0.159 ± 0.005	0.159 ± 0.005	0.061 ± 0.005	0.024 ± 0.005	0.039 ± 0.005
4.508	0.155 ± 0.004	0.015 ± 0.004	0.156 ± 0.004	0.155 ± 0.004	0.076 ± 0.004	0.023 ± 0.004	0.041 ± 0.004
5.481	0.168 ± 0.004	0.015 ± 0.004	0.168 ± 0.004	0.168 ± 0.004	0.093 ± 0.004	0.025 ± 0.004	0.048 ± 0.004
6.474	0.176 ± 0.005	0.015 ± 0.005	0.176 ± 0.005	0.175 ± 0.005	0.108 ± 0.005	0.027 ± 0.005	0.053 ± 0.005
7.467	0.179 ± 0.006	0.015 ± 0.006	0.180 ± 0.006	0.180 ± 0.006	0.124 ± 0.006	0.028 ± 0.006	0.056 ± 0.006
8.468	0.181 ± 0.007	0.015 ± 0.007	0.181 ± 0.007	0.180 ± 0.007	0.140 ± 0.007	0.029 ± 0.007	0.061 ± 0.007
9.458	0.178 ± 0.009	0.016 ± 0.009	0.179 ± 0.009	0.178 ± 0.009	0.155 ± 0.009	0.030 ± 0.009	0.063 ± 0.009
10.446	0.188 ± 0.012	0.016 ± 0.012	0.189 ± 0.012	0.187 ± 0.012	0.172 ± 0.012	0.032 ± 0.012	0.064 ± 0.012
11.447	0.176 ± 0.018	0.015 ± 0.018	0.179 ± 0.018	0.175 ± 0.018	0.185 ± 0.018	0.032 ± 0.018	0.069 ± 0.018
12.433	0.178 ± 0.025	0.016 ± 0.025	0.183 ± 0.025	0.174 ± 0.025	0.206 ± 0.025	0.032 ± 0.025	0.067 ± 0.025
13.446	0.152 ± 0.037	0.016 ± 0.037	0.153 ± 0.037	0.151 ± 0.037	0.211 ± 0.037	0.032 ± 0.037	0.066 ± 0.037
14.388	0.151 ± 0.059	0.016 ± 0.059	0.153 ± 0.059	0.151 ± 0.059	0.214 ± 0.059	0.029 ± 0.059	0.063 ± 0.059

E_h/GeV	ΔE_e	Δx_B	$\Delta\theta_\gamma$	Δy	$\Delta\theta_{\gamma,had}$	$\Delta\theta_h$	$\Delta\phi_h$	$\Delta\theta_e$	$\Delta\phi_e$
2.616	0.400 ± 0.008	0.023 ± 0.008	0.018 ± 0.008	0.026 ± 0.008	0.016 ± 0.008	0.002 ± 0.008	0.021 ± 0.008	0.016 ± 0.008	0.007 ± 0.008
3.553	0.346 ± 0.005	0.021 ± 0.005	0.015 ± 0.005	0.027 ± 0.005	0.011 ± 0.005	0.002 ± 0.005	0.017 ± 0.005	0.011 ± 0.005	0.007 ± 0.005
4.508	0.311 ± 0.004	0.020 ± 0.004	0.014 ± 0.004	0.027 ± 0.004	0.009 ± 0.004	0.002 ± 0.004	0.014 ± 0.004	0.009 ± 0.004	0.007 ± 0.004
5.481	0.304 ± 0.004	0.021 ± 0.004	0.014 ± 0.004	0.028 ± 0.004	0.009 ± 0.004	0.001 ± 0.004	0.013 ± 0.004	0.009 ± 0.004	0.007 ± 0.004
6.474	0.299 ± 0.005	0.021 ± 0.005	0.014 ± 0.005	0.028 ± 0.005	0.009 ± 0.005	0.001 ± 0.005	0.012 ± 0.005	0.009 ± 0.005	0.007 ± 0.005
7.467	0.295 ± 0.006	0.020 ± 0.006	0.013 ± 0.006	0.028 ± 0.006	0.009 ± 0.006	0.001 ± 0.006	0.010 ± 0.006	0.009 ± 0.006	0.007 ± 0.006
8.468	0.286 ± 0.007	0.021 ± 0.007	0.013 ± 0.007	0.028 ± 0.007	0.009 ± 0.007	0.001 ± 0.007	0.010 ± 0.007	0.009 ± 0.007	0.007 ± 0.007
9.458	0.284 ± 0.009	0.021 ± 0.009	0.013 ± 0.009	0.028 ± 0.009	0.009 ± 0.009	0.001 ± 0.009	0.009 ± 0.009	0.009 ± 0.009	0.007 ± 0.009
10.446	0.272 ± 0.012	0.021 ± 0.012	0.012 ± 0.012	0.028 ± 0.012	0.009 ± 0.012	0.001 ± 0.012	0.009 ± 0.012	0.009 ± 0.012	0.008 ± 0.012
11.447	0.256 ± 0.018	0.022 ± 0.018	0.012 ± 0.018	0.030 ± 0.018	0.009 ± 0.018	0.001 ± 0.018	0.010 ± 0.018	0.009 ± 0.018	0.008 ± 0.018
12.433	0.240 ± 0.025	0.020 ± 0.025	0.010 ± 0.025	0.029 ± 0.025	0.008 ± 0.025	0.001 ± 0.025	0.011 ± 0.025	0.008 ± 0.025	0.008 ± 0.025
13.446	0.236 ± 0.037	0.020 ± 0.037	0.012 ± 0.037	0.030 ± 0.037	0.008 ± 0.037	0.001 ± 0.037	0.009 ± 0.037	0.008 ± 0.037	0.008 ± 0.037
14.388	0.241 ± 0.059	0.016 ± 0.059	0.011 ± 0.059	0.032 ± 0.059	0.008 ± 0.059	0.001 ± 0.059	0.015 ± 0.059	0.008 ± 0.059	0.010 ± 0.059

Table E.2: Resolutions in the kinematic variables for π^-after application of the target magnet correction.

pion type	vm type	xbin 1	xbin 2	xbin 3	xbin 4	xbin 5	all xbins
π^+	EXCL.	0.063	0.060	0.037	0.024	0.016	0.048
π^+	ρ^0 SIDIS	0.108	0.101	0.098	0.096	0.093	0.111
π^+	ρ^+ SIDIS	0.104	0.104	0.102	0.098	0.102	0.115
π^+	ω^0 SIDIS	0.037	0.041	0.042	0.041	0.042	0.042
π^-	EXCL.	0.072	0.071	0.052	0.036	0.023	0.060
π^-	ρ^0 SIDIS	0.117	0.117	0.123	0.127	0.129	0.137
π^-	ρ^- SIDIS	0.095	0.094	0.090	0.088	0.095	0.094
π^-	ω^0 SIDIS	0.043	0.053	0.049	0.055	0.056	0.053
π^0	EXCL.	0.023	0.026	0.021	0.020	0.008	0.022

Table E.3: Dilutions of exclusive and semi-inclusive vector mesons in the pion data sample for the separate x bins and the combined SIDIS range (all bins).

pion type	vm type	zbin 1	zbin 2	zbin 3	zbin 4	zbin 5	zbin 6	all zbins
π^+	EXCL.	0.032	0.039	0.057	0.111	0.287	0.478	0.067
π^+	ρ^0 SIDIS	0.123	0.103	0.078	0.047	0.024	0.003	0.106
π^+	ρ^+ SIDIS	0.123	0.108	0.081	0.052	0.024	0.006	0.108
π^+	ω^0 SIDIS	0.064	0.037	0.016	0.005	0.001	0.000	0.039
π^-	EXCL.	0.040	0.049	0.072	0.148	0.367	0.578	0.082
π^-	ρ^0 SIDIS	0.144	0.121	0.098	0.059	0.023	0.005	0.129
π^-	ρ^- SIDIS	0.112	0.093	0.074	0.046	0.022	0.002	0.097
π^-	ω^0 SIDIS	0.076	0.047	0.021	0.007	0.001	0.000	0.050
π^0	EXCL.	0.014	0.021	0.031	0.052	0.051	0.100	0.023

Table E.4: Dilutions of exclusive and semi-inclusive vector mesons in the pion data sample for the separate z bins and the combined range (all bins).

transfer	rho asymmetry type	xbin 1	xbin 2	xbin 3	xbin 4	xbin 5
$\rho^0 \rightarrow \pi^+$	Sivers	0.176	0.161	0.130	0.197	0.270
	Collins	-0.371	-0.367	-0.387	-0.377	-0.388
$\rho^0 \rightarrow \pi^-$	Sivers	0.196	0.194	0.139	0.134	0.245
	Collins	-0.392	-0.404	-0.381	-0.406	-0.398
$\omega^0 \rightarrow \pi^0$	Sivers	0.127	0.094	0.032	0.131	0.178
	Collins	0.321	0.359	0.368	0.407	0.289

Table E.5: Asymmetry transfer values from vector mesons to their decay pions for the separate x bins for a Collins pion asymmetry for generated Sivers and Collins vector meson asymmetries.

transfer	rho asymmetry type	xbin 1	xbin 2	xbin 3	xbin 4	xbin 5
$\rho^0 \rightarrow \pi^+$	Sivers	0.476	0.476	0.453	0.356	0.413
	Collins	-0.239	-0.262	-0.227	-0.202	-0.288
$\rho^0 \rightarrow \pi^-$	Sivers	0.433	0.432	0.460	0.414	0.354
	Collins	-0.225	-0.249	-0.243	-0.140	-0.200
$\omega^0 \rightarrow \pi^0$	Sivers	0.334	0.409	0.472	0.320	0.391
	Collins	0.164	0.131	0.218	0.124	0.350

Table E.6: Asymmetry transfer values from vector mesons to its decay pions for the separate x bins for a Sivers pion asymmetry for generated Sivers and Collins vector meson asymmetries.

transfer	asymmetry type	zbin 1	zbin 2	zbin 3	zbin 4	zbin 5	zbin6
$\rho^0 \rightarrow \pi^+$	Sivers	0.174	0.164	0.139	0.197	0.205	0.192
	Collins	-0.364	-0.380	-0.352	-0.370	-0.448	-0.496
$\rho^0 \rightarrow \pi^-$	Sivers	0.224	0.136	0.131	0.169	0.152	0.102
	Collins	-0.378	-0.380	-0.369	-0.396	-0.409	-0.433
$\omega^0 \rightarrow \pi^0$	Sivers	0.104	0.157	0.092	-0.021	0.072	0.065
	Collins	0.360	0.437	0.334	0.241	0.240	0.217

Table E.7: Asymmetry transfer values from vector mesons to its decay pions for the separate z binsfor a Collins pion asymmetry for generated Sivers and Collins vector meson asymmetries.

transfer	asymmetry type	zbin 1	zbin 2	zbin 3	zbin 4	zbin 5	zbin6
$\rho^0 \rightarrow \pi^+$	Sivers	0.410	0.351	0.361	0.435	0.457	0.493
	Collins	-0.218	-0.172	-0.181	-0.268	-0.189	-0.168
$\rho^0 \rightarrow \pi^-$	Sivers	0.344	0.357	0.386	0.423	0.459	0.453
	Collins	-0.197	-0.172	-0.170	-0.213	-0.188	-0.095
$\omega^0 \rightarrow \pi^0$	Sivers	0.403	0.343	0.410	0.445	0.021	0.019
	Collins	0.222	0.123	0.205	0.133	-0.210	-0.190

Table E.8: Asymmetry transfer values from vector mesons to its decay pions for the separate z binsfor a Sivers pion asymmetry for generated Sivers and Collins vector meson asymmetries.

	run $\leq$ 2710		run $\geq$ 2710	
	$A_{UT}^{\sin(\phi-\phi_S)}$	$A_{UT}^{\sin(\phi+\phi_S)}$	$A_{UT}^{\sin(\phi-\phi_S)}$	$A_{UT}^{\sin(\phi+\phi_S)}$
pi^+	0.011 ± 0.015	0.073 ± 0.023	0.046 ± 0.010	0.022 ± 0.017
pi^-	0.008 ± 0.017	-0.076 ± 0.028	0.008 ± 0.013	-0.058 ± 0.020
pi^0	0.042 ± 0.030	-0.012 ± 0.047	0.042 ± 0.020	-0.023 ± 0.032

Table E.9: Sivers and Collins asymmetries for the two run ranges before and after run 2710. The π^0 results have not been background corrected.

variable	xbin 1	xbin 2	xbin 3	xbin 4	xbin 5	all xbins
$\langle x \rangle$	0.039	0.069	0.115	0.179	0.274	0.101
$\langle y \rangle$	0.659	0.529	0.471	0.447	0.431	0.532
$\langle z \rangle$	0.336	0.357	0.373	0.376	0.375	0.361
$\langle P_{h\perp}/\mathrm{GeV} \rangle$	0.499	0.418	0.378	0.358	0.353	0.411
$\langle Q^2/\mathrm{GeV}^2 \rangle$	1.31	1.84	2.76	4.07	6.06	2.47

Table E.10: Mean values of the kinematic variables $x, y, z, P_{h\perp}$ and Q^2 in each of the kinematic x-bins and in the whole semi-inclusive range for π^+.

F

Additional plots

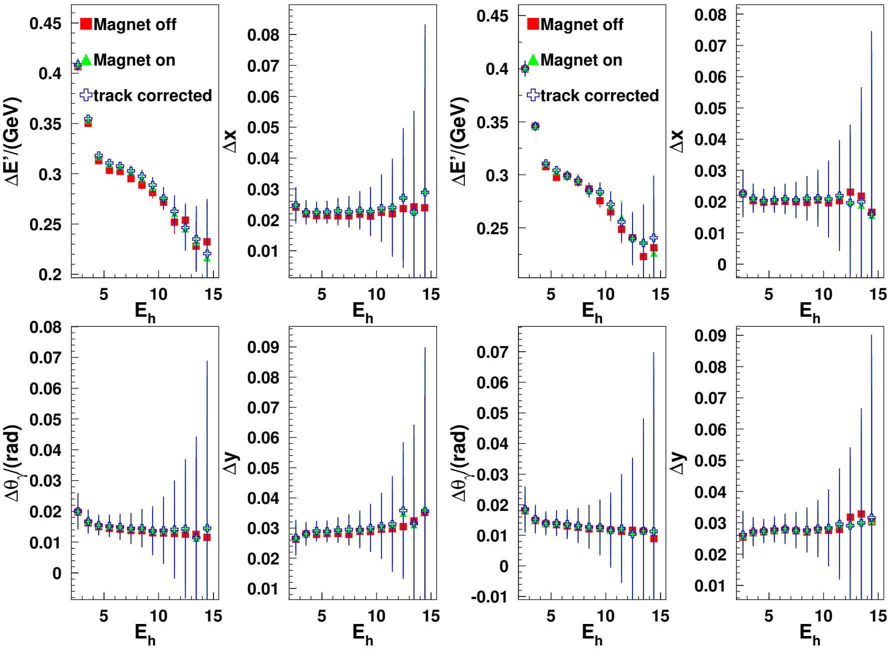

Figure F.1: Comparison in the resolutions of the lepton kinematical variables E', x, θ_γ and y vs. hadron energy for π^+ in the left panel and π^- in the right panel.

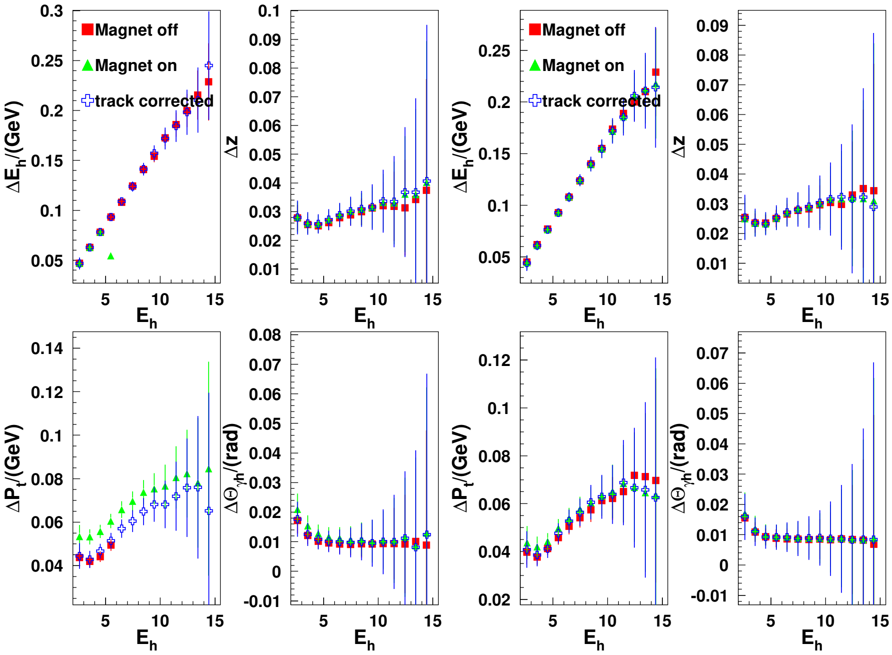

Figure F.2: Comparison in the resolutions of the hadron kinematical variables E_h, z, P_t and $\theta_{\gamma,h}$ vs. hadron energy for π^+ in the left panel and π^- in the right panel.

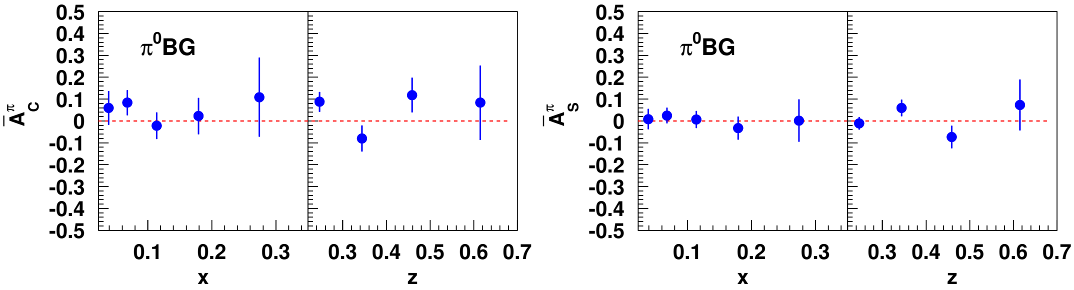

Figure F.3: Unweighted asymmetries of the nonresonant $\gamma\gamma$ background in the 25 MeV sidebands around the π^0 mass region. Left: Collins type asymmetries, right: Sivers type asymmetries.

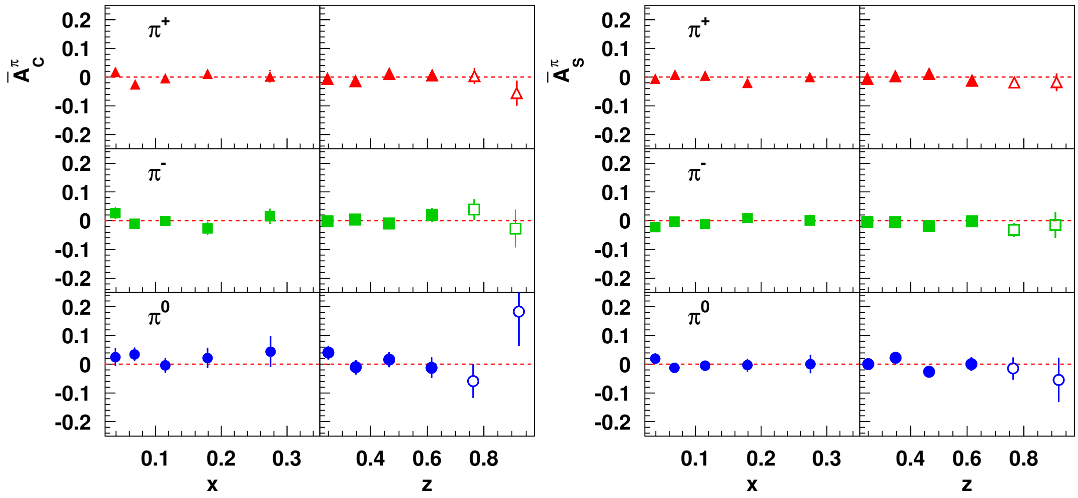

Figure F.4: Asymmetries where the spin state of each event was arbitrarily assigned. Left: Collins type asymmetries, right: Sivers type asymmetries.

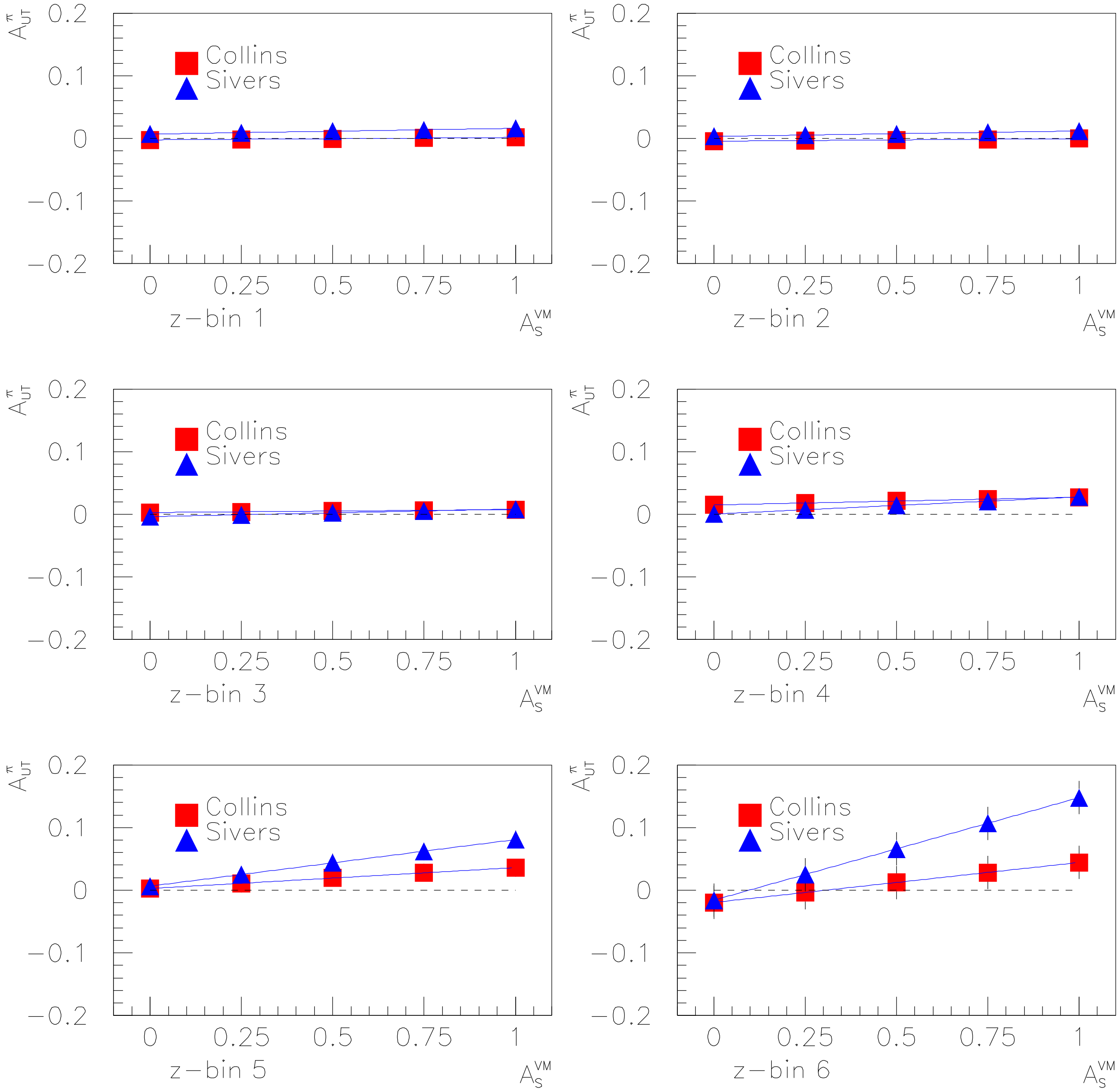

Figure F.5: Asymmetry transfer for all π^+ in the transversity pion sample generated with PYTHIA6 versus the Sivers asymmetry generated in the original exclusive vector meson sample for the 6 z-bins.

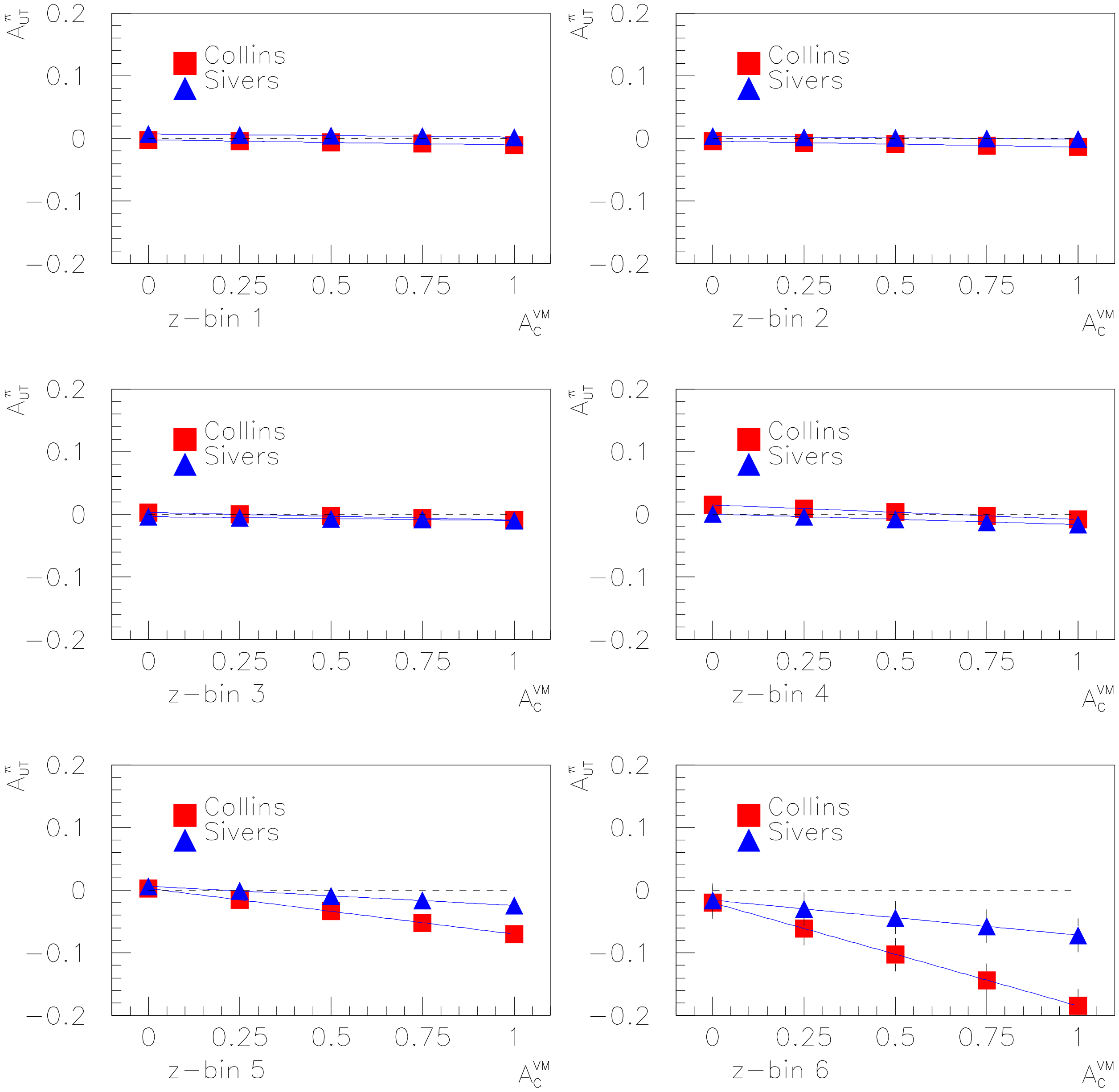

Figure F.6: Asymmetry transfer for all π^+ in the transversity pion sample generated with PYTHIA6 versus the Collins asymmetry generated in the original exclusive vector meson sample for the 6 z-bins.

List of Figures

List of Tables

Bibliography

[A$^+$88] J. Ashman et al., A measurement of the spin asymmetry and determination of the structure function g_1 in deep inelastic muon proton scattering, *Phys. Lett.*, B206:364, 1988.

[A$^+$95] F. Abe et al., Observation of top quark production in anti-p p collisions, *Phys. Rev. Lett.*, 74:2626–2631, 1995.

[A$^+$98a] K. Ackerstaff et al., The HERMES spectrometer, *Nucl. Instrum. Meth.*, A417:230–265, 1998.

[A$^+$98b] A. Airapetian et al., Measurement of the proton spin structure function $g_{1(p)}$ with a pure hydrogen target, *Phys. Lett.*, B442:484–492, 1998.

[A$^+$99] K. Abe et al., Measurements of $R = \sigma(L)/\sigma(T)$ for 0.03 < x < 0.1 and fit to world data, *Phys. Lett.*, B452:194–200, 1999.

[A$^+$00] A. Airapetian et al., Observation of a single-spin azimuthal asymmetry in semi-inclusive pion electro-production, *Phys. Rev. Lett.*, 84:4047–4051, 2000.

[A$^+$01a] A. Airapetian et al., Multiplicity of charged and neutral pions in deep-inelastic scattering of 27.5-GeV positrons on hydrogen, *Eur. Phys. J.*, C21:599–606, 2001.

[A$^+$01b] A. Airapetian et al., Single-spin azimuthal asymmetries in electroproduction of neutral pions in semi-inclusive deep-inelastic scattering, *Phys. Rev.*, D64:097101, 2001.

[A$^+$02a] A. Abashian et al., The BELLE detector, *Nucl. Instrum. Meth.*, A479:117–232, 2002.

[A$^+$02b] N. Akopov et al., The HERMES dual-radiator ring imaging Cerenkov detector, *Nucl. Instrum. Meth.*, A479:511–530, 2002.

[A$^+$03a] K. H. Ackermann et al., STAR detector overview, *Nucl. Instrum. Meth.*, A499:624–632, 2003.

[A$^+$03b] A. Airapetian et al., Measurement of single-spin azimuthal asymmetries in semi-inclusive electroproduction of pions and kaons on a longitudinally polarised deuterium target, *Phys. Lett.*, B562:182–192, 2003.

[A$^+$03c] L. Aphecetche et al., PHENIX calorimeter, *Nucl. Instrum. Meth.*, A499:521–536, 2003.

[A$^+$03d] H. Avakian et al., Measurement of beam-spin asymmetries for deep inelastic pi^+ electroproduction, *hep-ex/0301005*, 2003.

[A$^+$04] A. Airapetian et al., Flavor decomposition of the sea quark helicity distributions in the nucleon from semi-inclusive deep- inelastic scattering, *Phys. Rev. Lett.*, 92:012005, 2004.

[ADHK97] S. Aoki, M. Doui, T. Hatsuda, and Y. Kuramashi, Tensor charge of the nucleon in lattice QCD, *Phys. Rev.*, D56:433–436, 1997.

[ALS03] E.-C. Aschenauer, P. Liebing, and T. Sjostrand, in preparation, 2003.

[AM90] X. Artru and M. Mekhfi, Transversely polarized parton densities, their evolution and their measurement, *Z. Phys.*, C45:669, 1990.

[AMS$^+$04] W. Augustyniak, A. Miller, G. Schnell, S. Yen, and P. Zupranski, TMC-Vertex Reconstruction in the Presence of the HERMES transverse target magnet - to appear as a HERMES internal note, 2004.

[AP77] G. Altarelli and G. Parisi, Asymptotic freedom in parton language, *Nucl. Phys.*, B126:298, 1977.

[Art91] X. Artru, Transverse polarization in deep inelastic collisions, *AIP Conf. Proc.*, 223:176–183, 1991.

[Art93] X. Artru, Proposals for measuring transversity distributions in deep inelastic electron scattering and a model for E-704 asymmetries, *hep-ph/9310323*, 1993.

[B$^+$02] C. Baumgarten et al., An atomic beam polarimeter to measure the nuclear polarization in the HERMES gaseous polarized hydrogen and deuterium target, *Nucl. Instrum. Meth.*, A482:606–618, 2002.

[B$^+$03a] C. Baumgarten et al., A gas analyzer for the internal polarized target of the HERMES experiment, *Nucl. Instrum. Meth.*, A508:268–275, 2003.

[B$^+$03b] C. Baumgarten et al., The storage cell of the polarized H/D internal gas target of the HERMES experiment at HERA, *Nucl. Instrum. Meth.*, A496:277–285, 2003.

[BBHM00] A. Bacchetta, M. Boglione, A. Henneman, and P. J. Mulders, Bounds on transverse momentum dependent distribution and fragmentation functions, *Phys. Rev. Lett.*, 85:712–715, 2000.

[BBM$^+$] R. Brun, F. Bruyant, M. Maire, A. C. McPherson, and P. Zanarini, GEANT3, CERN-DD/EE/84-1.

[BBS95] S. J. Brodsky, M. Burkardt, and I. Schmidt, Perturbative QCD constraints on the shape of polarized quark and gluon distributions, *Nucl. Phys.*, B441:197–214, 1995.

[BCD97] V. Barone, T. Calarco, and A. Drago, A confinement model calculation of $h_1(x)$, *Phys. Lett.*, B390:287–292, 1997.

[BD] J. D. Bjorken and S. D. Drell, Relativistic quantum field theory. (german translation), Bibliograph.Inst./mannheim 1967, 409 P.(B.i.- hochschultaschenbuecher, Band 101).

[BDR02] V. Barone, A. Drago, and P. G. Ratcliffe, Transverse polarisation of quarks in hadrons, *Phys. Rept.*, 359:1–168, 2002.

[BESS] A. Bacchetta, U. Elschenbroich, G. Schnell, and R. Seidl, Single Spin Azimuthal in SIDIS off a Transversely polarized proton target, *HERMES Internal Release Report.*

[BHM$^+$02] S. J. Brodsky, P. Hoyer, N. Marchal, S. Peigne, and F. Sannino, Structure functions are not parton probabilities, *Phys. Rev.*, D65:114025, 2002.

[BHS02] S. J. Brodsky, D. S. Hwang, and I. Schmidt, Final-state interactions and single-spin asymmetries in semi-inclusive deep inelastic scattering, *Phys. Lett.*, B530:99–107, 2002.

[BJY03] A. V. Belitsky, X. Ji, and F. Yuan, Final state interactions and gauge invariant parton distributions, *Nucl. Phys.*, B656:165–198, 2003.

[BK03] A. Bruell and A. Kisselev, communications on the HERMES tracking list, 2003.

[BKMM02] A. Bacchetta, R. Kundu, A. Metz, and P. J. Mulders, Estimate of the Collins fragmentation function in a chiral invariant approach, *Phys. Rev.*, D65:094021, 2002.

[BM98] D. Boer and P. J. Mulders, Time-reversal odd distribution functions in leptoproduction, *Phys. Rev.*, D57:5780–5786, 1998.

[BMP03] D. Boer, P. J. Mulders, and F. Pijlman, Universality of T-odd effects in single spin and azimuthal asymmetries, *Nucl. Phys.*, B667:201–241, 2003.

[BO03] A. Bacchetta and K. A. Oganessyan, Private communication, 2003.

[BR] V. Barone and P. G. Ratcliffe, Transverse spin physics, River Edge, USA: World Scientific (2003) 294 p.

[BR03] A. Bacchetta and M. Radici, Partial-wave analysis of two-hadron fragmentation functions, *Phys. Rev.*, D67:094002, 2003.

[BSY04] A. Bacchetta, A. Schaefer, and J. Yang, Sivers function in a spectator model with axial-vector diquarks, *Phys. Lett.*, B578:109–118, 2004.

[Bac02] A. Bacchetta, Probing the transverse spin of quarks in deep inelastic scattering, *hep-ph/0212025*, 2002.

[Bac04] A. Bacchetta, Single-Spin Asymmetries with two-hadron fragmentation functions, Talk given at the DIS2004, 2004.

[Bec] M. Beckmann, Extraction of polarised quark distributions of the nucleon from deep inelastic scattering at the HERMES experiment, DESY-THESIS-2000-029.

[Bera] S. Bernreuther, The HERMES drift chamber system BC 1 / 2. (In German), DESY-HERMES-95-68.

[Berb] Stefan Bernreuther, Measurement of spin transfer at Lambda0 production in polarized lepton nucleon scattering in the HERMES experiment. (In German), DESY-THESIS-2000-003.

[Bjo69] J. D. Bjorken, Asymptotic sum rules at infinite momentum, *Phys. Rev.*, 179:1547–1553, 1969.

[Bur02] M. Burkardt, Impact parameter dependent parton distributions and transverse single spin asymmetries, *Phys. Rev.*, D66:114005, 2002.

[Bur04] M. Burkardt, Sivers mechanism for gluons, *hep-ph/0402014*, 2004.

[CG69] Jr. Callan, C. G. and D. J. Gross, High-energy electroproduction and the constitution of the electric current, *Phys. Rev. Lett.*, 22:156–159, 1969.

[Col93] J. C. Collins, Fragmentation of transversely polarized quarks probed in transverse momentum distributions, *Nucl. Phys.*, B396:161–182, 1993.

[Col02] J. C. Collins, Leading-twist single-transverse-spin asymmetries: Drell-Yan and deep-inelastic scattering, *Phys. Lett.*, B536:43–48, 2002.

[DCS] R. Devenish and A. Cooper-Sarkar, Deep inelastic scattering, Oxford, UK: Univ. Pr. (2004) 403 p.

[DY70] S. D. Drell and T. Yan, Massive lepton pair production in hadron - hadron collisions at high-energies, *Phys. Rev. Lett.*, 25:316–320, 1970.

[Die04] M. Diehl, DVCS and exclusive processes,, june 2004.

[Dok77] Y. L. Dokshitzer, Calculation of the structure functions for deep inelastic scattering and e+ e- annihilation by perturbation theory in quantum chromodynamics . (in russian), *Sov. Phys. JETP*, 46:641–653, 1977.

[EGS02a] A. V. Efremov, K. Goeke, and P. Schweitzer, Azimuthal asymmetries and Collins analyzing power, *Nucl. Phys.*, A711:84–88, 2002.

[EGS02b] A. V. Efremov, K. Goeke, and P. Schweitzer, Predictions for azimuthal asymmetries in pion and kaon production in SIDIS off a longitudinally polarized deuterium target at HERMES, *Eur. Phys. J.*, C24:407–412, 2002.

[EGS03] A. V. Efremov, K. Goeke, and P. Schweitzer, Collins effect and single spin azimuthal asymmetries in the HERMES and COMPASS experiments, *Eur. Phys. J.*, C32:337–346, 2003.

[EM74] P. Estabrooks and A. D. Martin, π π phase shift analysis below the K anti-K threshold, *Nucl. Phys.*, B79:301, 1974.

[ESS] U. Elschenbroich, G. Schnell, and R. Seidl, Single Spin Azimuthal in SIDIS off a Transversely polarized proton target – MC-studies, *HERMES Internal Report 03-007*.

[EST99] A. V. Efremov, O. G. Smirnova, and L. G. Tkachev, Study of T-odd quark fragmentation function in Z0 $\rightarrow$ 2-jet decay, *Nucl. Phys. Proc. Suppl.*, 74:49–52, 1999.

[Ell] F. Ellinghaus, Beam charge and beam spin azimuthal asymmetries in deeply-virtual Compton scattering, DESY-THESIS-2004-005.

[Els03] U. Elschenbroich, Status Report of the Transverse Asyemmtries,, dec 2003.

[FF78] R. D. Field and R. P. Feynman, A parametrization of the properties of quark jets, *Nucl. Phys.*, B136:1, 1978.

[FKOU95] M. Fukugita, Y. Kuramashi, M. Okawa, and A. Ukawa, Proton spin structure from lattice QCD, *Phys. Rev. Lett.*, 75:2092–2095, 1995.

[Fis04] H. Fischer, Transverse asymmetry A_{UT} for charged pions ,Talk given at the DIS2004, 2004.

[Fun] M. A. Funk, A measurement of the polarised parton densities of the nucleon in deep-inelastic scattering at HERMES, DESY-THESIS-1998-017.

[GGO03a] L. P. Gamberg, G. R. Goldstein, and K. A. Oganessyan, Novel transversity properties in semi-inclusive deep inelastic scattering, *Phys. Rev.*, D67:071504, 2003.

[GGO03b] L. P. Gamberg, G. R. Goldstein, and K. A. Oganessyan, A mechanism for the T-odd pion fragmentation function, *Phys. Rev.*, D68:051501, 2003.

[GGO04] L. Gamberg, G. R. Goldstein, and K. A. Oganessyan, Novel transversity properties in SIDIS, *AIP Conf. Proc.*, 698:617–620, 2004.

[GHO04] L. P. Gamberg, D. S. Hwang, and K. A. Oganessyan, Chiral-odd fragmentation functions in single pion inclusive electroproduction, *Phys. Lett.*, B584:276–284, 2004.

[GL72] V. N. Gribov and L. N. Lipatov, Deep inelastic e p scattering in perturbation theory, *Yad. Fiz.*, 15:781–807, 1972.

[GM64] M. Gell-Mann, A Schematic model of baryons and mesons, *Phys. Lett.*, 8:214–215, 1964.

[GPV01] K. Goeke, Maxim V. Polyakov, and M. Vanderhaeghen, Hard exclusive reactions and the structure of hadrons, *Prog. Part. Nucl. Phys.*, 47:401–515, 2001.

[Gri] D. J. Griffiths, Introduction to elementary particles, NEW YORK, USA: WILEY (1987) 392p.

[Gro93] CERN Programming Techniques Group, ADAMO– Entity-Relationship Programming System, Users Guide, Version 3.3, 1993.

[HGPO$^+$03] K. Hasuko, M. Grosse Perdekamp, A. Ogawa, J. S. Lange, and V. Siegle, Azimuthal asymmetries in fragmentation processes at KEKB, *AIP Conf. Proc.*, 675:454–458, 2003.

[Has02] D. Hasch, Private comunication, 2002.

[Hil] A. Hillenbrand, Tuning of the Lund model for fragmentation functions and purities, Prepared for 11th International Workshop on Deep Inelastic Scattering (DIS 2003), St. Petersburg, Russia, 23-27 Apr 2003.

[IER97] G. Ingelman, A. Edin, and J. Rathsman, LEPTO 6.5 - A Monte Carlo Generator for Deep Inelastic Lepton-Nucleon Scattering, *Comput. Phys. Commun.*, 101:108–134, 1997.

[JJ92] R. L. Jaffe and X. Ji, Chiral odd parton distributions and Drell-Yan processes, *Nucl. Phys.*, B375:527–560, 1992.

[JMR97] R. Jakob, P. J. Mulders, and J. Rodrigues, Modelling quark distribution and fragmentation functions, *Nucl. Phys.*, A626:937–965, 1997.

[JMY04] X. Ji, J. Ma, and F. Yuan, QCD Factorization for Semi-Inlcusive Deep-Inelastic Scttering at Low Transverse Momenta, 2004.

[JR75] F. James and M. Roos, 'MINUIT' A System for function minimization and analysis of the parameter errors and correlations, *Comput. Phys. Commun.*, 10:343–367, 1975.

[JY02] X. Ji and F. Yuan, Parton distributions in light-cone gauge: Where are the final-state interactions?, *Phys. Lett.*, B543:66–72, 2002.

[Jaf97] R. L. Jaffe, Can transversity be measured?, *hep-ph/9710465*, 1997.

[Ji97a] X. Ji, Deeply-virtual Compton scattering, *Phys. Rev.*, D55:7114–7125, 1997.

[Ji97b] X. Ji, Gauge invariant decomposition of nucleon spin, *Phys. Rev. Lett.*, 78:610–613, 1997.

[KE] S. Kowalski and H.A. Enge, RAYTRACE, *unpublished.*

[KLC01] S. Kretzer, E. Leader, and E. Christova, Fragmentation functions from semi-inclusive DIS pion production and implications for the polarized parton densities, *Eur. Phys. J.*, C22:269–276, 2001.

[KLC02] S. Kretzer, E. Leader, and E. Christova, Fragmentation functions and their role in determining the polarized parton densities, *Acta Phys. Polon.*, B33:3743–3748, 2002.

[KM97] A. M. Kotzinian and P. J. Mulders, Probing transverse quark polarization via azimuthal asymmetries in leptoproduction, *Phys. Lett.*, B406:373–380, 1997.

[KPG96a] H. Kim, M. V. Polyakov, and K. Goeke, Nucleon “Tensor Charges” in the Chiral Quark–Soliton Model, *Phys. Rev.*, D53:4715–4718, 1996.

[KPG96b] H. Kim, Maxim V. Polyakov, and K. Goeke, Tensor Charges of the Nucleon in the SU(3) Chiral Quark Soliton Model, *Phys. Lett.*, B387:577–581, 1996.

[Kot03] A. Kotzinian, Polarized SIDIS: Comment on purity method for extraction of polarized quark distributions, *Phys. Lett.*, B552:172–176, 2003.

[LM04] Z. Lue and B.Q. Ma, Sivers function in light-cone quark model and azimuthal spin asymmetries in pion electroproduction, *submitted to Nucl.Phys.*, A, 2004.

[LRT03] P. Lenisa, D. Reggiani, and P. Tait, Private communication, 2003.

[Lea01] E. Leader, Spin in particle physics, *Cambridge Monogr. Part. Phys. Nucl. Phys. Cosmol.*, 15:1, 2001.

[Lie] P Liebing, Double Spin Asymmetries in Single Hadron Quasi-Real Photoproduction at HERMES, *HERMES Internal Report 01-008*.

[MPXZ89] T. Meng, J. Pan, Q. Xie, and W. Zhu, Origin of proton spin: rotating constituents?, *Phys. Rev.*, D40:769, 1989.

[MSY02a] B. Ma, I. Schmidt, and J. Yang, Azimuthal spin asymmetries of pion electroproduction, *Phys. Rev.*, D65:034010, 2002.

[MSY02b] B. Ma, I. Schmidt, and J. Yang, Reanalysis of azimuthal spin asymmetries of meson electroproduction, *Phys. Rev.*, D66:094001, 2002.

[MT96] P. J. Mulders and R. D. Tangerman, The complete tree-level result up to order 1/Q for polarized deep-inelastic leptoproduction, *Nucl. Phys.*, B461:197–237, 1996.

[Mal04] G. K. Mallot, The COMPASS spectrometer at CERN, *Nucl. Instrum. Meth.*, A518:121–124, 2004.

[Men] F. M. Menden, Determination of the gluon polarization in the nucleon, DESY-THESIS-2001-060.

[N^+03] A. Nass et al., The HERMES polarized atomic beam source, *Nucl. Instrum. Meth.*, A505:633–644, 2003.

[P^+02] J. Pumplin et al., New generation of parton distributions with uncertainties from global QCD analysis, *JHEP*, 07:012, 2002.

[PFTV88] William H. P., Brian P. F., Saul A. T., and William T. V., *Numerical recipes in C: the art of scientific computing*, Cambridge University Press, 1988.

[PS] M. E. Peskin and D. V. Schroeder, An Introduction to quantum field theory, Reading, USA: Addison-Wesley (1995) 842 p.

[PSRZ] B. Povh, C. Scholz, K. Rith, and F. Zetsche, Particles and nuclei: An introduction to the physical conceptions. (In German), Berlin, Germany: Springer 4^{th} edition (2004) 396 p.

[Pob02] P. V. Pobylitsa, T-odd quark distributions: QCD versus chiral models, *hep-ph/0212027*, 2002.

[QS99] J. Qiu and G. Sterman, Single transverse-spin asymmetries in hadronic pion production, *Phys. Rev.*, D59:014004, 1999.

[RJB02] M. Radici, R. Jakob, and A. Bianconi, Accessing transversity with interference fragmentation functions, *Phys. Rev.*, D65:074031, 2002.

[Rob] R. G. Roberts, The Structure of the proton: Deep inelastic scattering, Cambridge, UK: Univ. Pr. (1990) 182 p. (Cambridge monographs on mathematical physics).

[Ros50] M. N. Rosenbluth, *Phys. Rev.*, 79:615, 1950.

[S$^+$01] P. Schweitzer et al., Transversity distributions in the nucleon in the large-N(c) limit, *Phys. Rev.*, D64:034013, 2001.

[SB04] P. Schweitzer and A. Bacchetta, Azimuthal single spin asymmetries in SIDIS in the light of chiral symmetry breaking, *Nucl. Phys.*, A732:106–124, 2004.

[SLMS03] T. Sjostrand, L. Lonnblad, S. Mrenna, and P. Skands, PYTHIA 6.3 physics and manual, *hep-ph/0308153*, 2003.

[SS97] I. Schmidt and J. Soffer, Melosh rotation and the nucleon tensor charge, *Phys. Lett.*, B407:331–334, 1997.

[ST64] A. A. Sokolov and I. M. Ternov, On Polarization and spin effects in the theory of synchrotron radiation, *Phys. Dokl.*, 8:1203–1205, 1964.

[ST00] A. Schafer and O. V. Teryaev, Sum rules for the T-odd fragmentation functions, *Phys. Rev.*, D61:077903, 2000.

[SW98] K. Suzuki and W. Weise, Chiral constituent quarks and their role in quark distribution functions of nucleon and pion, *Nucl. Phys.*, A634:141–165, 1998.

[Siv90] D. W. Sivers, Single spin production asymmetries from the hard scattering of point - like constituents, *Phys. Rev.*, D41:83, 1990.

[Sjo95] T. Sjostrand, PYTHIA 5.7 and JETSET 7.4: Physics and manual, *hep-ph/9508391*, 1995.

[Sof95] J. Soffer, Positivity constraints for spin dependent parton distributions, *Phys. Rev. Lett.*, 74:1292–1294, 1995.

[Str93] M. Stratmann, Bag model predictions for polarized structure functions and their Q^2 evolutions, *Z. Phys.*, C60:763–772, 1993.

[Tan04] H. Tanaka, A purity formalism for the extraction of h1 and/or $f_{1T}^{\perp}$,, dec 2004.

[W$^+$] W. Wander et al., DAD - Distributed ADAMO Database system at HERMES, Prepared for International Conference on Computing in High- energy Physics (CHEP 95), Rio de Janeiro, Brazil, 18-22 Sep 1995.

[WK99] M. Wakamatsu and T. Kubota, Chiral symmetry and the nucleon spin structure functions, *Phys. Rev.*, D60:034020, 1999.

[WRB$^+$90] L. W. Whitlow, S. Rock, A. Bodek, E. M. Riordan, and S. Dasu, A Precise extraction of $R = \sigma(L)/\sigma(T)$ from a global analysis of the SLAC deep inelastic e p and e d scattering cross-sections, *Phys. Lett.*, B250:193–198, 1990.

[Wak01] M. Wakamatsu, Chiral-odd distribution functions in the chiral quark soliton model, *Phys. Lett.*, B509:59–68, 2001.

[Wan] W. Wander, Reconstruction of high-energy scattering events in the HERMES experiment. (In German), DESY-HERMES-96-23.

[Web04] R Webb, Erste Messungen transversaler Spinasymmetrien durch Einzelpionproduktion am COMPASS-Experiment, 2004.

[Wei] C. Weiskopf, Measurement of the spin-dependent structure function $g_{1(d)}$ of the deuteron at HERMES. (In German), DESY-THESIS-2002-039.

[Wen] J. Wendland, Polarized parton distributions measured at the HERMES experiment, DESY-THESIS-2003-032.

[tHV72] G. 't Hooft and M. J. G. Veltman, Regularization and renormalization of gauge fields, *Nucl. Phys.*, B44:189–213, 1972.

Acknowledgment

> *Nichts beflügelt die Wissenschaft so, wie der Schwatz mit Kollegen auf dem Flur.*
>
> *Arno Penzias*

First of all I would like to thank my supervisor Prof. Dr. Klaus Rith for this very new and only recently addressed subject of transversity. He took the time when discussion of the implications of the analysis and the results was necessary but left me the freedom to develop the analysis procedure and choose the systematic studies according to what I thought the best way to proceed. I am also grateful that he gave me the opportunity to attend several important conferences and workshops which significantly helped to discuss the still theoretically not so settled properties of the transverse momentum dependent functions with theorists and experimental colleagues. I also owe him that I could spend two years of my Ph.D studies on-site at the HERMES experiment at DESY. There, the high density of fellow HERMES members and other physicists was extremely fruitful for the advance of the analysis and the understanding of the functions involved. From the experiment I have to thank Delia Hasch in helping me to get a jump-start on the analysis. The previous spokesperson Prof. Dr. Dirk Ryckbosch encouraged me to have a very early look at the raw 2002 data to find the new asymmetries which have been presented in its final form in this thesis. It was also him who proposed his Ph. D student Ulrike Elschenbroich to perform the cross check on this analysis. Together, Uli and I were a good team in analyzing the data, performing systematic studies and improving the understanding. She was a great help in getting all the studies and plots for the many reports and releases done. I would also like to thank several members of the HERMES management, namely the two analysis coordinators I experienced, Uta Stoesslein and Moskov Amarian and especially Elke Aschenauer. She is one of the Monte Carlo gurus, was always very well informed on the ongoing analysis, ensures the experiment to be running and is currently the spokesperson of HERMES. All those involved in the data production chain, starting from the data cops to maintaining the PC-farm were due to the great reliability also very important for the analysis of the data.

Under the lead of Gunar Schnell the others from the transversity working group were, in many discussions and subgroup meetings, the source of many better insights on the subject.

From the experimental side these were Naomi Makins, Hide Tanaka-san, Paul van der Nat, Ingrid Gregor and Ivana Hristova. I have to especially thank Andy Miller since he became the driving source of improvements in the analysis and its interpretations. From the theoretical side I have to thank Alessandro Bacchetta and Karo Oganessyan for many discussions and general improvement on the understanding of the theoretical implications mainly concerning the crucial convolution integrals appearing in the cross sections. I would also like to thank my colleagues from Erlangen who were always the source of many physics and non-physics discussions during the lunch and coffee breaks and the internal seminars. Those include among others Prof. Dr. Erhard Steffens, Achim Hillenbrand, Martin Raithel, Phil Tait, Nils Pickert, Christian Vogel, Friedrich Stinzing and Bernhard Krauss. I would also like to thank my diploma student Markus Diefenthaler who was always very keen on discussions on the theoretical basis of transversity and the aspects of the analysis techniques. He was also very cooperational and patient during the hot phase of writing this thesis.

A special thanks goes to those who shared the office with me, which were in Erlangen Christian Weisskopf, Caroline Riedl, Didi Zeiler and Tom Michler and in Hamburg Marc Beckman, Larry Felawka and temporarily Jürgen Wendland and Lara de Nardo. With them one could not only discuss physics but also have other interesting conversations and a good laugh. Then a big thanks goes to the whole bunch of regular offsite-meeting enthusiasts which were Beni Ziehlman, Larry, Frank Ellinghaus, Caro, Bino and most of the younger members of the HERMES collaboration, who made the excursions in the night-life of Hamburg a very amusing and sometimes liver threatening experience.

I would like to thank also those colleagues from the Tokyo Institute of Technology under the lead of Prof. Shibata-san and Yoshi Miyachi-san who gave me such a friendly welcome and helped an illiterate gaijin to get along in Tokyo. A big help were the secretaries, in Hamburg Soerne Moeller and Sabine Krohn and in Erlangen Eleonore Hassler. They took care of all the bureaucracy involved in travel, organizing of meeting rooms and phone conferences.

Also important were all the friends taking part in all the non-physics activities like going out, swimming, running, surfing, snowboarding, wakeboarding and lan-parties. It is always very important to remember that physics is not everything in life.

The most important thanks are due for my parents who supported me, especially as an undergrad student and who always greatly approved the scientific way I was choosing. I would like to thank also my sister Britta for the many times we met at interesting parties in Bremen and Hamburg.

Curriculum vitae

Personal Details

Name:	Ralf-Christian Seidl
Date of birth:	June 11, 1975
Place of birth:	Nürnberg, Germany
Age:	29
Nationality:	German
email-address:	ralf.seidl@physik.uni-erlangen.de

Education

1981-1985:	Georg Ledebour Grundschule, Nürnberg, Germany
1985-1994:	Martin Behaim Gymnasium, Nürnberg, Germany
	Abitur (A-levels)
1994-1995:	Military Service in Ahlen and Roth, Germany
1995-1997:	Universität Erlangen-Nürnberg, Germany
	Vordiplom (BSc)
1997-1998:	Universidad de Cantabria, Santander, Spain
1998-2001:	Universität Erlangen-Nürnberg, Germany
	Diplom (MSc)
2001-2004:	Ph.D Student at the Universität Erlangen-Nürnberg, Germany

Erlangen, July 28, 2004 ....

Publications

- U. Elschenbroich, G. Schnell and R. Seidl [HERMES Collaboration], "Transverse spin physics at HERMES, arXiv:hep-ex/0405017.
- R. Seidl [HERMES Collaboration], "Single spin azimuthal asymmetries and transversity," DESY-HERMES-03-23 *Prepared for 8th Conference on the Intersections of Particle and Nuclear Physics (CIPANP 2003), New York, New York, 19-24 May 2003*
- A. Airapetian *et al.* [HERMES Collaboration], "Evidence for a narrow |S| = 1 baryon state at a mass of 1528-MeV in quasi-real photoproduction," Phys. Lett. B **585**, 213 (2004) [arXiv:hep-ex/0312044].
- A. Airapetian *et al.* [HERMES Collaboration], "Nuclear polarization of molecular hydrogen recombined on a non-metallic surface," DESY-03-168
- A. Airapetian *et al.* [HERMES Collaboration], "Flavor decomposition of the sea quark helicity distributions in the nucleon from semi-inclusive deep-inelastic scattering," Phys. Rev. Lett. **92**, 012005 (2004) [arXiv:hep-ex/0307064].
- A. Airapetian *et al.* [HERMES Collaboration], "Quark fragmentation to pi+-, pi0, K+-, p and anti-p in the nuclear environment," Phys. Lett. B **577**, 37 (2003) [arXiv:hep-ex/0307023].
- A. Airapetian *et al.* [HERMES Collaboration], "Double-spin asymmetries in the cross section of rho0 and Phi production at intermediate energies," Eur. Phys. J. C **29**, 171 (2003) [arXiv:hep-ex/0302012].
- A. Airapetian *et al.* [HERMES Collaboration], "Measurement of single-spin azimuthal asymmetries in semi-inclusive electroproduction of pions and kaons on a longitudinally polarised deuterium target," Phys. Lett. B **562**, 182 (2003) [arXiv:hep-ex/0212039].